Development of Dose Verification Detectors

Towards Improving Proton Therapy Outcomes

by

Jason M. Holmes

A Dissertation Presented in Partial Fulfillment
of the Requirements for the Degree
Doctor of Philosophy

Approved April 2019 by the
Graduate Supervisory Committee:

Ricardo Alarcón, Chair
Martin Bues
Ralph Chamberlin
Evgeny Galyaev

ARIZONA STATE UNIVERSITY

May 2019

ABSTRACT

The challenge of radiation therapy is to maximize the dose to the tumor while simultaneously minimizing the dose elsewhere. Proton therapy is well suited to this challenge due to the way protons slow down in matter. As the proton slows down, the rate of energy loss per unit path length continuously increases leading to a sharp dose near the end of range. Unlike conventional radiation therapy, protons stop inside the patient, sparing tissue beyond the tumor. Proton therapy should be superior to existing modalities, however, because protons stop inside the patient, there is uncertainty in the range. "Range uncertainty" causes doctors to take a conservative approach in treatment planning, counteracting the advantages offered by proton therapy. Range uncertainty prevents proton therapy from reaching its full potential.

A new method of delivering protons, pencil-beam scanning (PBS), has become the new standard for treatment over the past few years. PBS utilizes magnets to raster scan a thin proton beam across the tumor at discrete locations and using many discrete pulses of typically 10 ms duration each. The depth is controlled by changing the beam energy. The discretization in time of the proton delivery allows for new methods of dose verification, however few devices have been developed which can meet the bandwidth demands of PBS.

In this work, two devices have been developed to perform dose verification and monitoring with an emphasis placed on fast response times. Measurements were performed at the Mayo Clinic. One detector addresses range uncertainty by measuring prompt gamma-rays emitted during treatment. The range detector presented in this work is able to measure the proton range in-vivo to within 1.1 mm at depths up to 11 cm in less than 500 ms and up to 7.5 cm in less than 200 ms. A beam fluence detector presented in this work is able to measure the position and shape of each beam spot.

It is hoped that this work may lead to a further maturation of detection techniques in proton therapy, helping the treatment to reach its full potential to improve the outcomes in patients.

DEDICATION

To the love of my life, Brittny, and my beautiful daughters, Natalie, Claire, and Johanna.

ACKNOWLEDGMENTS

I would like to thank my advisor, Dr. Ricardo Alarcón, for always placing a great amount of trust in me, for his general excitement of physics, and especially for providing countless research opportunities. It has been nothing but a great pleasure to work with Ricardo and I look forward to continuing our work.

To Dr. Martin Bues and Dr. Jiajian Shen of Mayo Clinic, I am thankful for their support through the years, for allowing access to world-class facilities and always going above and beyond in their assistance of this project. I have been genuinely impressed by the Mayo Clinic and the overall commitment to excellence in both patient treatment and research. I particularly want to thank the Marley Foundation for providing seed funding to the project, making possible the development of the devices.

I would like to thank my friend/colleague/lab-mate Dr. David Blyth, for providing mentorship throughout my Ph.D., helping to shape my research philosophies and generally teaching me what it means to be a great scientist.

To Dr. Evgeny Galyaev, I am thankful for the mentorship and friendship, for the genuine care expressed for myself and my family, and for opportunities to come.

Thank you to Dr. Ralph Chamberlin for being a committee member, and for your support as a program advisor and professor of multiple of my classes.

To my lab mates and colleagues over the years, Rafael, Jesse, Ben, Kevin, Lauren, and Glenn for the entertainment, never ending lunches, the insights, and the amazing work, I am grateful.

Lastly, I am forever grateful to my wife, Brittny, and daughters, Natalie, Claire, and Johanna, for making my dreams come true. And to my parents, Mike and LuAnn, my brother, Brian, for their love and support.

TABLE OF CONTENTS

CHAPTER Page

LIST OF TABLES

Table Page

LIST OF FIGURES

Figure Page

Figure Page

Figure Page

Chapter 1

PHYSICS OF ENERGETIC PROTONS INTERACTING WITH MATERIAL

In the context of proton therapy, a common assumption is that protons interacting with matter can be accurately modeled by consideration of only three types of interactions: (1) Energy loss due to atomic ionization/excitation, (2) deflection due to elastic/inelastic collisions with nuclei, and (3) production of secondaries due to inelastic collisions with nuclei. In this section, an overview of proton physics relevant to medical physics will be given to explain why these assumptions are made.

1.1 Proton Energy Deposition in Matter

We would like to determine the maximum possible energy, ΔE_{max}, that the proton could transfer in a single elastic head-on collision with any particle. Conserving energy and momentum, we can calculate the velocities of both particles after colliding,

$$v_1 = v\left(1 - \frac{2m_2}{m_1 + m_2}\right) \tag{1.1}$$

$$v_2 = \frac{2vm_1}{m_1 + m_2}\ , \tag{1.2}$$

where m_1 is the mass of the proton with initial velocity v, m_2 is the mass of the initially at-rest target particle, v_1 is the final velocity of the proton, and v_2 is the final velocity of the target particle. Now solving for the energy of the target particle or equivalently the energy lost by the proton,

$$\Delta E_{max} = \frac{1}{2}m_1 v^2 \frac{4m_1 m_2}{(m_1 + m_2)^2}\ . \tag{1.3}$$

Plugging in some numbers as an example, protons can lose close to 100 times more energy in a collision with an Oxygen nuclei than that of atomic electrons per interaction. However, the likelihood of scattering with a nucleus is much smaller than that of an atomic electron. In fact, a proton will interact with nuclei less than one time on average before it stops in a material (see Section 1.3, Figure 6). Consider the ratio of the geometric cross sections of a typical atom and nucleus, $\frac{\sigma_{atom}}{\sigma_{nucleus}} \approx \frac{^2}{fm^2} = 10^{10}$. Since a proton will interact with the atomic electrons millions of times along its path (see Section 1.2.1), while on average less than once with a nucleus, we can conclude that the amount of energy lost by a proton as it traverses through matter is completely dominated by interactions with atomic electrons.

1.1.1 Stopping Power and the Bethe Formula

The energy lost by a charged particle as it traverses through matter can be calculated using the Bethe formula which only considers interactions with atomic electrons. A proton with velocity v and charge ze is incident upon an electron located a distance b normal from where the proton would go if no interaction occurred, also known as the impact parameter. The angle between the x-axis and the line connecting the proton to the electron is θ (see Figure 1).

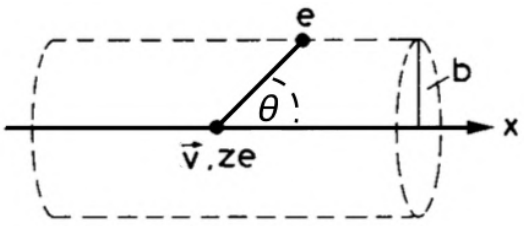

Figure 1: a setup showing the relevant parameters for deriving the Bethe formula

We would like to determine the stopping power or energy loss per unit path length, $\frac{dE}{dx}$, for the proton interacting with electrons in a material. Our strategy first done by Bohr [11] is as follows: (1) Calculate the momentum transfer of a proton to an electron, (2) calculate the amount of energy lost by the proton due to the momentum transfer, and (3) account for the amount of electrons that the proton will interact with.

As the proton passes by the electron, the electron is first pushed an amount in the (+)x-direction and then in the (-)x-direction. Due to symmetry, the average momentum transfer in the x-direction will be zero. In the y-direction,

$$\Delta p_y = \int F_y \, dt = \int F_y \, \frac{dx}{dx} dt = \int \frac{F_y}{v} \, dx = \int \frac{F \sin\theta}{v} \, dx \tag{1.4}$$

$$= \int_{-\infty}^{\infty} \left(\frac{ze^2}{4\pi\epsilon_0 (x^2 + b^2)} \right) \left(\frac{b}{\sqrt{x^2 + b^2}} \right) \frac{dx}{v} \tag{1.5}$$

$$= \frac{ze^2}{4\pi\epsilon_0} \frac{b}{v} \int_{-\infty}^{\infty} \frac{dx}{(x^2 + b^2)^{\frac{3}{2}}} = \frac{ze^2}{4\pi\epsilon_0} \frac{b}{v} \frac{2}{b^2} \tag{1.6}$$

$$= \frac{ze^2}{4\pi\epsilon_0 b} \frac{2}{v} \, . \tag{1.7}$$

Now we can determine the energy transfer from the momentum transfer,

$$\Delta E = \frac{\Delta p_y^2}{2m_e} = \frac{z^2 e^4}{8\pi^2 \epsilon_0^2 b^2 v^2 m_e} = \frac{z^2 e^4}{8\pi^2 \epsilon_0^2 b^2 \beta^2 m_e c^2} \, , \tag{1.8}$$

where $\beta = v/c$. Now that we know the energy lost by the proton due to one electron, we can consider many electrons. We need to determine the number of electrons per path length that the proton will interact with and at what distances from the proton in the y-direction, b, are appropriate for considering the interaction. Our equation will take the form,

$$\text{energy loss} = \frac{\text{energy lost}}{\text{electron}} \times \frac{\text{electrons}}{\text{length}} \times \text{path length} \, . \tag{1.9}$$

The number of electrons, N_e, can be found knowing the electron density of the material, n_t, and the volume container of the electrons (bounded by values of b), $2\pi b\, db\, dx$,

$$dN_e = n_t\, 2\pi b\, db\, dx\,, \tag{1.10}$$

where the number of electrons per length becomes

$$\frac{dN_e}{dx} = n_t\, 2\pi b\, db\,. \tag{1.11}$$

The equation begins to take form as we calculate the infinitesimal energy loss due to the electrons within the volume of interest,

$$-dE = (\Delta E)\left(\frac{dN_e}{dx}\right) dx \tag{1.12}$$

$$= \left(\frac{z^2 e^4}{8\pi^2 \epsilon_0^2 b^2 \beta^2 m_e c^2}\right)(n_t\, 2\pi b\, db)\, dx \tag{1.13}$$

$$-\frac{dE}{dx} = \int_{b_{min}}^{b_{max}} \left(\frac{z^2 e^4}{8\pi^2 \epsilon_0^2 \beta^2 m_e c^2}\right)(n_t\, 2\pi)\frac{db}{b} \tag{1.14}$$

$$= \frac{z^2 e^4 n_t}{4\pi \epsilon_0^2 \beta^2 m_e c^2} \ln\left(\frac{b_{max}}{b_{min}}\right) \tag{1.15}$$

We must now choose appropriate values for b_{min} and b_{max} such that the cross section accounts for realistic interaction lengths. We chose b_{min} to be the de Broglie wavelength, $b_{min} = \frac{h}{p} = \frac{h}{\gamma m_e v}$, and b_{max} to be such that the interaction time is shorter than the period of an electron [11] (adiabatic invariance), $b_{max} = \frac{\gamma v}{\langle \nu_e \rangle}$, where $\langle \nu_e \rangle$ is the classical electron orbital frequency, thus giving for the Bethe-formula [7],

$$-\frac{dE}{dx} = \frac{z^2 e^4 n_t}{4\pi \epsilon_0^2 \beta^2 m_e c^2} \ln\left(\frac{m_e c^2 \beta^2 \gamma^2}{h\langle \nu_e \rangle}\right)\,. \tag{1.16}$$

A modern quantum based derivation of the Bethe-formula gives the slightly more correct Bethe-formula,

$$-\frac{dE}{dx} = \frac{z^2 e^4 n_t}{4\pi \epsilon_0^2 \beta^2 m_e c^2}\left[\ln\left(\frac{2 m_e c^2 \beta^2 \gamma^2}{I}\right) - \beta^2\right]\,, \tag{1.17}$$

where I is the mean excitation potential or the average amount of energy required to excite an electron in the target atom. Felix Bloch showed that the mean excitation potential can be approximated by $I = (10\text{ eV})Z$. For a proton propagating through water, the Bethe-formula becomes

$$-\frac{dE}{dx} = \frac{17.06\text{ MeV/m}}{\beta^2}\left[\ln\left(10219.98\beta^2\gamma^2\right) - \beta^2\right] \ . \tag{1.18}$$

1.1.2 Proton Range

From the Bethe formula, we can see that a charged particle will lose energy proportional to $\frac{1}{v^2}$ or $\frac{1}{E}$ at each interval. Therefore, for a sufficiently thick target, as the particle slows down, the energy decreases rapidly until the particle loses all its energy and stops. The distance the particle travels along the beam axis before stopping is called its range and for an ensemble of particles the range is point where half of the particles have stopped. The proton range vs energy in water calculated using PSTAR [6] is plotted in Figure 2. For protons with kinetic energies relevant to proton therapy, the protons are somewhat relativistic, with a β between 0.3 and 0.6. Comparing the classical kinetic energy of the protons to the relativistic case,

$$\frac{m_0c^2(\gamma-1) - \frac{1}{2}m_0c^2\beta^2}{m_0c^2(\gamma-1)} \ , \tag{1.19}$$

and plotting the results in Figure 3, we can see that before entering a target, the protons should be considered relativistic. After entering the target, the protons begin the slow-down process and have less than 5% discrepancy starting at about 1 cm from the end of range and less than 2% at about 2 mm from the end of range (in water).

It would seem the range could be calculated analytically by integrating the inverse

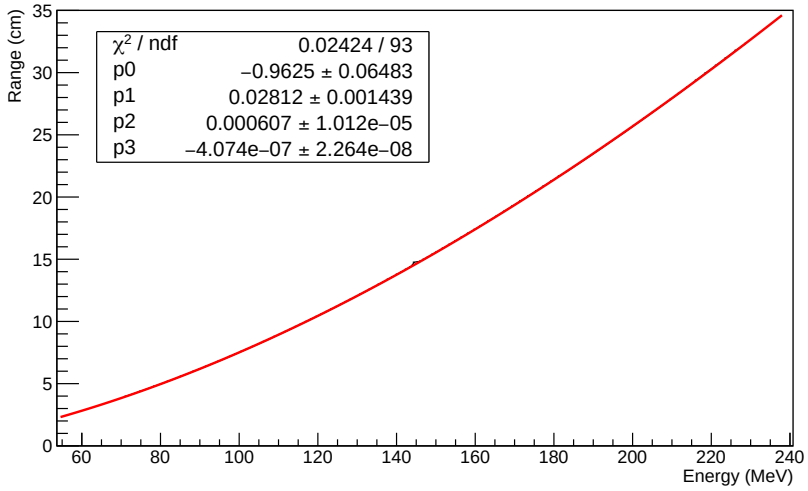

Figure 2: The proton projected range in water as calculated using PSTAR.

stopping power over the energy, however, since the particle will not in general take a straight path and the range is defined as the path length along the beam axis, the path length will always be greater than the range. This is however, a very small effect at clinical energies (.9988 at 100 MeV [32]), hence the range can be calculated by integrating over the inverse stopping power,

$$R(E) = \int_0^E \left(\frac{dE'}{dx}\right)^{-1} dE' \tag{1.20}$$

$$\approx \int_0^E CE'\, dE' = CE^2 \tag{1.21}$$

$$R(E) \propto E^2 \ . \tag{1.22}$$

Making some approximations to solve for the range, equation (1.22) can be helpful as a rule of thumb for predicting ranges.

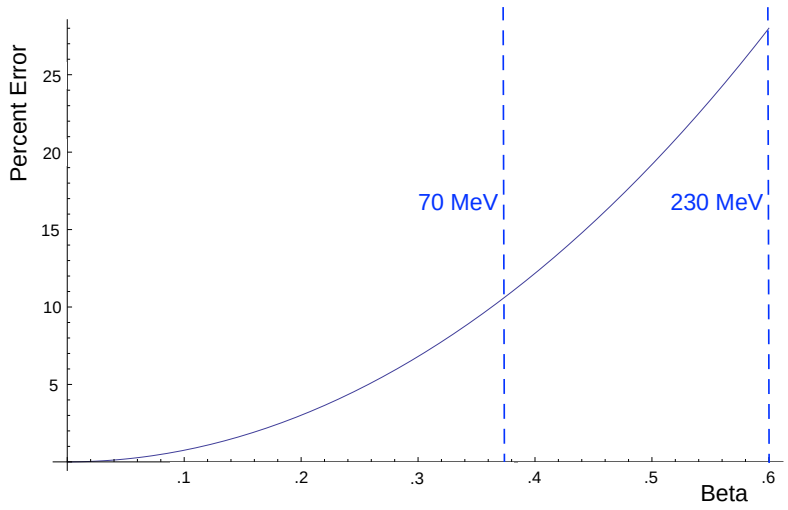

Figure 3: Comparison between classical and relativistic kinetic energy for protons in the clinical regime

1.1.3 Range Straggling and the Bragg Peak

To this point, particles have been considered to lose energy continuously and identically throughout the target material. In reality, the energy deposition is statistical in nature due to the discrete number of interactions along the trajectory. Imagine an ensemble of protons with equal energy incident on a material. These protons will endure a differing number of collisions based on probability, resulting in a statistical spread in energy. The more interactions endured, the larger the spread in energy. The distribution of energy spread causes the range of each proton within the identical ensemble to be slightly different, an effect known as range straggling. Using GEANT4[1], a Monte-Carlo toolkit [3], the energy deposition vs depth was simulated taking into

[1]in all references to the GEANT4 simulation toolkit for this work, the reference physics list used is QGSP_BIC_HP

account the range straggling effect, resulting in accurate Bragg curves shown in Figure 4. The peak near the end of range is known as the Bragg Peak.

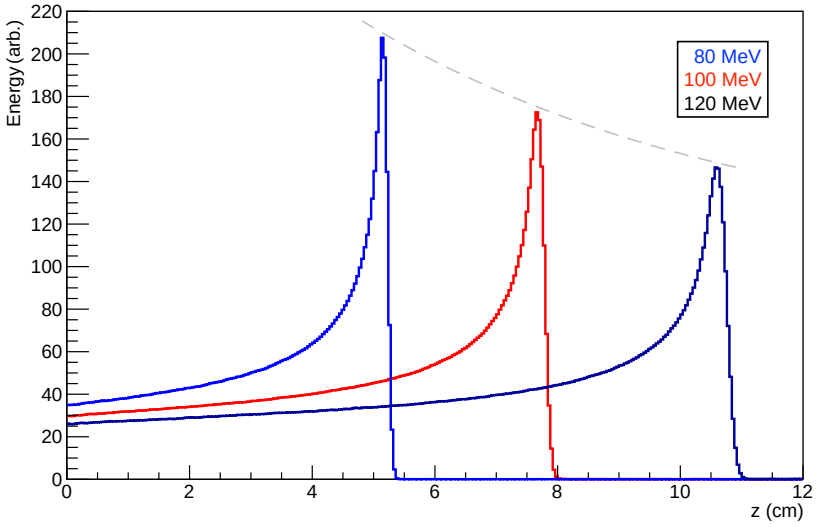

Figure 4: The Energy Deposited (arbitrary units) vs. Depth (cm) simulated in GEANT4. The range and straggling increases with energy.

1.2 Proton Deflection

We have so far concluded that the proton will lose energy predominantly through interactions with atomic electrons, resulting in an energy loss distribution characterized by the Bragg Peak near the end of range. In this section, we will now consider the trajectory of the proton as it traverses through a material. We will start with determining the largest scattering angle possible, ψ_{max}, for a proton incident on a stationary (in the lab frame) target. See Figure 5 for a diagram of the relevant parameters. In this scenario, the center of mass frame and the lab frame will be used

in order to exploit the fact that in the center of mass frame, the momentum is always zero and that $v'_{p,i} = v'_{p,f}$, $v'_{t,i} = v'_{t,f}$.

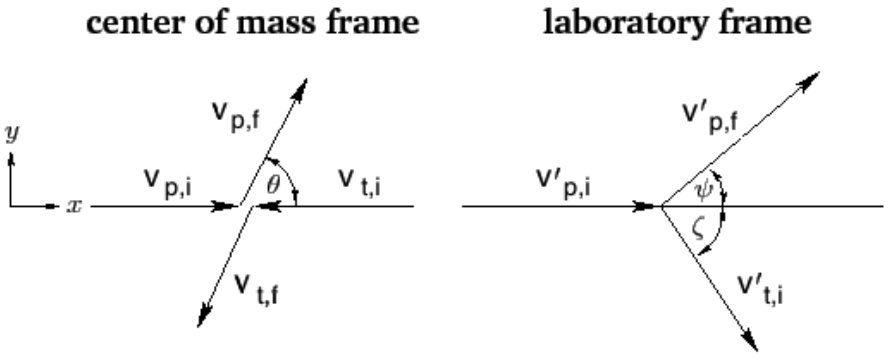

Figure 5: parameters for a two-body collision

We start with simple trigonometry to relate the lab frame scattering angle of the proton, ψ, to the lab frame scattering velocity, $v_{p,f}$,

$$\tan\psi = \frac{v_{p,f}\cdot\hat{y}}{v_{p,f}\cdot\hat{x}} \ . \tag{1.23}$$

Since the y-momentum in both frames is initially zero, the numerator of equation (1.23) is found to be $v_{p,f}\cdot\hat{y} = v'_{p,f}\sin\theta$, where θ is the scattering angle in the center of mass frame. $v_{p,f}\cdot\hat{x}$ can be related to the center of mass frame by boosting in the x-direction. The relative velocity between both frames is the velocity of the target in the center of mass frame before collision. Since the total momentum is always zero in the center of mass frame, we solve for the relative velocity,

$$m_p v'_{p,i} = m_t v'_{t,i} \tag{1.24}$$

$$v_{relative} = v'_{t,i} = v'_{p,i}\frac{m_p}{m_t} \ . \tag{1.25}$$

Now having the relative velocity, we can boost the lab frame velocity into the center

of mass frame and solve for the denominator of equation (1.23),

$$v_{p,f} \cdot \hat{x} = v'_{p,f} \cos\theta + v_{relative} \tag{1.26}$$

$$v_{p,f} \cdot \hat{x} = v'_{p,f} \cos\theta + v'_{p,i} \frac{m_p}{m_t} \ . \tag{1.27}$$

Since $v'_{p,i} = v'_{p,f}$, the velocities cancel leaving ψ to be solved in terms of only θ and the masses,

$$\tan\psi = \frac{\sin\theta}{\cos\theta + \frac{m_p}{m_t}} \ . \tag{1.28}$$

To find the maximum lab frame scattering angle, ψ_{max}, we take the derivative of equation (1.28)and set it equal to zero.

$$\frac{d\tan\psi}{d\theta} = \frac{1 + \frac{m_p}{m_t}\cos\theta}{\left(\cos\theta + \frac{m_p}{m_t}\right)^2} = 0 \ . \tag{1.29}$$

For ψ_{max}, $\cos\theta = -\frac{m_t}{m_p}$ (only defined for $m_p > m_t$). Therefore, plugging back into equation (1.28) and solving for ψ_{max},

$$\psi_{max} = \sin^{-1}\left(\frac{m_t}{m_p}\right) \ , \text{ for } m_p > m_t \ . \tag{1.30}$$

Otherwise, for $m_p < m_t$, such as for a target nucleus, there are no classical limits on the lab frame scattering angle. For a proton interacting with an electron, we calculate that the maximum scattering angle would be about .03°. For a proton colliding with a hydrogen nucleus, we have the special case where $m_t = m_p$, giving the maximum scattering angle of 90°. Although this result is not conclusive on its own, we can start to see that the deflection of a proton by a single nuclear interaction would have a much larger effect than the interactions with electrons.

1.2.1 Mean Free Path Using Screened Rutherford Scattering

We would like to calculate the mean free path of a proton incident on a volume of water. Since the mean free path can be calculated using the total cross section, $\lambda = 1/\sigma n_t$, we might try using Rutherford scattering. One problem with this approach is that the Coulomb potential has an infinite range and as a result, the cross section goes to infinity as the deflection angle approaches zero. Therefore, to solve for the mean free path, one would need to choose some minimum deflection angle. This choice in angle is highly arbitrary and therefore not a good parameter for determining the mean free path. Another complication lies in accounting for the nuclei and atomic electrons. To account for these complications, a "screened" potential is presented here,

$$V(r) = \frac{zZe^2}{r} e^{-r/a} \ , \tag{1.31}$$

also known as the screened Coulomb potential. Many screening potentials exist, all having the property of reducing much faster than the Coulomb potential at distances greater than a. Physically, the screened Coulomb potential (Equation 1.31) can be interpreted as the potential an incident particle experiences near an atom in a bulk material. The shell electrons screen the nucleus potential until the incident particle is within the screening parameter, a, which is on the order of the radius of an atom. We would now like to calculate the cross section of a proton experiencing the screened Coulomb potential starting with the scattering amplitude,

$$f(\theta) = -\frac{2\mu}{\hbar \Delta p} \int_0^\infty r' V(r') \sin\left(\frac{\Delta p}{\hbar} r'\right) \, dr' \tag{1.32}$$

$$= -\frac{2\mu z Z e^2}{\hbar \Delta p} \int_0^\infty e^{-\frac{r'}{a}} \sin\left(\frac{\Delta p}{\hbar} r'\right) \, dr' \tag{1.33}$$

$$= \frac{zZe^2}{\hbar^2/2\mu a^2 + \Delta p^2/2\mu} \ . \tag{1.34}$$

For elastic scattering, we can take $\Delta p = 2p \sin\frac{\theta}{2} = 2\hbar k \sin\frac{\theta}{2}$, thus giving

$$f(\theta) = \frac{zZe^2}{\frac{\hbar^2}{2\mu a^2} + 4E\sin^2\left(\frac{\theta}{2}\right)} \ , \tag{1.35}$$

where $E = \hbar^2 k^2/2\mu$. Squaring the scattering amplitude gives the differential cross section for the screened potential,

$$\frac{d\sigma}{d\Omega} = \left| \frac{zZe^2}{\frac{\hbar^2}{2\mu a^2} + 4E\sin^2\left(\frac{\theta}{2}\right)} \right|^2 \ . \tag{1.36}$$

Notice that by taking $a \to \infty$, the differential cross section for the screened potential goes to Rutherford scattering. The total cross section can be calculated by integrating over the differential cross section,

$$\sigma = \frac{16\pi\mu^2 z^2 Z^2 e^4 a^4}{\hbar^4} \frac{1}{1 + 8\mu E a^2/\hbar^2} \ . \tag{1.37}$$

For $E >> \frac{\hbar^2}{8\mu a^2}$, true for a on the order of atomic lengths, equation (1.37) can be simplified,

$$\sigma = \frac{2\pi\mu z^2 Z^2 e^4 a^2}{E\hbar^2} \tag{1.38}$$

Now having a total cross section which does not depend on the deflection angle, we can calculate the mean free path. First, however, we must calculate the target density, n_t. Since water consists of 18 nucleons per molecule, the number of molecules per kg $= \frac{N_A}{18 \text{ grams}} \frac{1000 \text{ grams}}{1 \text{ kg}} = 3.346 \times 10^{25}$ molecules/kg. Now, solving for the number of molecules per cubic meter where the density of water, $\rho = 1000$ kg/m^3, gives $n_t = \frac{3.346\times10^{25} \text{ molecules}}{1 \text{ kg}}\rho = 3.346 \times 10^{28}$ molecules/m^3. An empirical equation for the screening parameter is $a = \frac{.8854 a_0}{z^{.23} + Z^{.23}}$, where a_0 is the Bohr radius [40]. Since water, a molecule, is not an atom, an estimate for the effective atomic number, Z_{eff}, based on empirical data suggests 7.42 as an appropriate choice [29]. See Table 1, which gives the total cross section and mean free path for elastic collisions between the proton and water molecules.

E (MeV)	σ (m^2)	λ (m)
1	1.30×10^{-20}	2.30×10^{-9}
10	1.30×10^{-21}	2.30×10^{-8}
100	1.30×10^{-22}	2.30×10^{-7}

Table 1: Total cross sections and mean free path calculated using a screened Coulomb potential for a proton interacting with water

These results for the cross section of a proton colliding with an atom support the assumption that a proton will interact at a much higher probability with the atom than with the nucleus.

1.3 Secondary Radiation Due To Nuclear Inelastic Interactions

Protons will rarely interact with nuclei in a bulk material, yet the interactions that do occur are significant because they change the direction of the protons and produce secondaries which can leave the target. Using GEANT4, a simulation was conducted to measure the number of nuclear interactions per proton for protons incident on a water phantom. Based on these results, plotted in Figure 6, we see that it is rare for more than one nuclear interaction to occur for each incident proton.

For protons in the clinically relevant range of energies, select interactions with nuclei commonly found in organic materials are listed in Figure 7. Generally, only neutral secondaries will escape the target.

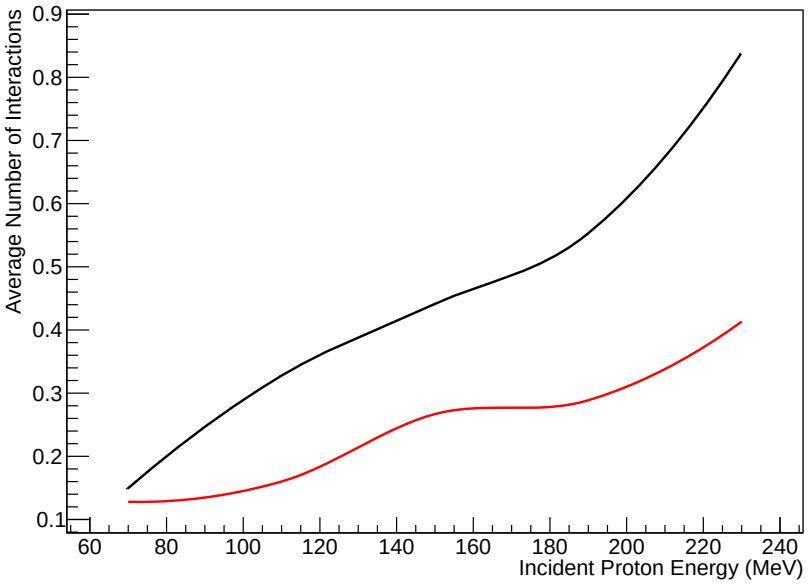

Figure 6: The number of nuclear interactions for protons being shot into a water phantom. Black = elastic collisions, Red = inelastic collisions.

E (MeV)	Transition	Reaction	Mean Life (s)
0.718	$^{10}B^{*0.718} \rightarrow$ g.s.	$^{12}C(p,x)^{10}B^{*}$	1.0×10^{-9}
		$^{12}C(p,x)^{10}C(\varepsilon)^{10}B^{*}$	27.8
		$^{16}O(p,x)^{10}B^{*}$	1.0×10^{-9}
0.937	$^{18}F^{*0.937} \rightarrow$ g.s.	$^{16}O(^{3}He,p)^{18}F^{*}$	6.8×10^{-11}
1.022	$^{10}B^{*1.740} \rightarrow {}^{10}B^{*0.718}$	$^{12}C(p,x)^{10}B^{*}$	7.5×10^{-15}
		$^{16}O(p,x)^{10}B^{*}$	7.5×10^{-15}
1.042	$^{18}F^{*1.042} \rightarrow$ g.s.	$^{16}O(^{3}He,p)^{18}F^{*}$	2.6×10^{-15}
1.635	$^{14}N^{*3.948} \rightarrow {}^{14}N^{*2.313}$	$^{14}N(p,p')^{14}N^{*}$	6.9×10^{-15}
2.000	$^{11}C^{*2.000} \rightarrow$ g.s.	$^{12}C(p,x)^{11}C^{*}$	1.0×10^{-14}
2.124	$^{11}B^{*2.125} \rightarrow$ g.s.	$^{12}C(p,x)^{11}B^{*}$	5.5×10^{-15}
2.313	$^{14}N^{*2.313} \rightarrow$ g.s.	$^{14}N(p,p')^{14}N^{*}$	9.8×10^{-14}
		$^{16}O(p,x)^{14}N^{*}$	9.8×10^{-14}
2.742	$^{16}O^{*6.872} \rightarrow {}^{16}O^{*6.130}$	$^{16}O(p,p')^{16}O^{*}$	1.8×10^{-13}
3.736	$^{40}Ca^{*3.736} \rightarrow$ g.s.	$^{40}Ca(p,p')^{40}Ca^{*}$	2.9×10^{-11}
4.438	$^{12}C^{*4.439} \rightarrow$ g.s.	$^{12}C(p,p')^{12}C^{*}$	6.1×10^{-14}
		$^{14}N(p,x)^{12}C^{*}$	6.1×10^{-14}
		$^{16}O(p,x)^{12}C^{*}$	6.1×10^{-14}
4.444	$^{11}B^{*4.445} \rightarrow$ g.s.	$^{12}C(p,2p)^{11}B^{*}$	5.6×10^{-19}
		$^{14}N(p,x)^{11}B^{*}$	5.6×10^{-19}
5.105	$^{14}N^{*5.106} \rightarrow$ g.s.	$^{14}N(p,p')^{14}N^{*}$	6.3×10^{-12}
		$^{16}O(p,x)^{14}N^{*}$	6.3×10^{-12}
5.180	$^{15}O^{5.181} \rightarrow$ g.s.	$^{16}O(p,x)^{15}O^{*}$	$< 4.9 \times 10^{-14}$
6.129	$^{16}O^{*6.130} \rightarrow$ g.s.	$^{16}O(p,p')^{16}O^{*}$	2.7×10^{-11}
6.916	$^{16}O^{*6.917} \rightarrow$ g.s.	$^{16}O(p,p')^{16}O^{*}$	6.8×10^{-15}
7.115	$^{16}O^{*7.117} \rightarrow$ g.s.	$^{16}O(p,p')^{16}O^{*}$	1.2×10^{-14}
15.10	$^{12}C^{*15.11} \rightarrow$ g.s.	$^{12}C(p,p')^{12}C^{*}$	1.5×10^{-17}

Figure 7: Select nuclear interactions (organic elements) as taken from Kozlovsky et al [22]

Chapter 2

PROTON THERAPY

Proton therapy is a medical treatment which consists of using a proton beam to irradiate cancerous tumors. Typical energies in proton therapy are between 40 MeV up to 300 MeV with ranges as low as a couple cm and up to 30 cm in water. Robert R. Wilson is credited with the idea to use protons as a form of treatment in 1948. Although the treatment is not new, proton therapy required many years of advancement before becoming the viable treatment it is today. Proton therapy is now gaining popularity with more than 160 facilities planned, under construction, or in operation throughout the world and more than 40 facilities in the United States alone, see Figure 8.

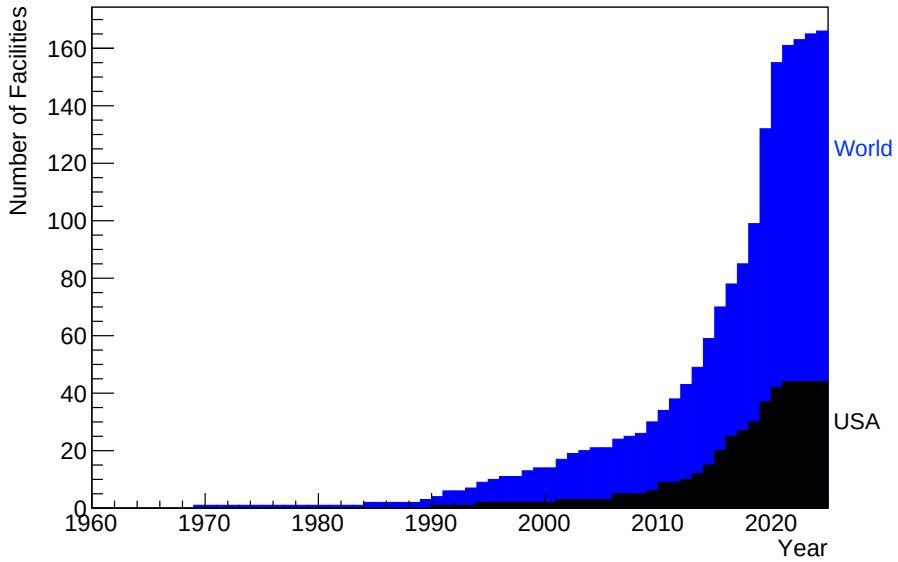

Figure 8: The cumulative number of proton therapy facilities over time as of Jan 2019 (Numbers obtained from PTCOG.ch)

In this section, a background of proton therapy will be given with a focus on the challenges which must be overcome for the treatment to reach its full potential.

2.1 Proton vs. Photon

Two fundamental advantages proton therapy offers over conventional photon therapy include (1) a dose-depth curve featuring a finite range that ends in vivo thus allowing for negligible dose distal to the target, and (2) highly localized energy deposition thus contributing to larger relative biological effectiveness (RBE) since protons have interaction lengths on the order of nanometers at the Bragg Peak (shown in Section 1.2.1). A plot showing dose-depth profiles for various particle-types and energies is given in Figure 9 [38].

Ideally, the sharp distal fall off of the proton dose-depth curve could be used to spare sensitive tissue while delivering the maximum dose to the tumor. Precise knowledge of the location of the distal fall off is therefore extremely important, however, the location of the Bragg Peak can only be known to within some degree of uncertainty, usually between 1 mm and up to 1 cm under poor conditions. Conventional photon therapy can be planned more precisely, since there is no range uncertainty as the beam passes through the body. Additionally, photon and electron based treatments are more mature. So, although protons have a fundamental physics advantage over photons in the context of radiation therapy, range uncertainty forces doctors to use low risk, suboptimal treatment plans [32]. As range uncertainty is minimized, doctors can treat patients more aggressively, unlocking the full potential of proton therapy. Range uncertainty remains one of the biggest obstacles facing proton therapy today [21].

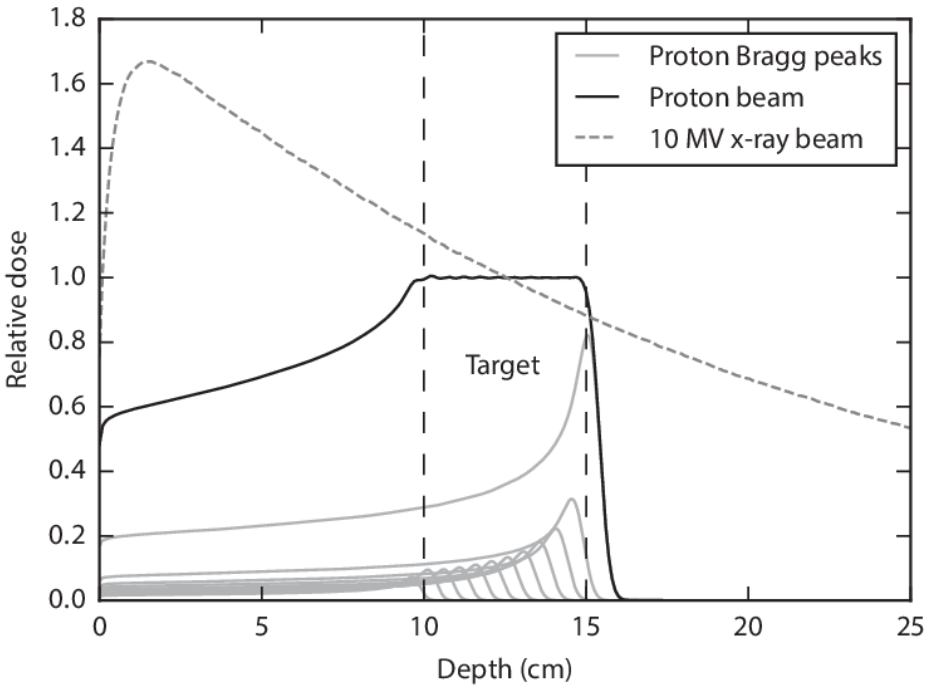

Figure 9: The Relative Dose vs. Depth for different types of delivery modalities. Image taken from Verburg [38].

2.2 Causes of Range Uncertainty

In order to reduce range uncertainty, the causes must be well understood. The major causes of range uncertainty [21] are:

1. Systematic errors to do with the process of relating CT scan results to proton range - 3% of range
2. Random errors in patient positioning or movement with each treatment
3. Random/systematic errors to do with a changing patient anatomy over the course of treatment (weeks)

Along with limiting each cause of range uncertainty directly, measuring the range with external devices may be part of the solution.

2.3 Accelerator Types: Synchrotron and Cyclotron

Two types of accelerators are common to proton therapy, the synchrotron and the cyclotron. The cyclotron works by holding a constant magnetic field, B, across the "Dees" as shown in Figure 10. The two "Dees" are held at a potential difference which switches as the particle passes from one to another. Charged particles are injected near the center resulting in a semi-circular path outwards where the peak energy is reached at the outer edge, radius R. The "cyclotron frequency", f, is found by setting the centripetal force equal to the Lorentz force and dividing by the circumference and is given here,

$$f = \frac{qB}{2\pi m_0 \gamma} = \frac{qBc^2}{2\pi E} \ . \tag{2.1}$$

Because the electric field switching frequency is dependent on the velocity (purely a relativistic effect) the frequency can only be held constant for non-relativistic particles, ie $\gamma = 1$. Due to the periodic nature of the accelerating mechanism, the particles will bunch together in time at values on the order of nanoseconds. For a 230 MeV beam with a 5 Tesla magnet (IBA S2C2, Numbers taken from The CERN Accelerator School, Austria 2015), a frequency of 61 MHz (16 ns period) is found respectively. Although the beam is bunched, a cyclotron is typically said to be continuous, possibly for two reasons: (1) At time scales much greater than nanoseconds, the beam will appear to have a continuous intensity and (2) the accelerator can be injected continuously unlike other types of accelerators such as the synchrotron.

A synchrotron is similar to the cyclotron in that it accelerates particles periodically, however, in a synchrotron, the path is fixed and the electromagnetic fields change over time. As the particle gains energy in the loop the magnets must apply a stronger

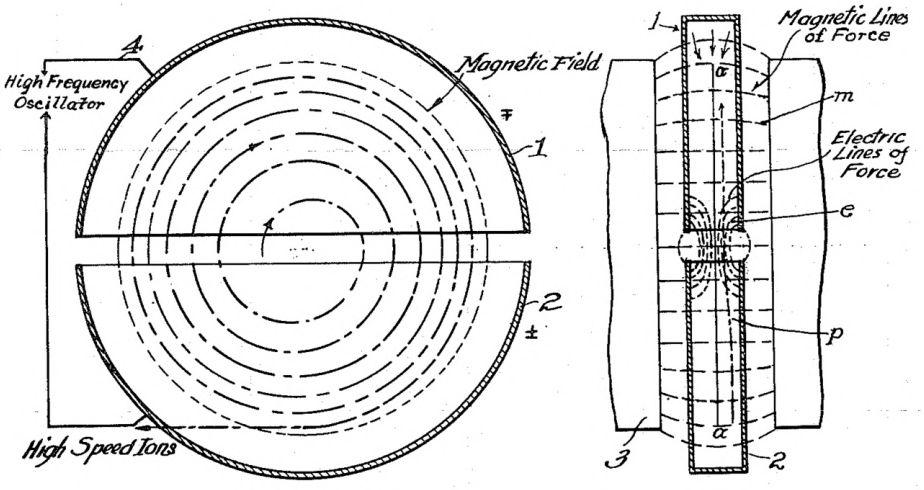

Figure 10: The workings of a cyclotron as shown in Ernest Lawrence's patent application, a technology for which he won the Nobel Prize in 1939

field with each pass. In this way, the entire system is "synched", hence the name. The timing structure of a synchrotron beam will be a result of the RF cavity accelerators, the natural bunching due to the timing of magnets, and the extraction method. For this reason, the timing will usually have a hierarchical structure.

Both cyclotrons and synchrotrons have advantages and disadvantages in the context of proton therapy. The size of the cyclotron is typically smaller than that of a synchrotron. The energy of exiting particles in a cyclotron is fixed and therefore must be attenuated to lower energies, thus leading to secondary radiation. Contrary to the cyclotron, the synchrotron can produce a continuous range of energies, thus avoiding secondary radiation as caused by attenuation.

2.4 Pencil Beam Scanning

Proton therapy has been steadily improving over time. In the past decade, pencil beam scanning (PBS) has become the new standard modality with nearly all new

facilities using the technology. PBS is a simple and yet profound way to conform the dose to a tumor. In passive scanning, material is used to attenuate and/or collimate a large cross-sectional area beam as a means of conforming to the tumor. This method requires careful engineering of the attenuation materials to ensure a highly targeted dose. PBS requires no passive attenuation to conform the beam. Instead, a small cross-sectional area beam on the order of a cm in diameter raster scans the tumor. The beam targets one small part of the tumor, turns off, then moves to the next point, turns on again and repeats. Each discrete shot of the beam is termed a "spot". Each point in space may receive many spots. The magnets control the (x, y) position and the beam energy controls the depth, z. Each discrete depth is called a "layer". The dose from all the points in (x, y, z) are "patched" together to form the conformal dose [21].

2.5 Mayo Clinic Proton Therapy Facility in Phoenix, AZ

The Mayo Clinic Proton Therapy Facility in Phoenix, AZ is one of four facilities with the Hitachi PROBEAT proton therapy system in the United States. The PROBEAT system at MD Anderson Cancer Center in Houston, TX has been described by Smith et al [35]. The PROBEAT system uses a synchrotron to accelerate the protons. Patient tumors are targeted by the beam using a magnetic aiming system (active scanning). The beam raster scans the tumor in a process known as pencil beam scanning (PBS) as previously described. The synchrotron is hidden behind a 6 foot thick concrete wall to protect patients and staff from any secondary radiation produced by the accelerator. The combination of a synchrotron accelerator, active beam scanning,

and thick concrete shielding ensures the lowest possible flux of secondary radiation in and around the treatment area.

2.5.1 PROBEAT Synchrotron Accelerator Extraction

The synchrotron ring, having a circumference of 18 meters, is filled by a linear accelerator with a finite number of protons, each having energy of around 3.5 MeV. The RF cavity is tuned to the revolution frequency of the protons, $f_{RF} = \frac{v}{l} = \frac{c}{l}\sqrt{1 - \left(\frac{m_p c^2}{E}\right)^2}$, where v is the particle velocity, l is the path length of one loop, c is the speed of light, E is the total energy, and m_p is the mass of the particle. For the Mayo Clinic facility, $f_{RF}(70 \text{ MeV}) = 6$ MHz and $f_{RF}(230 \text{ MeV}) = 10$ MHz. The synchrotron RF cavity has a large tune factor (low-Q) to accommodate for the large range of proton energies used in proton therapy, between 70 MeV and 230 MeV, where tune is defined as $\frac{\Delta f_{RF}}{f_{RF}}$. The large tune factor causes a spread in the momentum of the protons, $\frac{\Delta f_{RF}}{f_{RF}} \propto \frac{\Delta p}{p_0}$ [13], leading to longitudinal beam oscillations centered around the revolution frequency. The longitudinal beam oscillations can manifest themselves in the beam current as beat frequencies.

After a finite number of protons have been accelerated to the specified energy, protons are extracted from the synchrotron ring and sent to the patient room. A dose monitor controls the extraction, turning the extraction on/off based on the integrated dose measured by the dose monitor. A unit of dose in the dose monitor is termed the "monitor unit" (MU), which is calibrated to dose and differs from facility to facility. The dose is delivered in "spots", which typically last around 5 ms and contain around 10^7 protons ($\sim$0.1 MU at Mayo Clinic in Arizona). This method of extraction, known as slow extraction, ensures a highly controlled dose delivery.

In summary, the dominant beam current features are (1) the RF cavity frequency ($\tilde{1}$0 MHz), (2) beat frequencies ($\tilde{\text{k}}$Hz) due to longitudinal oscillations caused by a spread in the proton momentum within the synchrotron, and (3) the dose monitor spot extraction frequency ($\tilde{1}$00 Hz). Figure 11 shows the measured shape of a typical spot delivered by the PROBEAT system.

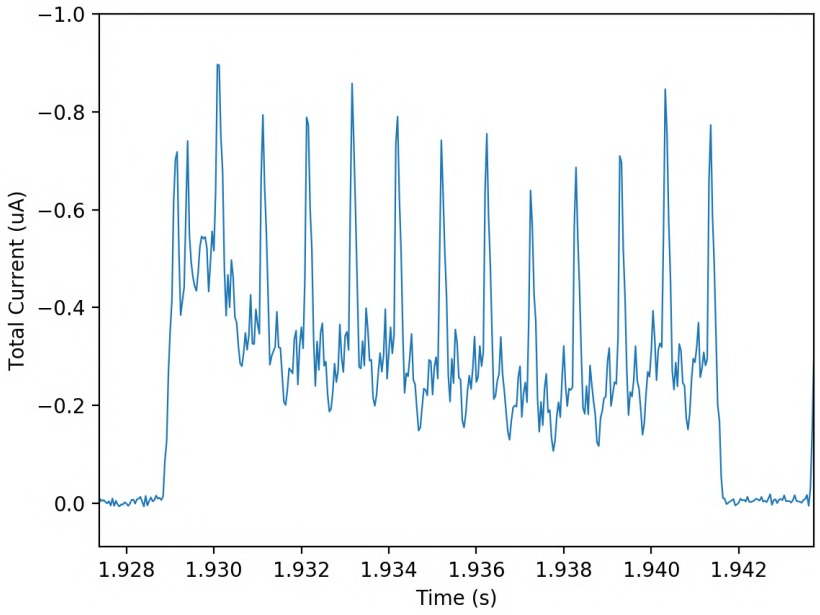

Figure 11: The shape of a single beam spot as measured by a P10 gas gridded ionization chamber. The measured value is detector ionization current versus time for a 151.9 MeV 0.1 MU spot. The spot duration is about 14 ms.

2.5.2 Active vs. Passive Scanning

Regardless of accelerator type, once the beam has been transported to the treatment room, it arrives with uniform energy and position. A beam of this nature is not

clinically relevant alone. The beam characteristics must be manipulated so the dose can be distributed to the contour of the tumor. There are generally two methods of controlling the beam, either by strong magnetic fields (active) or by placing material in the beam path (passive) to attenuate, block, or conform the beam. Active scanning has the advantage of producing less secondary radiation as compared to passive techniques.

2.6 Treatment Planning and Quality Assurance

Beyond being able to measure the proton range, the problem of having reliable external measurements that can offer immediate treatment feedback continues to allude proton therapy. Currently, oncologists and medical physicists mostly depend on robust treatment planning and careful beam verification procedures to assure the quality of care. The quality assurance (QA) philosophy in proton therapy is to ensure beam predictability by constricting the beam performance with a multi phase measurement approach. If the beam performance is within tolerance over a set of measurements, then the beam is considered to be adequately described by analytical approaches. Each of these constricting measurements occurs outside of patient treatment. There are typically no measurements made during treatment external to the dose monitoring log files. In order to ensure a highly controlled dose delivery during treatment, proton therapy needs to mature to include external treatment measurements such as range detection and dose monitoring.

2.6.1 Treatment Planning

Treatment planning begins with a CT scan to determine the precise location of the tumor. A CT scan is a measure of the electron density since x-ray linear attenuation is a function of the electron density in a non-crystalline material. Using the CT scans, the x-ray attenuation is converted to proton stopping power. Similar to conventional radiation therapy, many fields (beam angles and entrance points) can be used in order to minimize the dose to non-target tissues. Given certain input parameters, a computer program will determine an optimal plan. Range uncertainty is accounted for in treatment planning by (1) introducing a margin (a beam overshoot to ensure tumor coverage), and (2) avoiding fields that terminate at critical structures as demonstrated by Figure 12 [21]. A typical margin used in the clinic is the prescribed range + 3.5% + 1 mm, which can exceed the prescribed range by more than 7 mm at commonly used depths [31]. The margin is an input to the treatment planning software and as range uncertainty is minimized, smaller margins can be used thus regaining some of the advantages offered by proton therapy.

Once a treatment plan is approved, treatment of the patient may begin. Although multiple treatment plans over the course of treatment would be ideal, it is not common. In most cases, a single treatment plan will be produced to be used over the entire course of treatment. The entire treatment plan is composed of 5 to 20 "fractions", where 1 fraction is delivered to the patient in each visit.

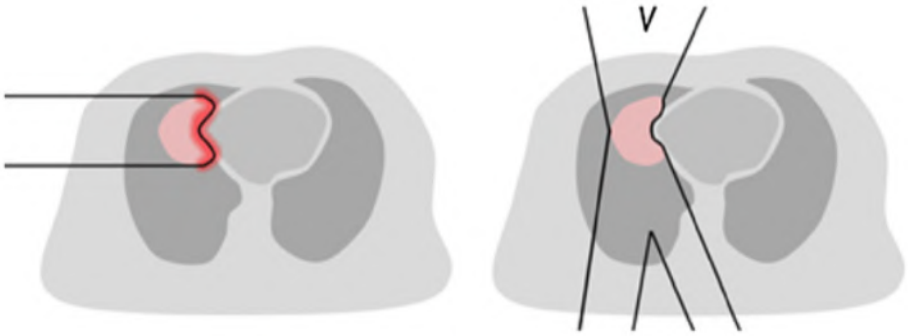

Figure 12: Left: the optimal, yet high risk, plan for minimizing the total non-target dose. Right: A compromise in order to avoid dose to the critical structure. Image taken from Knopf and Lomax [21].

2.6.2 Patient-Specific Quality Assurance at the Mayo Clinic

The treatment planning software used by Mayo Clinic is Eclipse for Proton written by Varian [1]. The treatment plan consists of the beam energies, x-y positions, and gantry angles which will deliver the planned dose. The dose distribution is calculated analytically or by Monte Carlo and so uncertainty in translating the x-ray images into proton stopping power introduces uncertainty in the dose distribution. After the treatment plan has been optimized, the planned dose distribution delivered by the proton beam can be overlaid with a three dimensional patient image from the CT scan, see Figure 13. Each treatment plan goes through a verification measurement process called patient-specific QA.

In order to perform patient-specific QA, Eclipse tranforms the treatment plan into a new treatment plan for a water phantom. The transformation essentially removes the gantry angles and recalculates the new dose distribution for the featureless water phantom for each gantry angle. Having the patient plan transformed into a water phantom plan allows for checking for discrepancy between the planned dose with the

measured dose in a stationary water phantom. The measurement is performed by placing a 2D ionization chamber into an acrylic sleeve which scans along the beam axis inside the water phantom, shown in Figure 14. A 2D dose profile is measured at 3 strategic points along the beam axis. Each dose profile is compared to the calculated profile by Eclipse using the γ-index analysis [26]. An example 2D measured dose profile and a 2D calculated dose profile are shown in Figure 15. A more detailed overview of the patient-specific QA performed at Mayo Clinic in Arizona is outlined by Morales et al. [28].

Another patient-specific QA measure is an analysis of the log files from the dose monitor. Because the beam dose monitor keeps logs of the MU and spot positioning, the information can be used as input to recalculate the delivered dose after treatment [28]. In principle, however, having no external verification to the dose monitor during treatment is not ideal since a single measurement device may have problems, but two devices in agreement during treatment would ensure a more robust treatment.

2.6.3 Machine Quality Assurance at the Mayo Clinic

Machine QA is performed typically on a monthly basis outside of patient treatment times. The purpose is to directly confine the beam performance to within tolerance for spot positioning, spot size, and range for a variety of beam configurations.

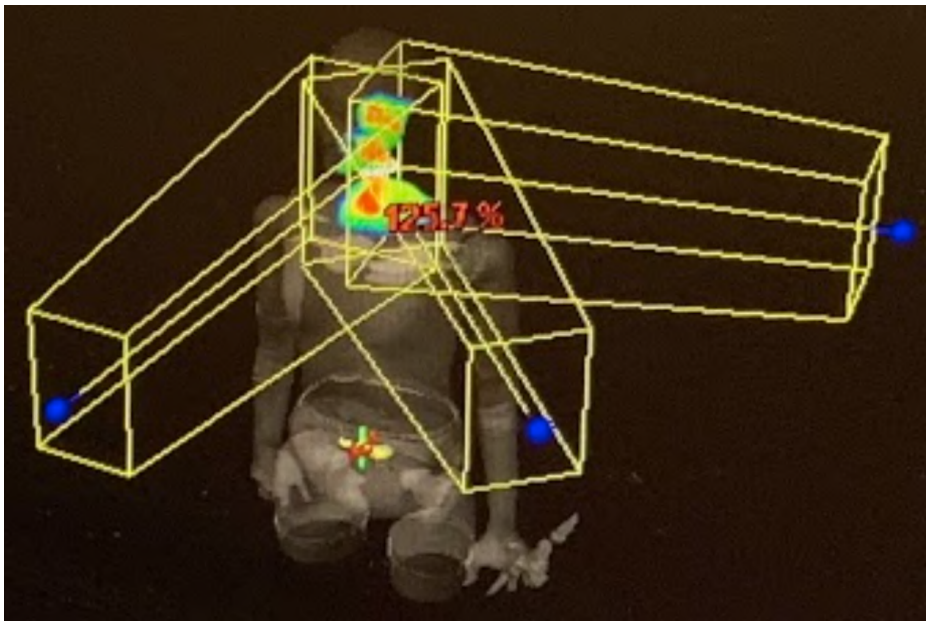

Figure 13: A three dimensional view of the planned dose overlaid with the patient CT scan (not a real patient shown).

Figure 14: The DigiPhant scanning water phantom which houses the MatriXX 2D segmented ionization detector. The beam axis runs parallel to the shown the z-axis.

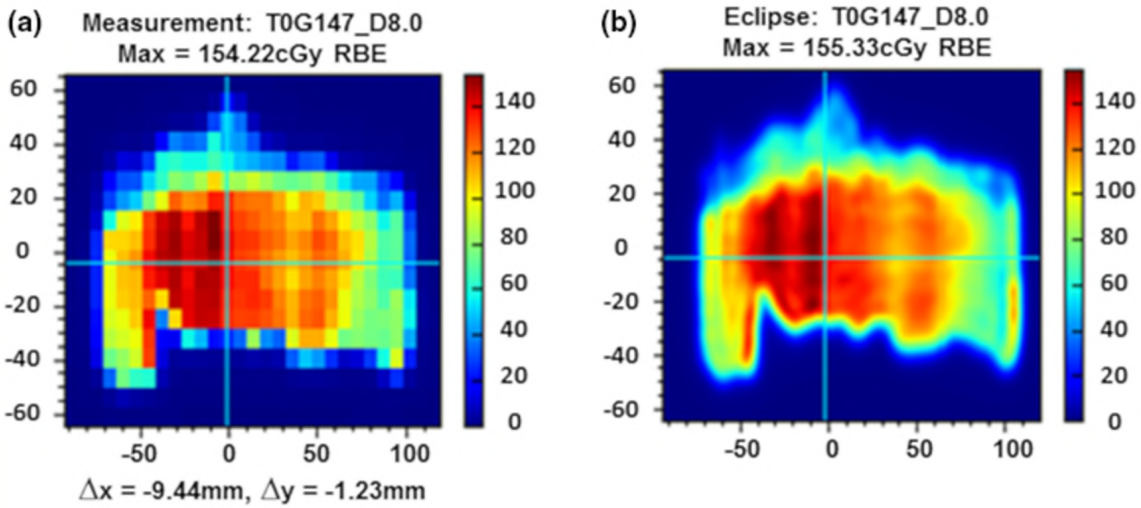

Figure 15: The measured dose profile by the IBA MatriXX segmented ionization chamber and the Eclipse-calculated dose profile. Patient-specific QA involves comparing many of these types of plots for a treatment plan. Image taken from Morales et al. [28]

Chapter 3

MEASURING THE PROTON RANGE USING PROMPT GAMMA-RAYS

There are a few ways to reduce range uncertainty in proton therapy. The most direct approach is by measuring the proton range during treatment. As protons traverse through the patient, occasional nuclear collisions result in a gamma-ray or neutron exiting the patient. One method for measuring the proton range in-vivo during treatment is to reconstruct the proton beam by detecting the gamma-rays that are promptly emitted after a nuclear collision. By determining the position where the prompt gamma-rays originated, the proton range can be reconstructed [27]. Measuring the proton range using prompt gamma-rays is an active area of research with many groups developing various detector designs [27] [37] [15] [23]. Even as range uncertainty has been recognized as one of the main challenges facing proton therapy, in-vivo range measurement has yet to be implemented in a meaningful way and remains an unsolved problem. In this work, a collimated array of gamma-ray detectors inspired by Min et al. [27] has been developed which can measure the range of the protons in a patient by detecting prompt gamma-rays emitted during proton therapy. The detector design motivation, an overview of the detector implementation, and measurement results from recent visits to the Proton Therapy Center at Mayo Clinic Arizona will be presented.

3.1 Monte-Carlo study of Nuclear Interactions in the Patient

Measuring the proton range using prompt gamma-rays requires a clear understanding of the underlying nuclear physics occurring in the patient. GEANT4 was used to study the detector flux, energy spectra, timing, and the correlation between proton range and the nuclear reaction products emitted from a patient. As is often done, this simulation uses a water volume as an approximation of a patient. This section will give an overview of the simulation results.

About 1 in 4 protons interacting within the patient results in a gamma-ray or neutron exiting the patient during treatment. Prompt gamma-rays emitted by the patient can be grouped in two categories: (1) those produced by (p,xγ) reactions with no neutrons in their interaction history and (2) those descended from a neutron at some point in its interaction history. These two types of prompt gamma-rays are distinct because the vertex location of prompt gamma-rays from (p,xγ) reactions are highly correlated with the proton range while prompt gamma-rays with neutrons in their track history are not. Using GEANT4, a water phantom was bombarded with 120 MeV protons. The resulting gamma-ray energies versus the position where they originated are shown in Figure 16a while Figure 16b shows the results for gamma-rays descended from a neutron. It is seen that some of the gamma-ray energies such as 4.44 MeV and 5.2 MeV produced by (p,xγ) reactions are highly correlated with the Bragg Peak while 2.22 MeV (neutron capture on hydrogen) and 6.13 MeV show no correlation. Because the discrete energy peaks are the result of known nuclear reactions, having a detector that can measure particle energy becomes essential for separating the gamma-ray processes. The energy spectra for both types of prompt

gamma-rays along with neutrons are shown in Figure 17 where important energy peaks are labeled by their corresponding nuclear reaction.

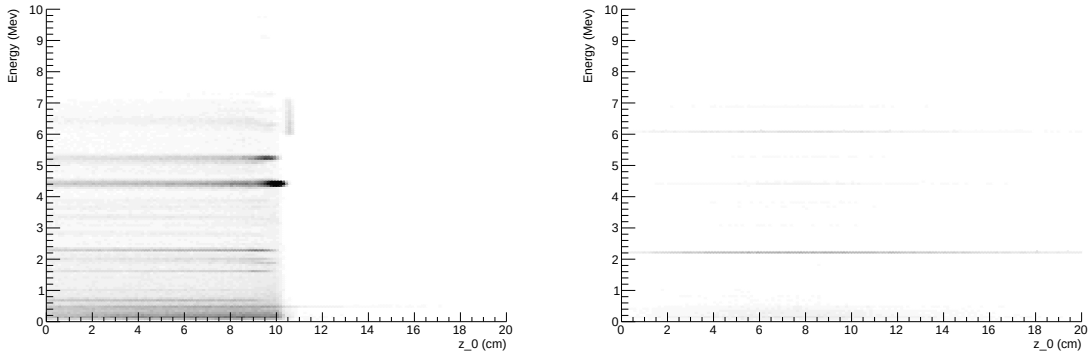

(a) (p,xγ) gamma-ray detector flux (b) neutron-induced gamma-ray detector flux

Figure 16: On the left, the energy and initial z-position are binned for (p,xγ) gamma-rays which escape a 16 cm x 16 cm x 40 cm water phantom as produced by a 120 MeV proton beam (simulated in GEANT4). On the right, only the gamma-rays produced by neutron processes are plotted. Gamma-rays produced by neutron processes are not correlated with the proton beam.

Direct neutrons and gamma-rays produced by neutrons in the patient amount to a substantial background flux for the range measurement. To illustrate the background, Figure 18 gives the partial detector fluxes for each particle type depending on the detector solid angle, the beam proton rate, and the beam energy (simulated by GEANT4). The arrival times of the prompt gamma-rays and neutrons are different since neutrons do not travel at the speed of light. The particles time of flight for a single bunch of protons shot into a water phantom are shown in Figure 19. The neutrons are seen to separate in time from the gamma-rays. An important interaction not captured in Figure 19 due to its short time scale is neutron capture on hydrogen in the patient, where the resulting 2.22 MeV gamma-ray time of flight has a time constant of about 60 microseconds as shown in Figure 20. This relatively slow 2.22

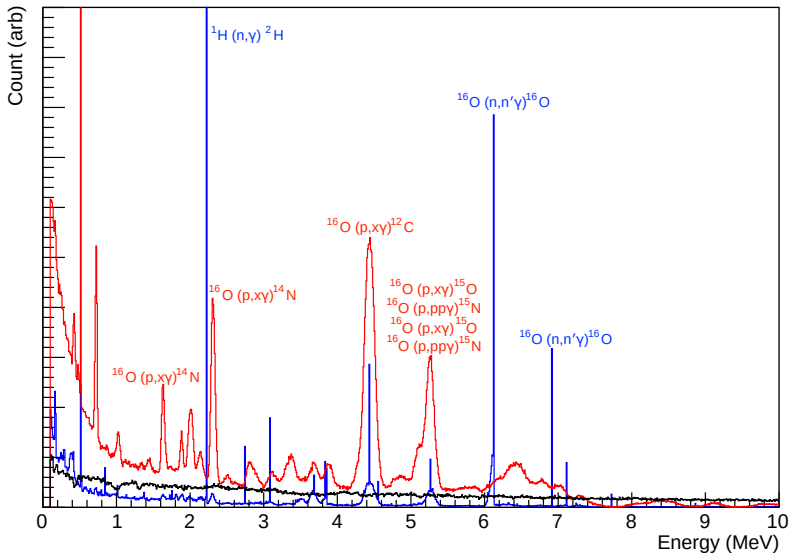

Figure 17: The energy spectra for gamma-rays produced by (p,xγ) (red), gamma-rays produced by processes involving neutrons (blue), and direct neutrons (black) as simulated by GEANT4 for a 120 MeV proton beam shot into a water phantom. Important energy peaks are labeled by the reaction.

MeV gamma-ray flux is the result of neutron thermalization in the patient occurring with a time constant of about 30 microseconds [18].

3.2 Response Time Requirements for a Prompt Gamma-Ray Range Detector

This work is primarily focused on prompt gamma-ray range detectors which have the intended purpose of providing feedback to the treatment system before a harmful amount of dose is delivered distal to the planned treatment volume. Complexity in measuring the proton range is reduced if the intended purpose is only to provide

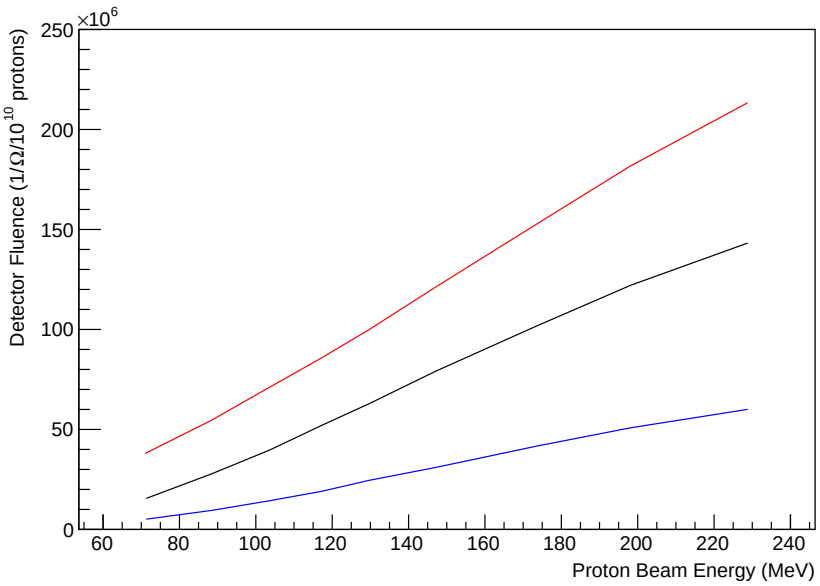

Figure 18: The particle rates at the detector for gamma-rays produced by (p,xγ) (red), gamma-rays produced by processes involving neutrons (blue), and neutrons (black) as simulated by GEANT4 for various proton beam energies into a water phantom.

corrections to the treatment plan for upcoming treatment fractions since longer integration times reduce noise in the measurement. Because having a short measurement time window increases the detector complexity, it is desired to estimate an adequate response time, where response time is defined as the minimum amount of time required to measure the proton range to within 1 mm.

In order to estimate an adequate detector response time, the dose that begins to cause health complications is estimated based on the 2011 study, Quantitative Analyses of Normal Tissue Effects in the Clinic (QUANTEC) [5]. Because the range detector is intended to prevent a harmful dose beyond the target, a lower limit for the dose that begins to cause harm is desired as a threshold for range measurement. Based on the QUANTEC dose/outcome summary, a lower limit on the dose that may

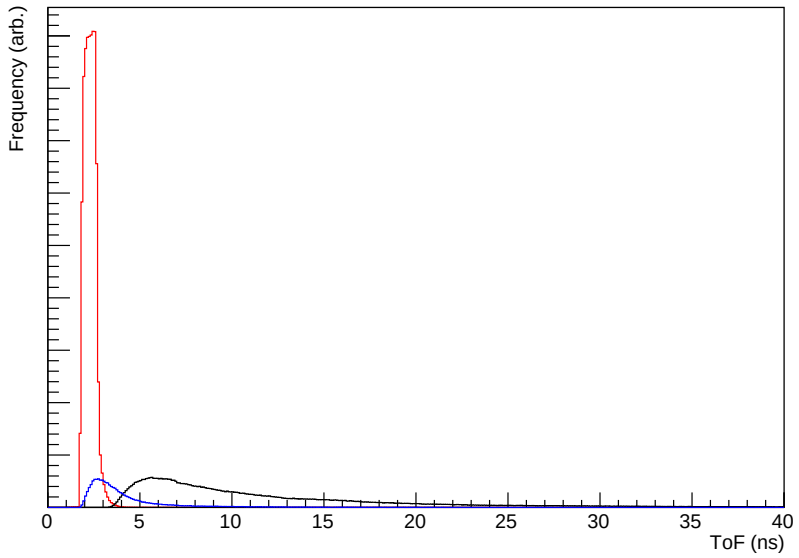

Figure 19: The time of flight for a single bunch of protons (delta function) shot into a water phantom. Gamma-rays produced by (p,xγ) (red), gamma-rays produced by processes involving neutrons (blue), and neutrons (black) are shown as simulated by GEANT4.

cause complications in healthy tissue is conservatively estimated to be 10 Grays over 10% of the tissue volume for a variety of organs.

Because of the sharp fall off in the dose deposition for protons near the end of range, even a small overshoot can provide harmful dose levels outside of the prescribed region. In the case of a 3 mm overshoot, protons deposit about 5% of their delivered dose distal to the target. Approximating over a range of proton energies, every 5 x 10^7 protons with a 3 mm overshoot deliver about 10 centigray outside the target volume. Since damage is estimated to begin after 10 Grays is delivered, damage to a critical structure due to a 3 mm overshoot begins to occur after about 1 second for typical proton therapy fluxes (10^{10} protons/s). It seems that a reasonable target for the response time of a proton range detector would be the time it takes to deliver

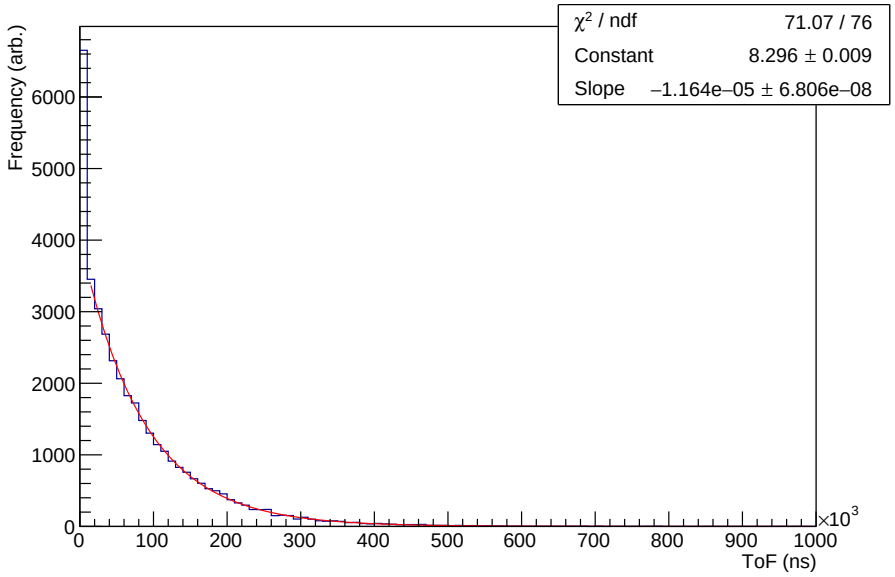

Figure 20: Time of flight for the neutron capture on Hydrogen gamma-ray line (2.22 MeV).

10-25% of the dose that may cause damage or 1 to 2.5 grays. Based on this estimate, a live feedback system would require the range detector to have a response time of 100-250 ms or less.

Chapter 4

DEVELOPMENT OF A COLLIMATED PROMPT GAMMA-RAY DETECTOR ARRAY

Challenges associated with measuring the proton range using prompt gamma-rays include short measurement times (100 ms), the neutron background, and high rate-handling requirements. The most common material used for detection of gamma-rays are high density inorganic scintillation crystals. For Thallium-doped Cesium Iodide (CsI (Tl)), the mean free path for gamma-rays is about 6 cm as shown in Figure 21, which was found using XFOR [30]. Depending on the incident energy, gamma-rays interact mainly through Compton scattering, the photoelectric effect, and pair production, with cross sections shown in Figure 22. Due to the large mean free path and the dominant interactions being Compton scattering and pair production for the most relevant prompt gamma-ray energies, the detector will often receive only partial energy deposit and a few hits per gamma-ray.

In proton beam reconstruction, two possibilities (or the combination thereof) exist for determining the origin of a gamma-ray, (1) by looking at multiple interaction gamma-ray events and using Compton scattering physics to determine the incident angle, or (2) using collimation to place a restriction on the allowed angles of acceptance for the incident gamma-rays. This work focuses on the use of collimation as a means of imaging.

The collimated prompt-gamma detector array concept design is shown in Figure 23. The detector consists of an array of CsI (Tl) scintillation crystals and an array

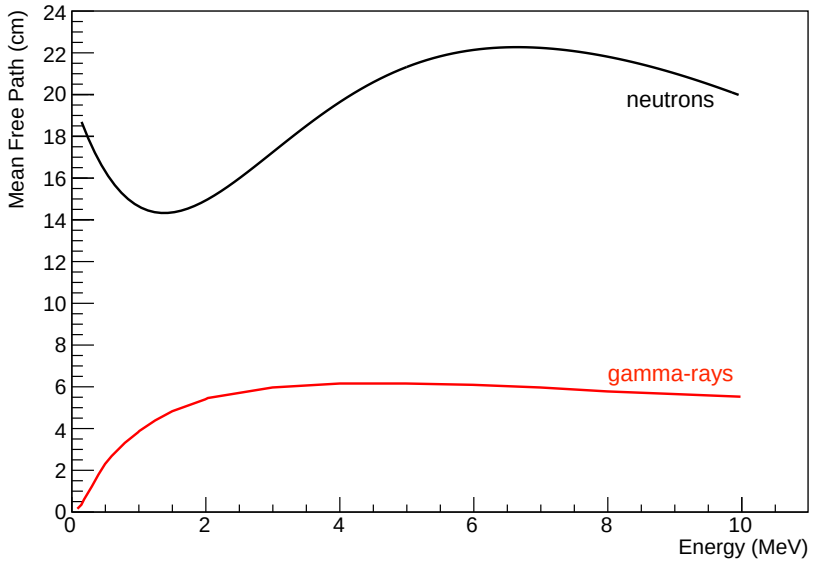

Figure 21: The mean free path in CsI (Tl) for gamma-rays (XCOM) and neutrons (EXFOR)

of tungsten collimation plates. The crystal pitch is 6.6 mm and the thickness of the collimation plates is 2.2 mm. For a single spot of protons, depending on the energy, there are between 800 and 40,000 gamma-rays incident on the detector, only a fraction of which make it through the collimation. For a 120 MeV proton beam, Figure 24 shows the loss in signal due to the collimation thickness for both gamma-rays and neutrons incident on the detector. The detector design must balance between collimation strength, the gamma-ray detection rate, and the neutron background, all of which contribute to uncertainty in the range measurement. In this section, an overview of the detector development and principles will be given.

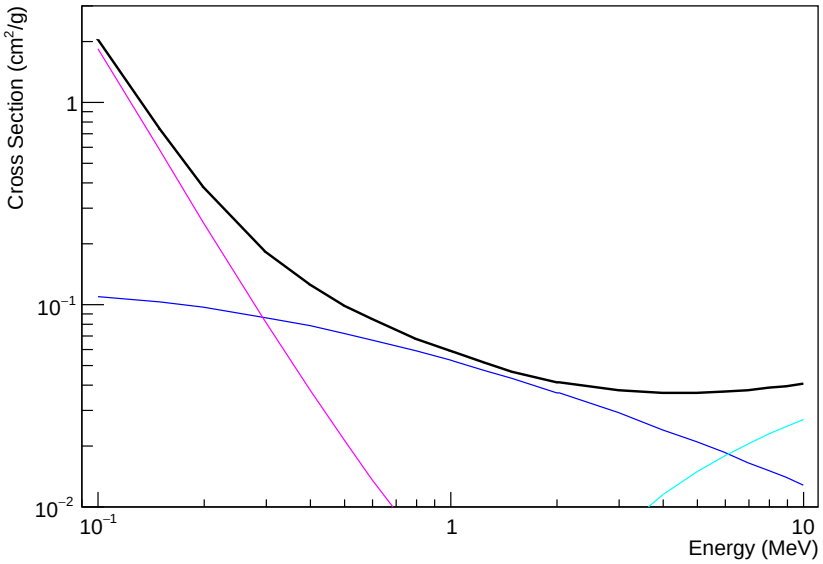

Figure 22: The total cross section (black) and partial cross sections according to interaction type including Compton scattering (blue), photoelectric effect (pink) and pair production (teal).

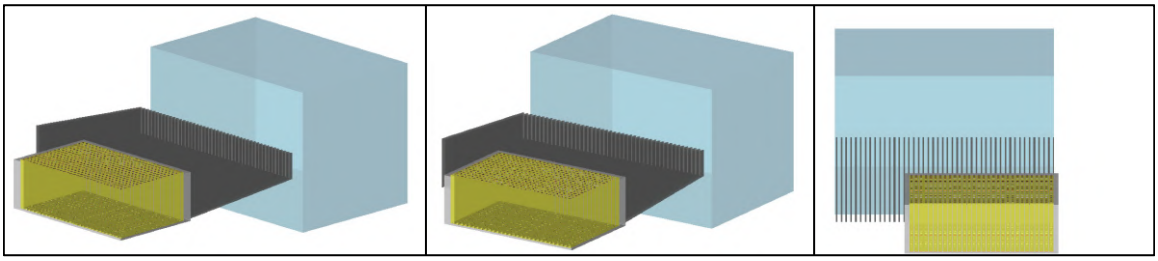

Figure 23: The collimated prompt gamma-ray detector array and a water phantom as simulated in GEANT4.

4.1 Collimation Array

The collimation serves to accept gamma-rays with momentum transverse to the beam axis. In reality, the collimation accepts a range of small angles about the transverse direction. Using a line of sight approach, the maximum accepted angle is $\theta_{max} = \arctan(p/d)$, where p is the spacing between each collimation plate and d is

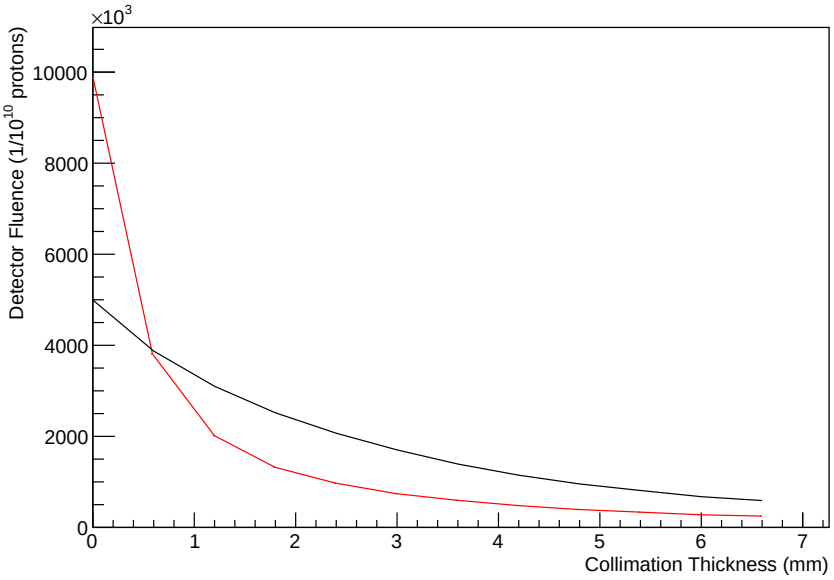

Figure 24: The gamma-ray and neutron fluence dependent on the amount of collimation (1 plate per crystal) for a 120 MeV proton beam.

the depth of the plates. Figure 25 shows the field of view drawn using line of sight for each crystal as a result of the collimation geometry parameters p and d. Each field-of-view region is shaded based on the amount of overlap in the fields of view for each respective crystal, hence lighter regions can be "seen" by more crystals. Because the regions further from the collimation can be "seen" by more of the detector, a photon emitted from the lighter regions cannot be reconstructed as precisely as the darker regions. Figure 25 demonstrates the first order importance of parameters p and d. d contributes to the depth of field while the aspect ratio p/d contributes to the field of view.

The situation is further complicated for gamma-rays since the collimation cannot restrict gamma-rays along the line of sight. Depending on the energy, a gamma-ray may pass through, absorb, or scatter off the collimation plates. To take into account

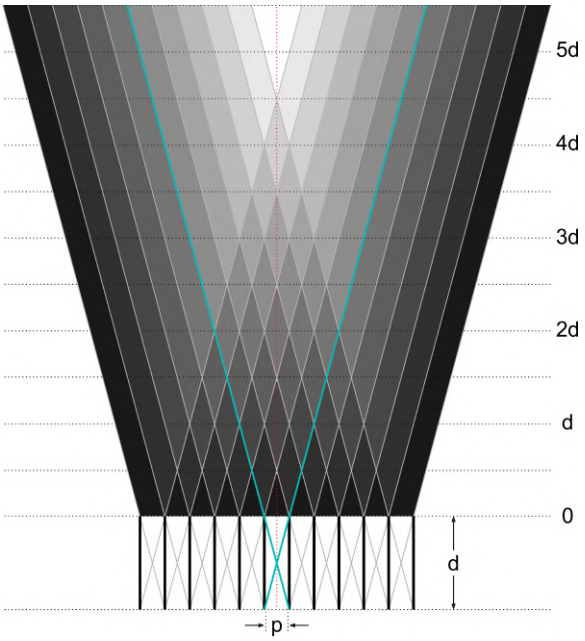

Figure 25: The field of view for a set of collimation plates with depth d and pitch p

the complexity of gamma-ray interactions with the collimation and in order to optimize the shape of the plates, a GEANT4 simulation has been produced.

4.1.1 Collimation Geometry Optimization

In designing an optimal collimation geometry, two important factors to consider are the collimation strength and the number of detected gamma-rays. Although having thicker, longer plates increases the collimation strength, the extra collimation material reduces the number of gamma-rays that reach the detector, thereby increasing the statistical uncertainty in the range measurement. In addition, shorter collimation plates allow the detector to be positioned closer to the patient, thereby collecting more gamma-rays. The collimation setup requires an optimization of the plates thickness and depth, which is outlined in this section.

In order to optimize the collimation plates geometry, the point spread function of

the collimation was examined by placing an isotropic point source at a fixed location of 10 cm in front of an infinite number of collimation plates with a 6.6 mm pitch. A diagram of the optimization setup is shown in Figure 26a. When the detector is hit, the z position is recorded and histogrammed. A sample histogram can be seen in Figure 27. The signal to noise ratio is calculated for the histogram. The signal to noise ratio is defined as $\frac{\int^{z_0} Countdz}{\sqrt{\int Count}}$, where z_0 is the crystal width also shown in Figure 27. The energy distribution of the source gamma-rays is the same as that of a water phantom being bombarded by protons of 80 MeV, but only those greater than 2 MeV. The signal to noise was calculated for various plate thicknesses and depths. The front of the collimation is always at 10 cm from the source, even when the collimation depth is changed. The detector is always directly behind the collimation making the detector closer to the source for shorter collimation depths and further for longer collimation depths. Figure 28 shows the signal to noise ratio found for various plate thicknesses and depths. There is a broad range of optimal configurations. In order to more closely approximate a line source similar to the gamma-rays emitted by a proton track, the same optimization was performed for a line source where the line is the same thickness as a single crystal, 6.6 mm, where the setup is shown in Figure 26b. The results are shown in Figure 29. Taking both analyses into account and attempting to choose a geometry which satisfies both, a plate with thickness 2.2 mm and depth of 20 cm was chosen. Figure 30 shows the actual collimation plates constructed from Tungsten and held in place with polyethylene spacers.

The collimation does not need to strictly be the same pitch as the crystal array.

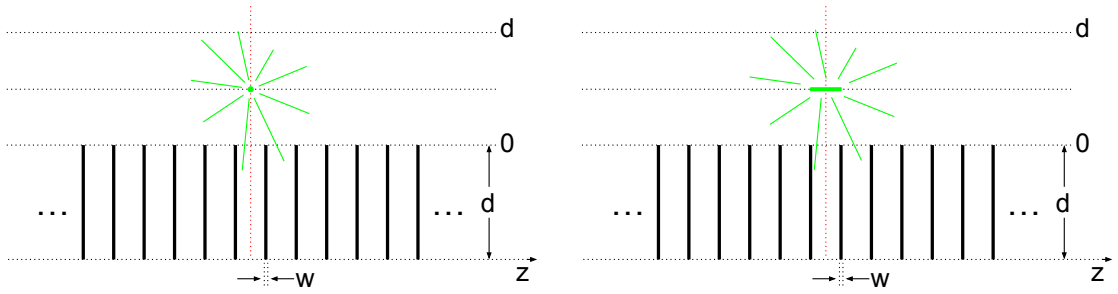

(a) point source optimization (b) line source optimization

Figure 26: The optimization setup for optimizing the w and d parameters, shown in the diagram. The gamma-ray source was either a point source (left) or line source (right) with energy distribution equal to a gamma-rays emitted by a water phantom irradiated by protons, but only those above 2 MeV.

The number of plates per crystal was varied while holding the total collimation mass constant to see if there could be any improvement in the signal to noise over using 1 plate per crystal. The results shown in Figure 31 indicate that the best option is to use 1 plate per crystal. To see if collimating in ϕ increase the signal to noise ratio, additional plates at different ϕ angles were incorporated into the simulation. In this case, Figure 32 shows that there may be a small improvement in collimating along ϕ, but probably not enough to overcome the added complexity in building such a setup.

As a summary of the collimation study, the collimation thickness and depth is not a super critical parameter as there are many configurations that can yield similar results. It does seem safe to conclude that having only 1 plate per crystal is the best scenario, which is a result of the much larger solid angle acceptance when the number of plates per crystal is 1 as compared to higher densities. In cases where the gamma-ray rates are higher than necessary for the measurement window, having thicker collimation plates may be a good choice.

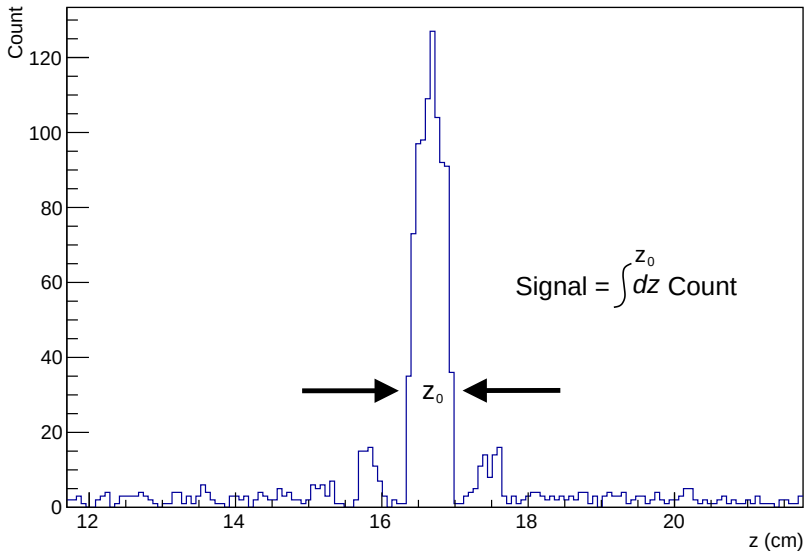

Figure 27: The signal to noise ratio definition and a sample measurement resulting from an isotropic point source sitting at 10 cm in front of the collimation opening.

4.1.2 Collimation Field of View for Gamma-rays

For 31 2.2 mm thick x 20 cm deep collimation plates (the sizes chosen for the real detector, see Section 4.1.1), a GEANT4 simulation was used for calculating the field of view and depth of field collectively just called the field of view. The spacing between each plate was 6.6 mm. A 4.4 MeV gamma-ray source was placed at grid points in the x-z plane, where z is the collimated axis, and x is the axis parallel with the plates. The grid points chosen were at increments of 6.6 mm along z and 10 cm increments along x. 600,000 gamma-rays were shot isotropically from each point. The initial z-positions and final z-positions are recorded for gamma-rays which successfully pass through the collimation.

The simplest method to quantify the field of view is to measure the probability

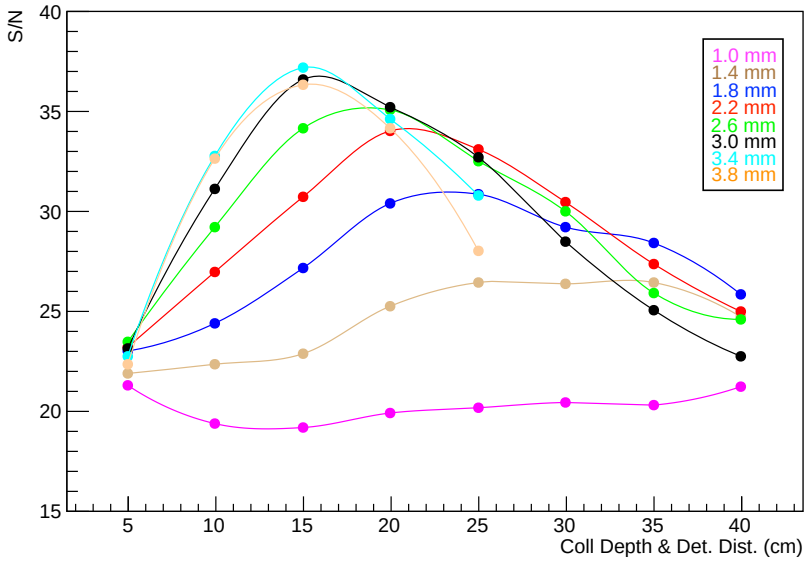

Figure 28: The signal to noise ratio calculated for varying collimation plates geometry resulting from gamma-ray point source.

at each grid point of a gamma-ray to reach the detector when emitted from that point. Figure 33a shows the probability of gamma-rays reaching the detector as a representation of the field of view. The probability of passing through the collimation reduces with distance, but at a rate slower than $\frac{1}{r}$. The collimation is also seen to restrict the gamma-rays to mostly directly in front of the collimation as intended.

Because the purpose of the collimation is to more specifically accept gamma-rays with momentum transverse to the beam axis, the signal to noise ratio as defined in Section 4.1.1 was calculated for gamma-rays emitted at points in the field of view. The usefulness of the collimation is limited by the field of view and the collimation strength, both accounted for by the signal to noise ratio. Figure 34b shows the collimation strength in 1D as a function of the distance away from the collimation opening. Figure

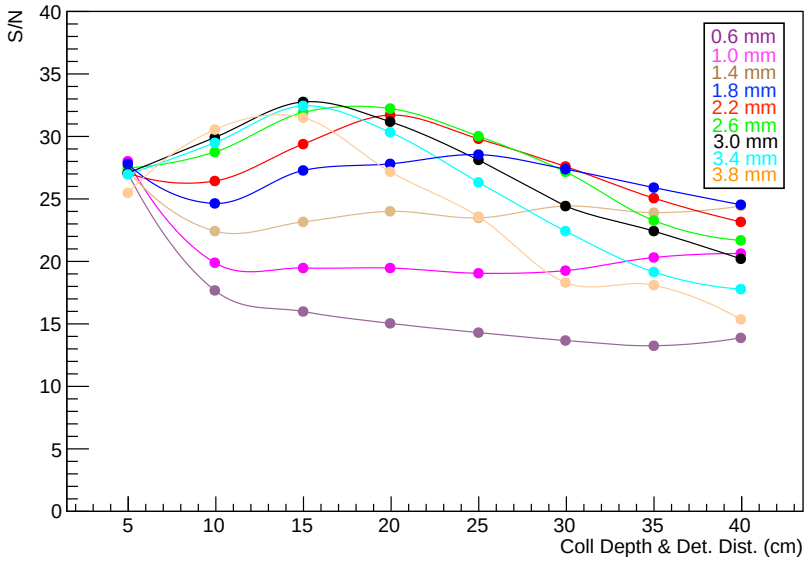

Figure 29: The signal to noise ratio calculated for varying collimation plates geometry resulting from gamma-ray line source. The line source is the width of one crystal.

34a shows the signal to noise in 2D. In 2D, the signal to noise is seen to be fairly uniform along z, but reducing with distance.

From the field-of-view results given, it is not immediately clear how far a patient could be from the collimation for range measurement. However, based on real measurements at 10 cm in front of the collimation (see Section 5.1), it seems reasonable that at 40 cm, which is a bit more than half the signal to noise at 10 cm, the measurement could still be performed to within the specified requirements.

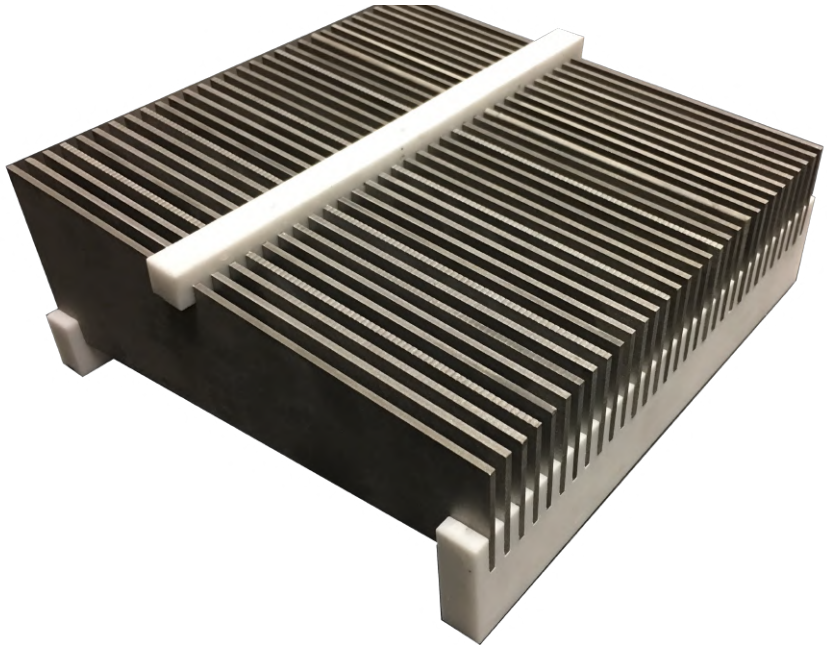

Figure 30: 31 plates of tungsten collimation. The depth is 20 cm, height is 7 cm tapering to about 3.7 cm, and the thickness is 2.2 mm. The tapering was to save on material cost, however it reduces the field of view in ϕ.

4.2 CsI (Tl) Scintillation Crystal

The choice in scintillation material is very important for a few reasons: (1) The gamma-ray cross section increases with density and atomic number, (2) the scintillation decay time limits the acceptance rate of the detector, (3) the scintillation pulse shape can be used to distinguish between particle types, and (4) the cost can vary drastically. For these reasons, the active material for detecting gamma-rays was chosen to be Thallium-doped Cesium Iodide (CsI (Tl)). This material is commonly used thanks to its high light output, low cost, and resiliency to water. CsI (Tl) has also shown to be a good choice for achieving pulse shape discrimination between charged particles.

The scintillation bulk timing characteristics can be modeled as two exponentials

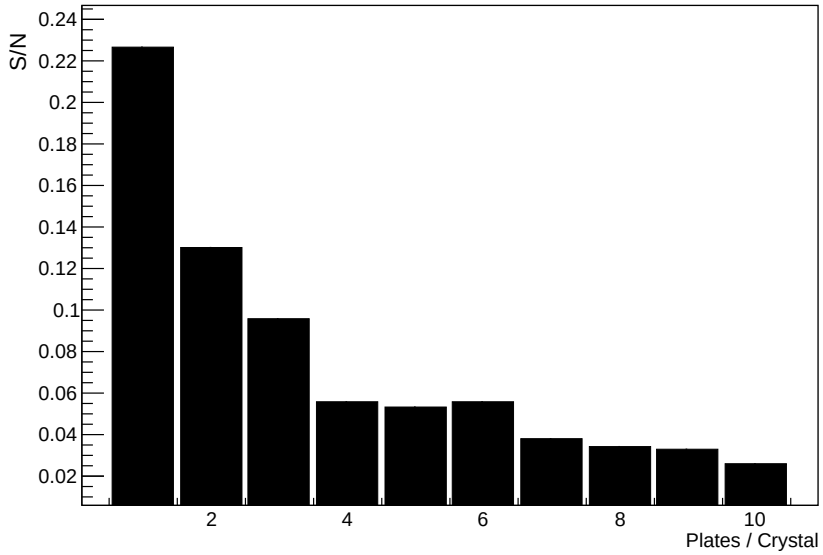

Figure 31: The signal to noise ratio calculated for varying number of plates per crystal.

[25],

$$N = A\ \exp(-t/\tau_f) + B\ \exp(-t/\tau_s)\ , \tag{4.1}$$

where N is the number of scintillation photons, A and B are the amplitudes, τ_f and τ_s are the fast and slow decay constants, and t is the time. By averaging the scintillation signal from 10,000 events, an average scintillation pulse shape was found and is shown in Figure 35. The pulse is normalized by the integral. Fitting to the data to two exponentials, the fast component was found to be approximately 900 ns while the slow component was approximately 4000 ns, agreeing somewhat with the literature [33] having values of 600 ns and 3500 ns. The light yield for gamma-rays and alpha particles is dependent on the Thallium concentration in CsI (Tl). For a photodiode coupled to CsI (Tl), the light yield for photons increases with higher Thallium concentrations until the concentration reaches 200 ppm, where it begins to saturate. The light

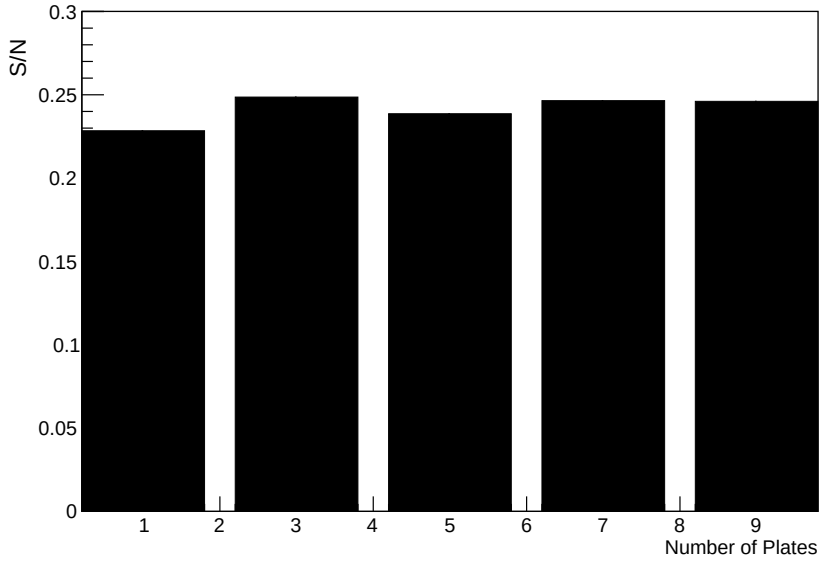

Figure 32: The signal to noise calculated for collimation in both z and ϕ, where the number of plates used to collimate ϕ is varied.

yield for alpha particles increases until the concentration reaches about 3000 ppm. Therefore, using a Thallium concentration above 200 ppm increases the discriminating power of pulse shape analysis, however the overall scintillation response time reduces with increasing Thallium concentration, so the requirements depend on the application [33]. The Thallium concentration quoted by the manufacturers for the scintillators used in this project is 390 ppm, which strikes a good balance between discriminating power and response time.

The intensity for which the detector can safely detect depends on the scintillation timing characteristics. The scintillation light yield maximum, for CsI (Tl), occurs after about 800 ns while the entire waveform lasts around 12 μs.

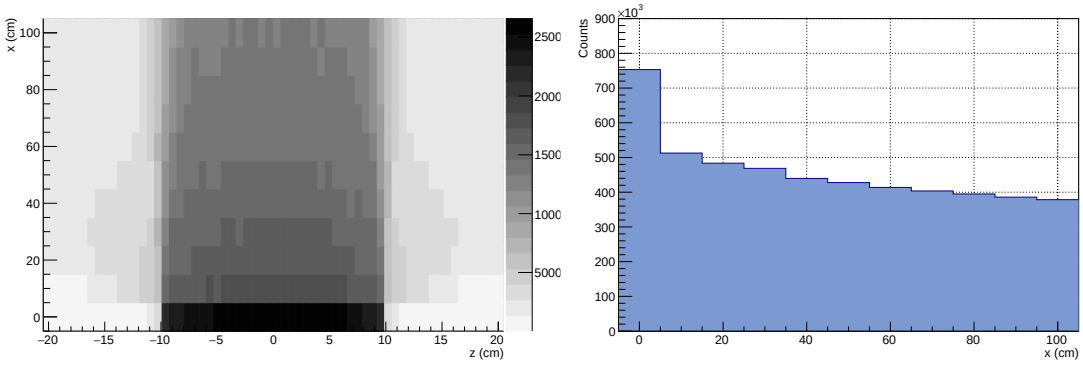

(a) field of view in 2D

(b) field of view in 1D

Figure 33: The field of view as a measure of the probability of a gamma-ray to pass through the collimation. Each bin shade (arb. units) represents the likelihood for a 4.4 MeV gamma-ray to reach the detector if emitted from that location.

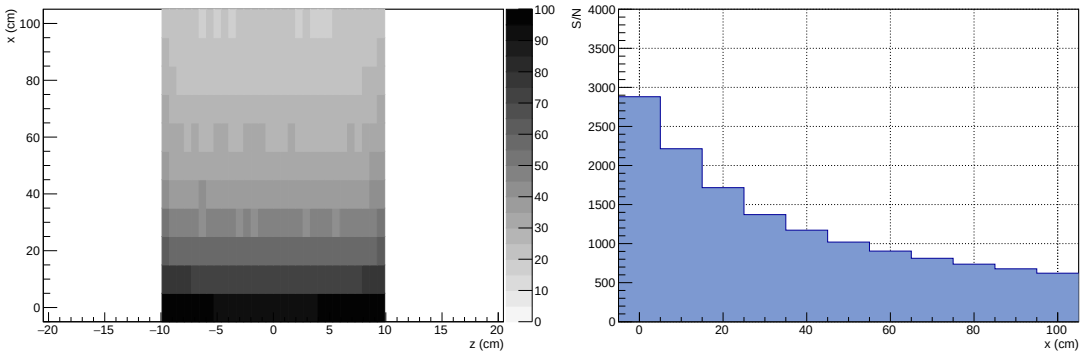

(a) S/N in 2D

(b) S/N in 1D

Figure 34: The signal to noise ratio at each point in the field of view for 4.4 MeV gamma-rays emitted at each point.

4.2.1 Detector Intensity (Rate) Acceptance

The particle intensity at the detector is a choice in this experiment since any distance from the patient can be chosen, however, the higher the rate, the better the signal to noise ratio that can be achieved on a spot by spot basis. Simulations show that a detection rate of around 60 kHz is expected for an 80 MeV proton beam.

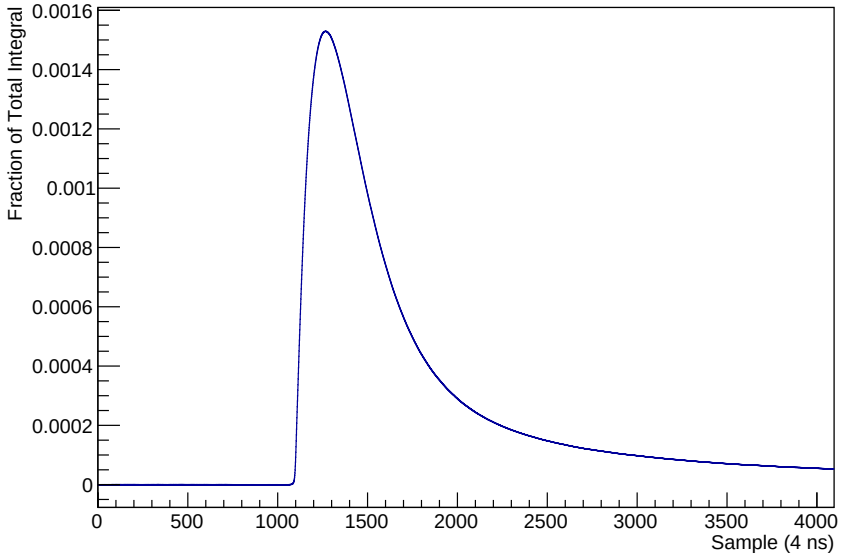

Figure 35: Average scintillation waveform found by averaging 10,000 events, normalized to the total integral. The curve was fit to two exponentials giving decay times of 4000 ns and 900 ns.

Therefore, we are interested in studying the detection rate limitations of the CsI (Tl) crystals. We can put limits on the particle intensity that the detector can accept based on the waveform analysis technique that is required. For example, one scenario might involve summing the entire waveform (about 12 μs). A different scenario might require looking at only the height of the waveform (about 800 ns). Assuming the analysis would require having no waveform-overlap during the chosen time window as caused by an excessive particle rate, we can calculate a rate of overlap occurrence which might be acceptable for the analysis. In other words, what is the rate per scintillation crystal for which we would expect overlap 10% of the time (90% of data is good)? Using Poisson statistics, we can calculate the average number of occurrences over some time period, λ, for which there are 2 or more occurrences 10% of the time,

$$\text{P(2 or more)} = \text{P(0 or more) - P(0) - P(1)} \tag{4.2}$$

$$.1 = 1 - \frac{\lambda^0 e^{-\lambda}}{0!} - \frac{\lambda^1 e^{-\lambda}}{1!} \tag{4.3}$$

Solving, we find that $\lambda = .53$. Finally, we determine an acceptable rate by enforcing .53 occurrences per the time window of which we have interest. For the scenario involving analysis of the entire waveform, the acceptable rate would be $\frac{.53 \text{ pulses}}{12\mu s} = 44$ kHz. So, for any real-time analysis, events must be fully analyzed and processed at a rate of at least 44 kHz per crystal. By either accepting more pileup or by decreasing the time window, a practical rate of acceptance approaches 100 kHz per crystal.

4.2.2 Scintillation Crystal Geometry Optimization

In choosing the optimal crystal dimensions for the detector, we start with the assumption that in the case of simply detecting as many gamma-rays as possible, the optimal size would be infinitely large. In reality, the limiting factor is cost of both crystal material and number of channels. Given a budget for crystals and a price per volume of the material, we can calculate the overall volume of the scintillating material. We constrain the width of the crystals to be 0.5 cm or 0.6 cm, for the purpose of light collection using photodiodes. The cost was set to \$10,000 for 16 crystals at $\$13/cm^3$. A study was conducted to find the optimum depth and height of the crystals given a fixed width and cost per unit volume. In analyzing each dataset, only gammas above 2 MeV were considered.

Method 1: To determine the optimal height and depth, an isotropic point source with an energy spectrum matching the prompt gamma spectrum of a water phantom

bombarded by protons (see Figure 17) is placed in front of a single infinitely large crystal at a distance somewhere between 30 cm and 60 cm. In each run, the energy deposition at every location in the crystal is recorded. In this method, the optimal crystal size is defined as the dimensions which yield the highest $\frac{\text{energy collected by crystal}}{\text{total energy}}$ averaged over an entire run. The volume of the crystal is held constant so that the optimal dimensions can be found for a fixed scintillator cost.

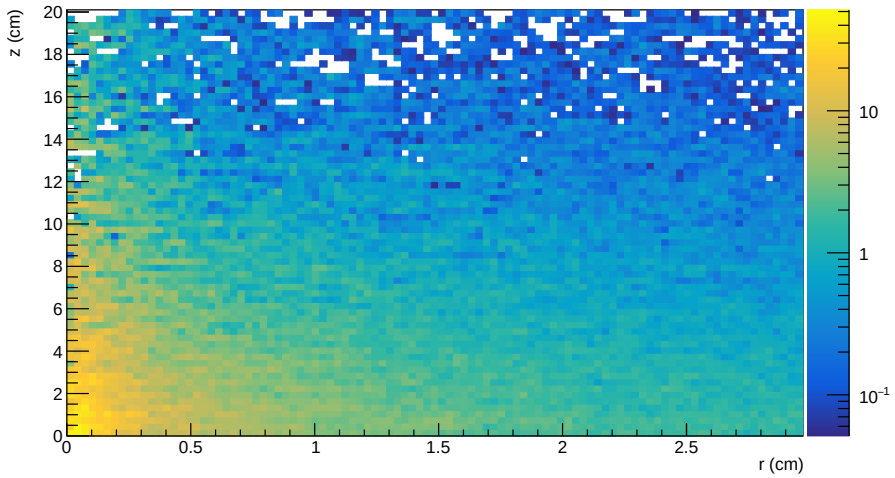

Figure 36: The energy deposition in a large block of CsI (Tl) for a point source simulated in GEANT4. The gamma-rays have the equivalent energy spectrum for protons bombarding a water phantom, but only gamma-rays with energy above 2 MeV are included in the analysis. The crystal size dimensions are varied, but the volume stays the same. The crystal dimensions that contain the most energy deposit are considered the optimal dimensions.

Figure 36 shows the energy deposition in the infinitely large crystal at a distance and depth from the line connecting the crystal face and the isotropic source (10^6 incident gammas). The method for finding the optimal crystal dimensions is to vary

the single crystal size until a maximum amount of energy deposit within the crystal is found. Because the source is isotropic, the incident gamma angles will be smaller on average as the source is moved away from the infinite crystal. Therefore, the procedure was repeated for different distances. The results are shown in Figure 37. The optimal depth appears to be somewhere near 12 cm no matter the distance from the scintillating crystal.

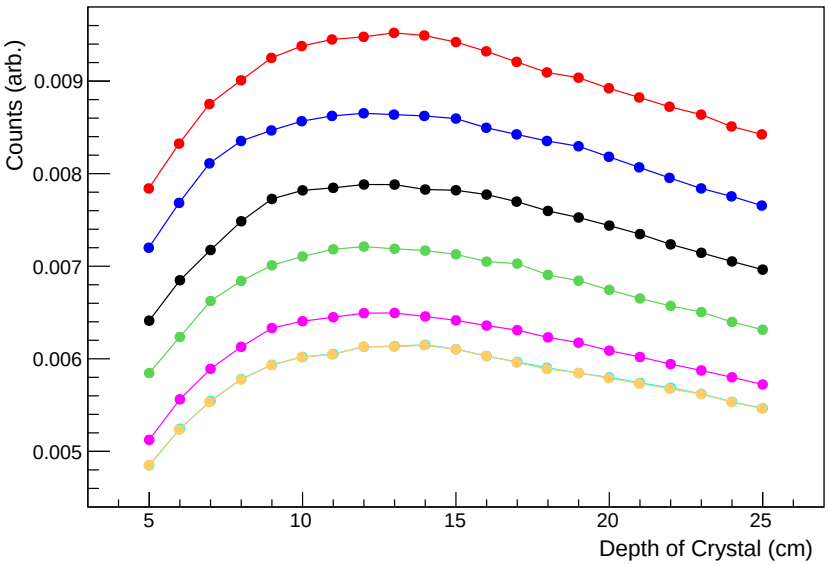

Figure 37: The crystal dimensions were varied for different source distances from the block to see if the incident gamma-ray angles are important. Each curve is for a different distance away from the source. The crystal volume is always constant as the depth and height varies.

Method 2: In this method, a beam of gammas with an energy spectrum matching the prompt gamma spectrum of a water phantom bombarded by protons (see Figure 17) is placed in front of one of three different crystal configurations: (1) a cylinder with a radius = crystal height and depth = crystal depth, (2) a cuboid with height

= crystal height, depth = crystal depth, and an infinite width, (3) a single crystal with 6.6 mm width. A beam is chosen, rather than an isotropic source, so that any dependence on the distance from the source would be eliminated. In the case of the cylindrical crystal and the infinitely wide crystal, the intent was also to eliminate any dependence of the width of the crystal from consideration. We only want to analyze the height and depth of the crystal independent of all other factors. In this scenario, the optimal crystal is defined as the dimensions which yield the largest number of incident gamma interactions with the crystal averaged over each run. Figure 38 shows the number of gamma interactions within the three volumes. The more interactions that occur within the detector per gamma-ray, the more information is available for analysis. Figure 38 shows that for the entire detector volume, having 2 interactions per gamma-ray is likely, but for a single crystal, 1 interaction is more likely. For this reason, an analysis which can combine hits between crystals would be ideal.

Based on these methods of optimization, the actual crystal dimensions were chosen to be 12 cm deep x 7 cm high x 6 mm thick.

4.3 Data Acquisition and Readout

The data acquisition setup for the detector was designed to be able to provide instantaneous feedback to a user or system to facilitate the usefulness of the detector in practice. The data acquisition system incorporates an FPGA which does live processing of a generally large raw dataset into meaningful information that can be used quickly and with minimal further processing.

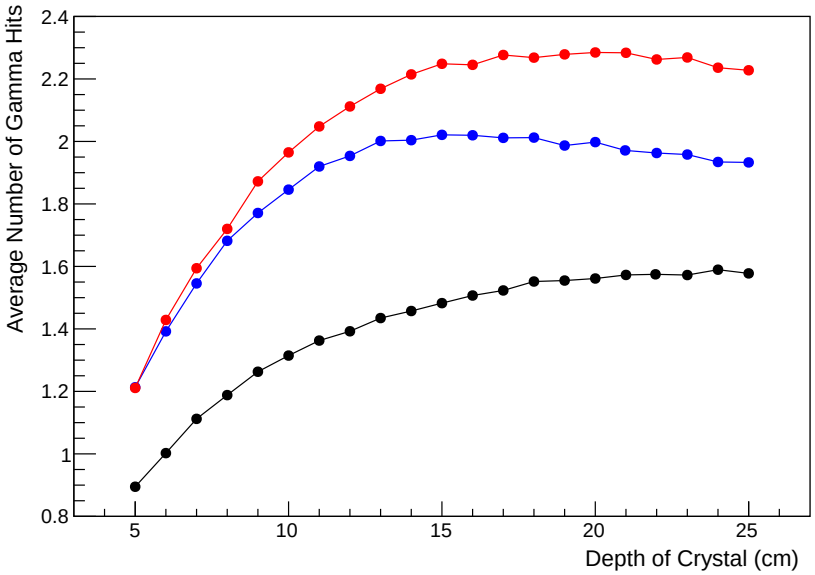

Figure 38: 3 separate crystal geometries were tested in order to eliminate edge effects for a detector with a finite number of crystals. The number of gamma-ray interactions in the entire crystal are plotted (top two curves) along with the number of gamma-ray interactions for a single crystal (lowest curve)

4.3.1 Scintillation Light Readout

A good match for collecting scintillation light produced in CsI (Tl) are multi-pixel photon counters (MPPC), a type of silicon photomultiplier. Figure 39 shows the overlap between the CsI (Tl) light emission intensity and the Hamamatsu S12572-025P MPPC quantum efficiency. The Hamamatsu S12572-025P has an active area of 3 mm x 3 mm, 14,400 pixels, gain up to 5.15 x 10^5, and a capacitance of 320 picofarads. The device is shown in Figure 40. The pixelation in an MPPC is not meant for position sensitivity as each pixel is wired in parallel for a single output. Each pixel is a silicon photomultiplier (SiPM). If any individual SiPM pixel is hit (fired), the output for that pixel is designed to saturate, so that if one fired pixel gives an output of 10^5 electrons,

10 fired pixels would give 10×10^5 electrons. The fact that each pixel saturates allows for a uniform response across the area of the MPPC resulting in low noise overall. The concept is similar to a geiger counter. The photons are counted by counting the number of fired pixels, where each fired pixel corresponds to one photon. Each pixel takes approximately 20 ns to recover after firing, so by using a very fine pixelation, the possibility of under-counting the number of incident photons due to pixels recovering is minimized. Hamamatsu offers differing degrees of pixelation depending on the application.

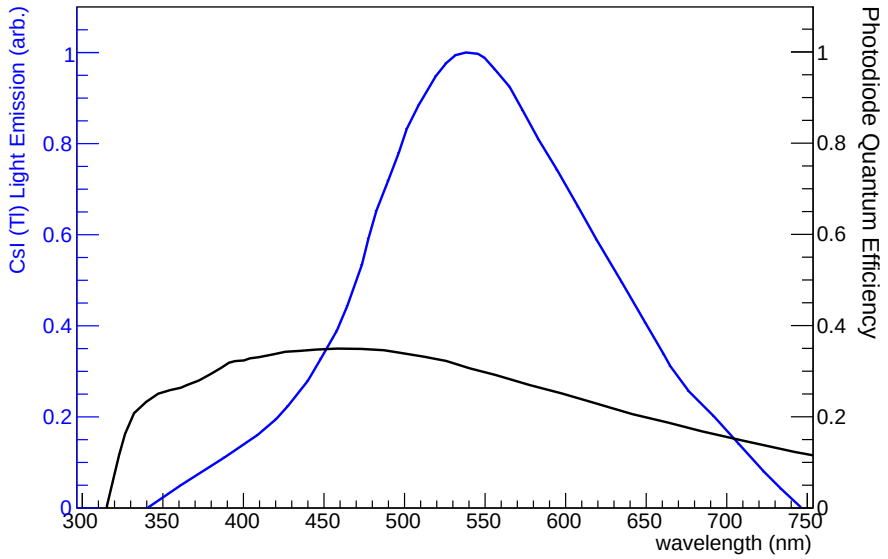

Figure 39: The CsI (Tl) light emission (blue) and the MPPC quantum efficiency (black). The overlap between the two curves shows a good match.

Collecting light from each scintillating crystal requires an optical system. In this application, the concern is in maximizing the light collection for a given event. Each crystal is wrapped with 3 layers of teflon, a diffuse scatterer of light, to prevent light

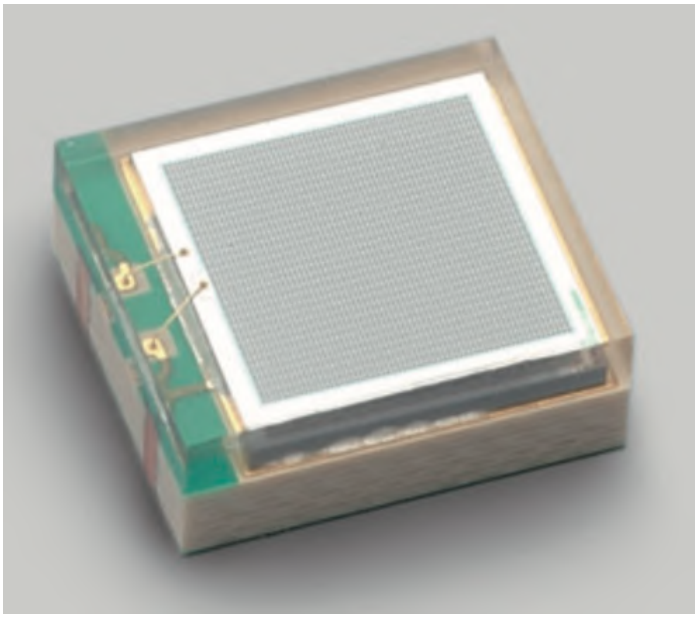

Figure 40: Hamamatsu S12572-025P MPPC.

leakage. The MPPCs are coupled on two sides of the crystal as shown in a 2-crystal prototype detector which was constructed to aid in the development process, Figure 41. To aid in scintillation light transmission between the MPPCs and the scintillator, an optical couplant gel was used, Nye OC-431A-LVP. The optical couplant blocks light below 400 nm, but has nearly no effect on light in the remaining wavelengths of interest (up to 800 nm).

To determine a suitable pixelation of the MPPCs for the detector, the probability of 2 or more photons hitting a pixel within the recovery time of a fired pixel is calculated. The first step is to approximate the number of photons expected to reach the MPPC within the recovery time. The desired dynamic range of the detector is to measure gamma-rays up to 10 MeV. The light emission for CsI (Tl) is 54,000 photons per MeV of energy deposit, so for a 10 MeV gamma-ray depositing all of its energy into a single crystal, we would expect about 540,000 photons to be generated. The light is not

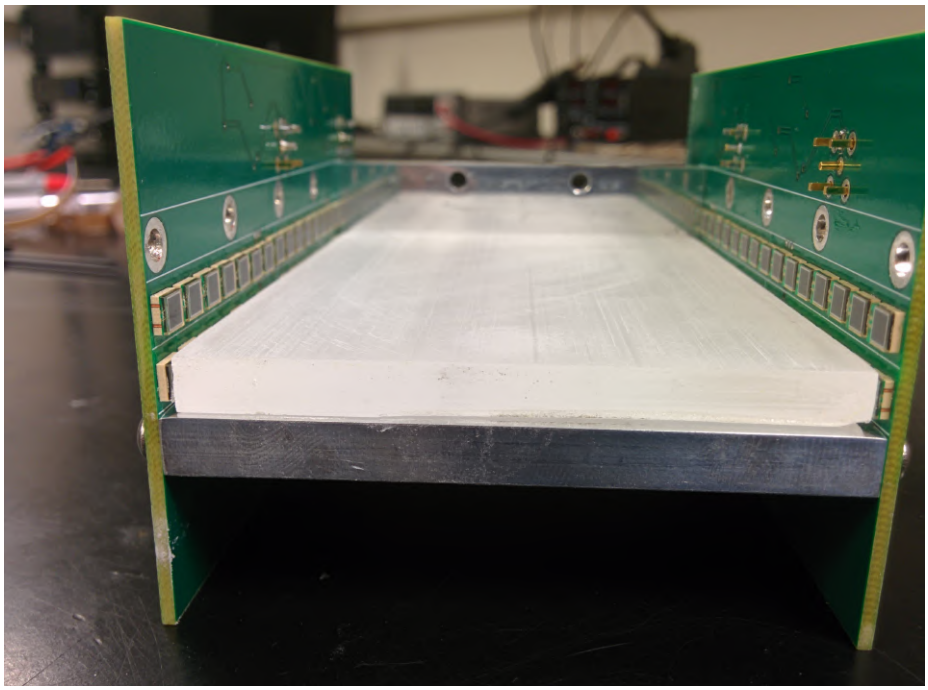

Figure 41: An early prototype detector which used 2x CsI (Tl) crystals. The CsI (Tl) crystal is normally wrapped in Teflon, however, this image demonstrates the coupling to the MPPCs.

generated instantaneously for CsI (Tl) as discussed in Section 4.2. The scintillation light is emitted following the pulse shape shown in Figure 35, which gives at its peak about 0.15% of the total light emission. Over a 20 ns period, the total percentage of the signal is about 0.75%. So, of the 540,000 photons that are generated over the lifetime of a 10 MeV gamma-ray scintillation pulse, the maximum emission rate is about 0.75% of 540,000 photons over a 20 ns period. The MPPC area is 3 mm x 3 mm and the area of the crystals which is being read out is 2 sides x 6 mm x 120 mm. A typical fraction of the light that reaches the MPPC is $\frac{\text{3 mm x 3 mm}}{\text{2 x 6 mm x 120 mm}} = 0.625$ %, but we would like to calculate the upper limit, so we will assume that the event happens nearby the MPPC and the MPPC receives the entire fraction of light. We also assume there is no absorption in the crystal or light leakage. Now the amount of

electron-hole pairs actually generated in the photoelectric conversion is a function of the quantum efficiency, which we generously set to 30% over the whole wavelength spectrum. So an upper limit on the total amount of pixels fired during 20 ns for a 10 MeV gamma-ray in a single MPPC is approximately 0.75% x 30% x 540000 = 1200 fired pixels. There are 3 choices of pixelation density for the Hamamatsu S12572 MPPC family, either 900 pixels, 3600 pixels, or 14,400 pixels. The average number of photons per pixel respectively are 1.33, 0.33, and 0.083. The upper limit on the probability for each pixel to have 2 or more photons within the 20 ns peak scintillation for a 10 MeV gamma-ray is about 38%, 4%, and 0.3% respectively. To avoid any amount of saturation due to the recovery time of the pixels in the MPPC, the 14,400 pixel MPPC was chosen. Since this light collection approximation is an upper limit, the 3600 pixel MPPC is a good choice as well.

4.3.2 Preamplification

The MPPCs are wired in parallel in groups of 8, so input capacitance for the preamp is 8 x 320 pF = 2560 pF, which is quite large. Topologically, the MPPC preamplifier shown in Figure 42 is a charge integrator. The voltage output is approximately, $V_{out} = Q_{det}/C_f$, where Q_{det} is the charge deposited into the detector and C_f is the feedback capacitor. The feedback capacitance was chosen through experimentation to be $C_f = 22$ pF. The preamp gain was measured for a similar input capacitance as the expected input capacitance for the MPPCs. For a 3200 pF input capacitance driven by a 10 mVpp sine wave, the gain was measured and plotted in Figure 43. The theoretical gain is approximately $\frac{V_{out}}{V_{in}} = \frac{Q_{det}}{C_f V_{in}} = \frac{C_{in}}{C_f} = 145$. Because of 50 Ω termination of both the preamp and the oscilloscope input (forming a voltage divider),

the measured voltage is half of the amplifier output. Taking the 50 Ω termination into account, the calculated gain matches well with the measured gain since they are different by about a factor of 2.

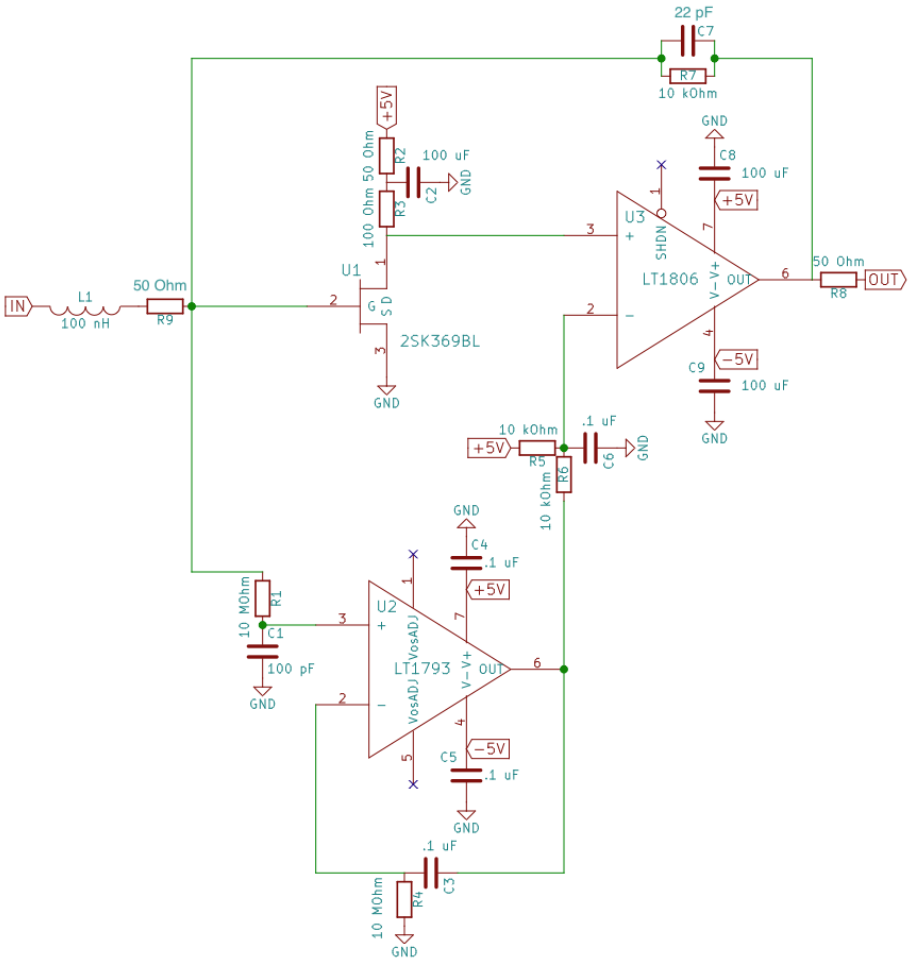

Figure 42: A large bandwidth, high gain, low noise circuit design for amplifying the MPPC signals.

The remainder of the preamp circuit consists of a servo and a JFET input buffer. The LT1793 opamp acts as a servo, which is a mechanism that senses an offset at the output and drives the input until the output goes to zero. The JFET input buffer

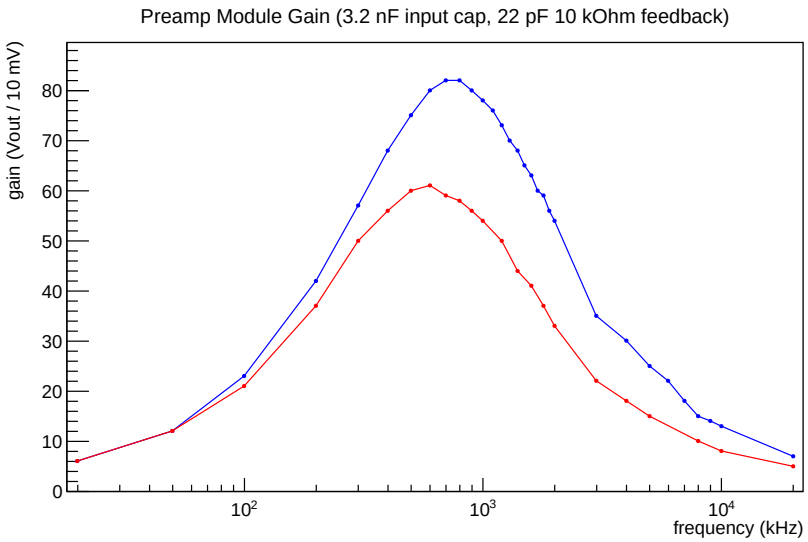

Figure 43: The gain of the preamp module measured by driving a 3200 pF capacitor with a 10 mVpp sine wave and measuring the output voltage.

has a very high impedance, which has the effect of eliminating input current noise and also minimizing any input offset error. The integrator opamp, LT1806, has a low voltage noise current density, 3.5 nV/$\sqrt{\text{Hz}}$ and a high gain bandwidth product of 325 MHz. The output voltage noise has been measured to between 1 mV - 2 mV. The bandwidth of the preamplifier is about 2 MHz shown in Figure 43. The circuit layout was designed using a pcb layout software called KiCad. 40 assembled preamps were produced by Sierra Circuits. To allow flexibility in the readout of the detector, the preamps were made to be modular. The resulting preamp is shown in Figure 44.

4.3.3 FPGA Processing and Data Reduction

The preamplifiers outputs are fed through two cables to the National Instruments data acquisition (DAQ) system, the NI 5752R. The analog to digital converter (ADC)

Figure 44: MPPC Preamp Module, designed to plug into headers on the readout board.

is the Texas Instruments AFE5801. The data from the ADC is processed by the Xilinx Kintex-7 field programmable gate array (FPGA) followed by data transfer via PCIe to the computer for storage.

The FPGA hardware implementation is a major feature of the data acquisition system. The main duty of the FPGA is to process waveforms into hit packets as a means of reducing the data. Without data reduction, entire waveforms would need to be stored. For a 12-bit digitizer, an entire waveform of 300 samples would be 12 bit $*$ $300 = 3600$ bits.

For a single event, four waveforms are produced at each crystal (4 channels of digitization). Rather than storing the entire waveform of each, the waveforms are

processed into "hit packets" of size 224 bits as seen in Table 2. This gives a reduction in data factor of $4 * 3600$ bits / 224 bits = 64.3. Therefore, in theory, by this means of data reduction, the DAQ can handle particle rates 64 times higher than without data reduction. The information stored about each pulse relates to the total energy deposit, the pulse shape, the location of the hit within the crystal, and the time as seen in 2.

Quantity	Size (bits)
time	64
ch0_Sum	32
ch1_Sum	32
ch2_Sum	32
slow_Sum	32
total_Sum	32
Hit Packet	224

Table 2: The contents of a hit packet as processed by the FPGA firmware.

To get an idea of the amount of available bandwidth per crystal per waveform, the data transfer rate (PCIe single lane, single link) is 250 MB/s, but in practice $D = 215$ MB/s. For a particle rate of $\nu = 500$ kHz, for $N = 16$ total crystals, the data available per crystal per event is $\frac{D}{\nu N} = 225$ bits. For an entire waveform, the maximum accepted data rate is 31 kHz if only storing one waveform, or if storing 4 for each crystal, 7.8 kHz.

4.3.4 Triggering on Correlation

Triggering of the DAQ system uses no synchronization signal from the beam. The triggering system is completely self-triggering. Each scintillation crystal has 4 channels of readout. When a gamma-ray interaction occurs within the crystal, a trigger is

generated when at least two of the channels become correlated for more than 150 consecutive samples. The correlation coefficient is defined as the following:

$$r = \frac{cov(X,Y)}{\sigma_X \sigma_Y} = \frac{N\Sigma x_i y_i - \Sigma x_i \Sigma y_i}{\sqrt{[N\Sigma x_i^2 - (\Sigma x_i)^2]}\sqrt{[N\Sigma y_i^2 - (\Sigma y_i)^2]}} \ ,$$

where x and y are data sets which are being checked for correlation. The correlation coefficient ranges between -1 and 1 with 1 being perfectly correlated and -1 being anticorrelated, 0 is no correlation.

Division is often a very complicated process in terms of FPGA processing. Many LUTs (look up table, a unit of logic in an FPGA) can be used up in division processing. Instead, we can manipulate the equation to achieve the same results, using multiplication only (which can be computed efficiently in some cases) [10]. The condition for triggering computed by the FPGA is then

$$r > \frac{cov(X,Y)}{\sigma_X \sigma_Y} \quad \rightarrow \quad r * (\sigma_X \sigma_Y) > cov(X,Y) \ , \tag{4.4}$$

where r can be set as the minimum correlation coefficient for a trigger. In order to calculate the correlation coefficient on an FPGA, 5 sums need to be tracked, Σx_i, Σy_i, $\Sigma x_i y_i$, Σx_i^2, Σy_i^2.

As each new sample comes in from the ADC, it is pushed into each of the above sums. Also, in order to keep the sum from diverging, the oldest value which was added is removed. So, if 200 samples are being considered for correlation, a 200 sample length FIFO (first in, first out) can be used to access the most recent sample and the oldest sample for iterating on the sums. A sample screen shot of the logic layout in lab view is shown in Figure 45. The logic block takes two inputs, x and y, and outputs the covariance and variance of the most recent 200 samples, allowing for a check on the condition shown in Equation (4.4). The end result is the ability to calculate the correlation coefficient over the last 200 samples for each sample.

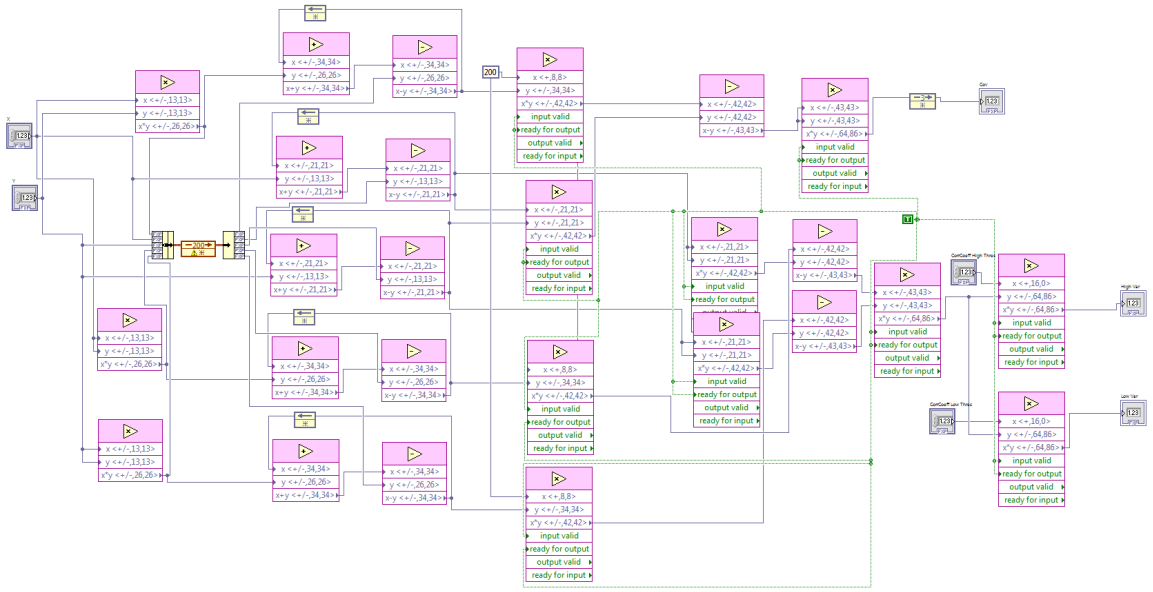

Figure 45: The graphical representation of the correlation coefficient calculation as drawn in LabVIEW.

The correlation trigger has a minimal sensitivity to noise since noise between independent signals is uncorrelated. An example detector measurement and the corresponding correlation coefficient plotted versus time are shown in Figure 46, which shows 4 channels of readout from the same CsI (Tl) crystal. For a particle interaction in a scintillating crystal, each channel should be correlated since each is reading out the same crystal. In Figure 46, the signal in each channel is indistinguishable from the noise, however, the correlation calculation shown at the bottom of Figure 46 shows a clear correlation between the channels implying that a real interaction occurred. This can in principle allow for measuring tiny energy deposits in the crystal, which is helpful for clustering of the multiple crystals for an event.

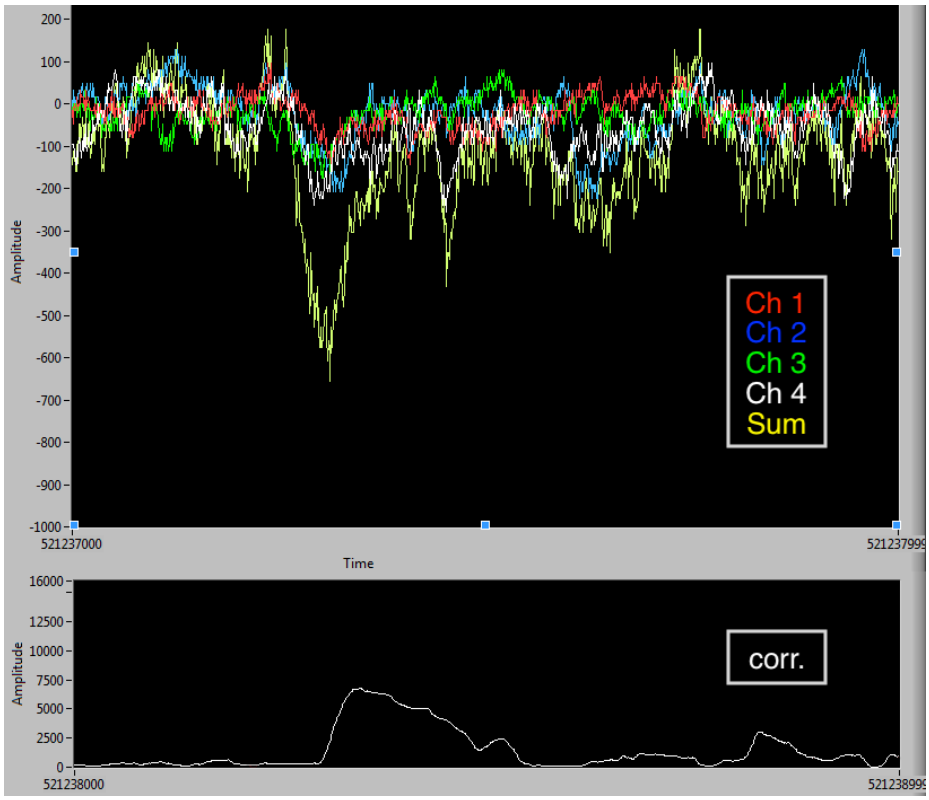

Figure 46: The readout of a single scintillating crystal by 4 channels. This is an example of a small signal where each channel is nearly imperceptible as a signal, the sum is barely above the peak noise, but the correlation coefficient clearly identifies this as a real pulse.

4.3.5 Streaming Pedestal Subtraction

An important aspect of analyzing pulses from the detector is to subtract the intrinsic offset associated with each detector channel. The offset is usually the result of an electronics offset introduced by the amplifier. In poor conditions, the offset could also be the result of a leakage current or dark current. Subtracting the offset or pedestal is important for a quality analysis of the pulses, especially for measuring the energy deposit of a particle. A unique pedestal calculation procedure is outlined in this section. The procedure is equivalent to filling a histogram of the ADC value and

keeping track of the most common value over a window of 15000 (threshold) clock cycles. The assumption is that the most common value is the pedestal.

The procedure is as follows. A counter array has 256 values. Each element of the array has a unique address. Each channel ADC fills two FIFOs every 3rd clock cycle (clock = 50 MHz). The ADC values streaming through the FIFOs are used to point at corresponding array values. So, if the ADC value were 125, the address 125 of the array would be selected to be modified. The value stored at the address picked by the ADC is checked against the largest value stored in the array. If it is greater than the highest value, then the ADC value is stored as the new highest value in a register. If the value is less than the highest value, the register value is unchanged. In either case, the value of the array is incremented by 1 until the total number of values in the array reaches a threshold of 15,000. Once over threshold, a mechanism for decrementing values begins. One FIFO continually accepts new ADC values which are immediately used to increment the array. A different FIFO, which was filled with the same values as the other, but is not emptied until the number of entries is overthreshold the of 15,000, begins decrementing the array. New ADC values are only being introduced into each FIFO on every 4th clock cycle allowing the decrementing to occur more frequently than the incrementing when over threshold. In this way, the total integral of the array stays approximately equal to the threshold value. As the ADC values are streaming, the calculated pedestal is subtracted from the ADC on every clock cycle.

For a pedestal that varies with time, the response time of the algorithm depends on the ADC value distribution, $P(x)$, the total integral of the histogram, and the sample rate. The time taken for a new pedestal to emerge would be approximately equal to $\frac{1}{2\ (\text{sample rate})} \int_{-\Delta x}^{\Delta x} P(x)\, dx$, where the pedestal is bounded by $\pm\Delta x$. The Pedestal FIFO acquires values 4 times slower than it outputs values. Therefore, once the subtraction

mechanism turns on, the total integral of the histogram should be approximately equal to the threshold value. The acquisition rate is $\frac{50 \text{ MHz}}{4} = 12.5$ MHz. Currently, the threshold is 15000. The limit on the pedestal change time (taking the pedestal width to infinity) would be approximately $\frac{15000}{2\,(12.5 \text{ MHz})} = 0.6$ ms, giving a rate of about 1,667 kHz or a response time of about 600 microseconds.

4.4 Methods For Reducing the Neutron Background

As the patient is irradiated by protons, the resulting gamma-ray signal at the detector is well correlated to the Bragg Peak. The major background to that signal is due to neutrons. During a typical treatment, there can be many sources of neutrons including the patient, the beam nozzle, or along the beam-line upstream of the treatment room. The neutron flux at the detector will vary depending on the treatment environment, but will generally be higher than the gamma-ray signal since the neutrons do not react strongly to the collimation as further demonstrated by Figure 47. This effect is counteracted a bit since the total cross section for neutrons interacting with CsI (Tl) is not as high as gamma-rays as shown in Figure 22, found with EXFOR data [30]. Three methods for reducing the neutron background, time of flight, pulse shape discrimination, and shielding will be presented in this paper.

4.4.1 Time of Flight (TOF)

Time of flight is a method which can reduce the neutron background if the timing of the protons from the beam is well known. The idea is to accept signal at the detector when the prompt gamma-rays are arriving and reject the detector signal

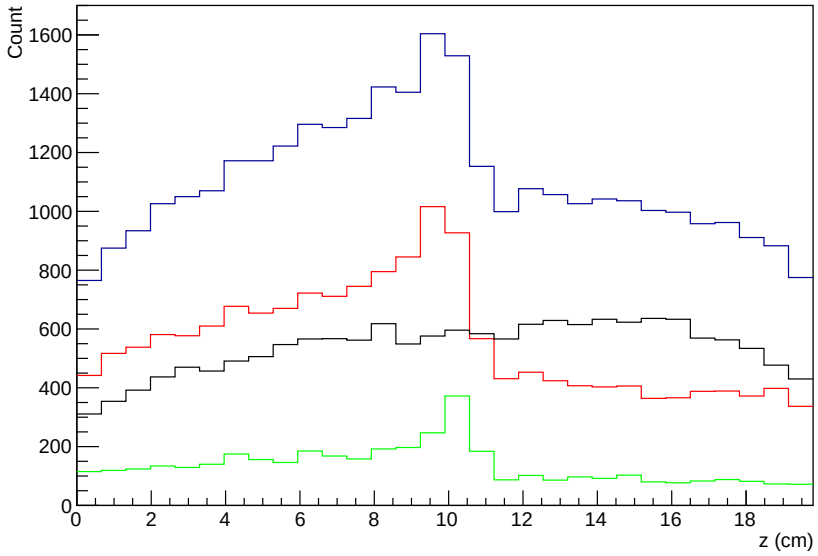

Figure 47: The range detector signal separated by incident particle type simulated in GEANT4. Blue is the total signal, red is from gamma-rays, black is from neutrons, and green is from the 4.4 MeV gamma-ray.

at all other times. Because the neutrons which are produced in the patient during treatment move slower than the prompt gamma-rays, they arrive at the detector spread out in time, becoming a constant background, whereas a prompt gamma-ray will always have an identical time of flight independent of energy. A proton therapy simulation was run to understand the timing of the gamma-rays and neutrons emitted from the patient. For a perfectly bunched proton beam, Figure 48a shows how the prompt gamma-rays arrive tightly bunched, clearly separated from the later arriving neutrons. In a real beam, there are some important differences depending on the beam accelerator, predominantly either a synchrotron or cyclotron. The RF for a typical proton therapy cyclotron is usually an order of magnitude higher than synchrotrons, such as the IBA C230 isochronous cyclotron, which has an RF of 106 MHz [37]. The process of slow extraction and the low Q cavity as used in the PROBEAT system

makes the duty cycle very large, nearly continuous. The revolution frequency for the PROBEAT synchrotron is between 6 MHz to 10 MHz, which leads to proton bunching of between 100 ns and 160 ns. Adding to the simulation a 100 ns bunching of the proton beam leads to a mixing of the gamma-rays and neutrons in time, no longer allowing for discrimination as shown in Figure 48b. For a cyclotron producing 230 MeV protons, the period is about 3 ns (see Section 2.3). According to Biegun et al. [8], in order to use time of flight as a means of background reduction in prompt gamma-ray range measurements, the proton bunches need to have a duration of no more than about 5 nanoseconds. Most cyclotron accelerators for clinical use meet this requirement, while the synchrotrons do not. See reference [37] for a detailed study of using TOF to reduce the neutron background for a cyclotron accelerator. Due to the primary focus being to measure the range at the Mayo Clinic facility in Arizona, using time of flight to reduce the neutron background is not possible.

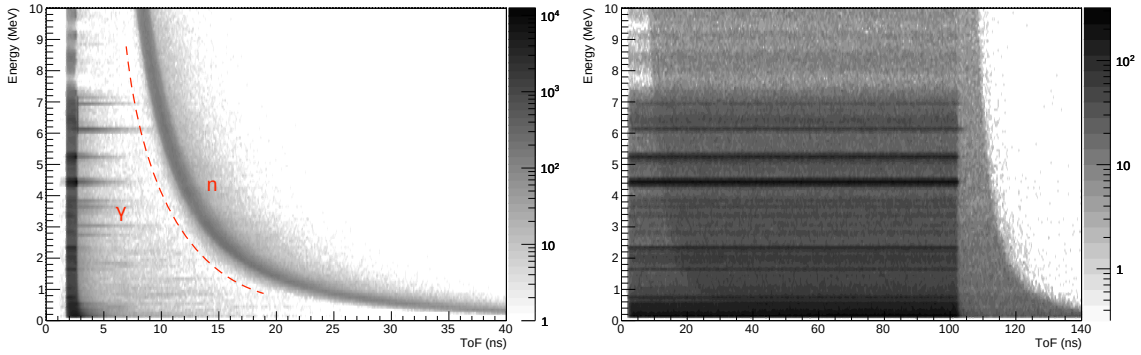

(a) perfectly bunched proton beam

(b) 100 ns proton bunch

Figure 48: For protons that are perfectly bunched, i.e. all having identical t_0, the time of flight for all detected secondary radiation is plotted on the left. For perfect bunching of the proton beam, the neutrons and gamma-rays can be separated using time of flight. For protons that have a 100 ns bunch, the gamma-rays and neutrons are no longer distinguishable from each other, as can be seen on the right.

4.4.2 Pulse Shape Discrimination

Scintillators are known to respond differently to different incident particle-types due to the intrinsic LET differences between particle types. By doing waveform analysis, neutron interactions which result in a secondary charged particle can be identified. The most common method for using pulse shapes of detector signals to discriminate between particle types is to simply integrate over different parts of the waveform, most commonly the beginning of the waveform (fast) and the end of the waveform (slow), and then to plot the fast versus the slow. Figure 49 defines the fast and slow parts of a pulse for a single CsI (Tl) crystal detector averaged over 10,000 events. A Fast Vs. Slow plot is made by plotting a point for each waveform: $(x, y) = (\int_{slow}, \int_{fast})$.

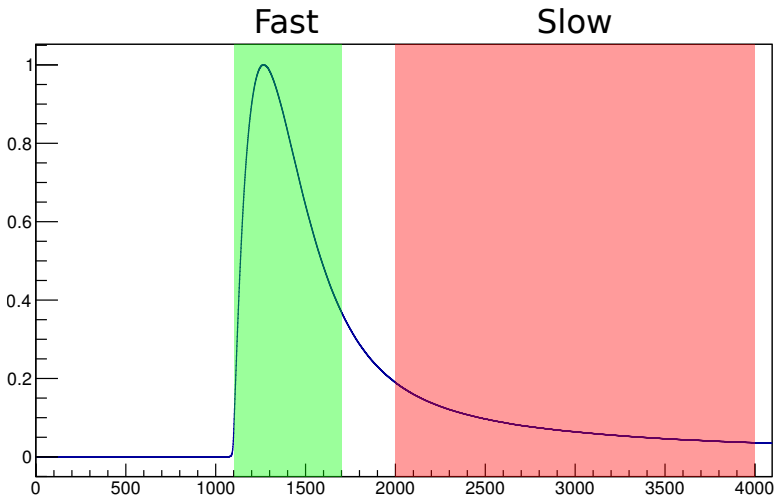

Figure 49: Average scintillation pulse found by averaging 10,000 events. The fast part is defined by the green range, while the slow part is defined by the red range.

A two-crystal detector was used to study the pulse shape discrimination capabilities

of CsI (Tl). Two radioactive sources were used for comparison, one being a sealed Cobalt-60 source, which emits gamma-rays through β^- decay and the other a sealed AmBe source, which emits gamma-rays through alpha decay and neutrons through alpha spallation on Beryllium. The Fast Vs. Slow plot for Cobalt-60 is shown in Figure 50. See Figure 51 for a Fast Vs. Slow plot for an Americium-241(Be) radioactive source, which emits both neutrons and gamma-rays. Notice that for the Cobalt-60 source, only one line is visible, while with the Americium-241(Be) source, there are three lines visible. The common line between both plots is a result of gamma-ray interactions with the crystal. Other features shown in the Figure 51 are still being studied, but the current hypothesis are given in the caption. What can be said of the two uncommon lines is that they must be a result of neutrons, however, it cannot be said that all the incident neutrons are contained in these lines. More commonly, neutrons can also excite nuclei through inelastic collisions in the crystals, which results in an emitted gamma-ray that is then detected. Most likely, most of the neutrons which interact with the scintillators result in a gamma-ray. Nonetheless, pulse shape discrimination should provide some reduction of the neutron background and can also be used to eliminate other sources of background such as pileup or direct proton hits from the proton beam.

4.4.3 Shielding

Carefully chosen shielding may be able to reduce the neutron fluence while retaining the fluence from prompt gamma-rays generated by protons. A hypothesis is that by introducing a low-Z moderating material between the collimation plates, the gamma-

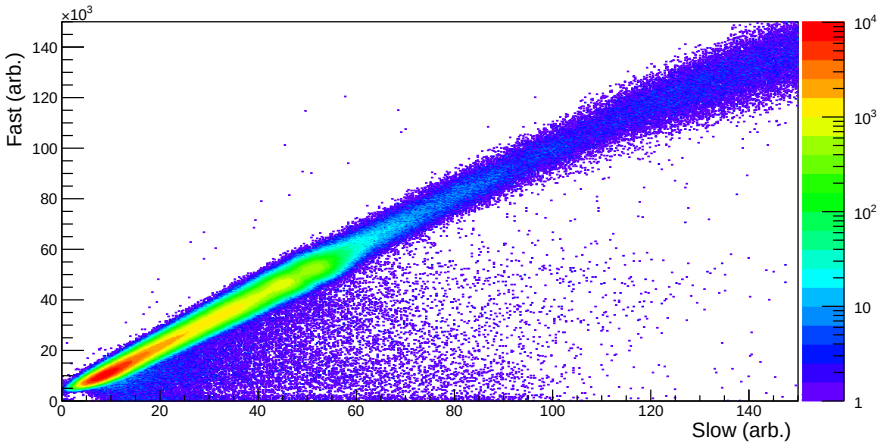

Figure 50: Prototype Detector Measurements: A Fast vs. Slow plot for a low intensity Cobalt-60 source, where only one line is present.

rays will pass more easily than the neutrons. Once the neutrons are moderated down to thermal energies, they will capture onto a nucleus, a process that typically produces a gamma-ray. Because we do not want to introduce additional gamma-rays into the measurement, the moderator is loaded with Lithium-6, which has a high thermal neutron capture cross section (900 barns) and does not emit a gamma-ray in the neutron capture reaction. The shielding has not been studied extensively to this point, however future work will test the viability of shielding the neutrons.

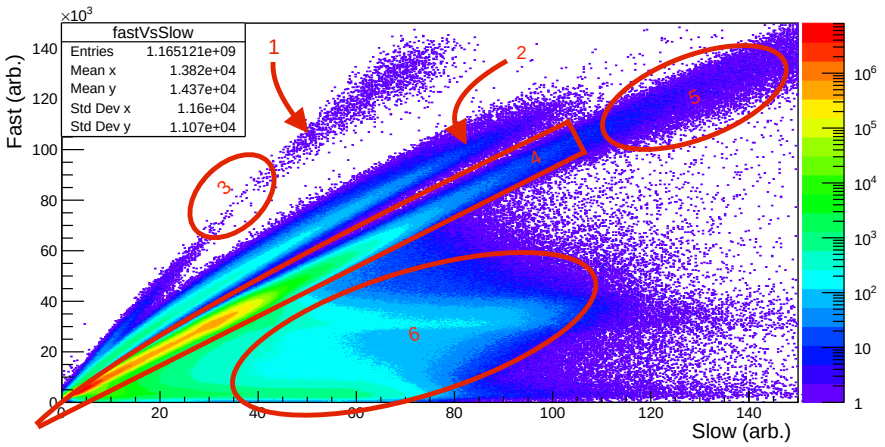

Figure 51: Prototype Detector Measurements: (1) A curved line (possibly alphas) produced through neutron interactions in the CsI (Tl). (2) A curved line (possibly protons) produced through neutron interactions in the CsI (Tl). (3) A gap in the line, currently of unknown origin. (4) A straight line, caused by electrons produced through Compton scattering, photoelectric absorption, pair production. (5) The point where saturation in the SiPM preamplifier is starting to occur. (6) Pileup: Events where 2 or more waveforms appear in the same time window.

Chapter 5

RANGE VERIFICATION DETECTOR RESULTS

Based on the development process described in Chapter 4, a 16-crystal collimated prompt gamma-ray detector was constructed and tested at the Mayo Clinic Proton Therapy Center in Phoenix, Arizona. The measurement involved shooting 6 beam energies through isocenter into an acrylic phantom and measuring the range and the statistical uncertainty in the range. The goal is to measure the range to about 1 mm within 100 ms of beam time for a 1 nA beam current. This chapter will describe the detector and its operation, the experimental setup, and the measurement results. This work was funded by The Kemper Marley Foundation through the Mayo Clinic.

5.1 Detector (16 Crystals, version 3)

The range detector is shown in Figure 52. The design is quite compact, which is seen as an important factor for integrating the range detector into clinical use. The detector assembly process is somewhat complex as it involves three separate systems, temperature control, electrical readout, and optical readout.

Images highlighting the different assembly steps are shown in Figure 53. An overview of the detector assembly process is as follows:

1. Solder all the readout electrical devices onto the pcb.
2. Build a cooling block module (temperature control).

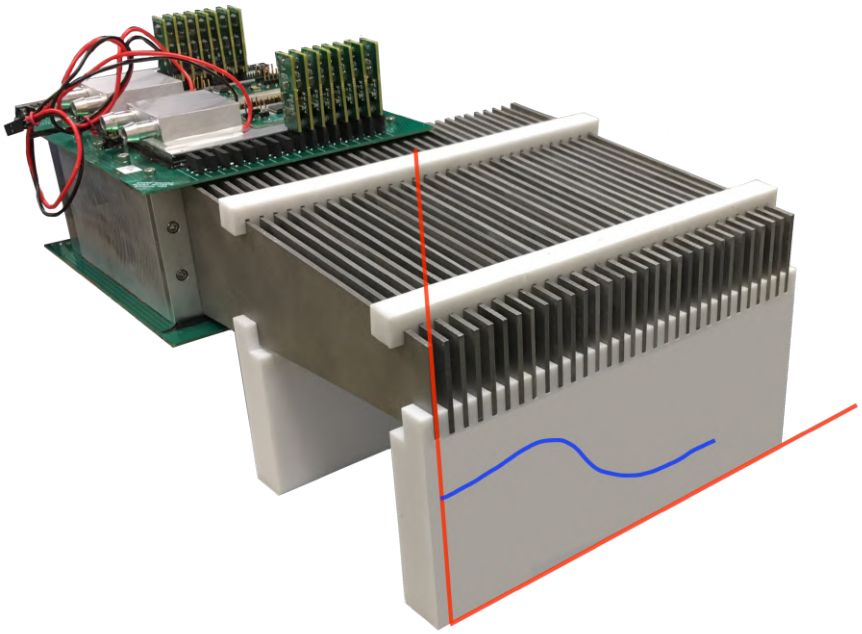

Figure 52: A prototype 16-crystal CsI (Tl) prompt gamma-ray range detector. The plot overlaid on the front of the detector demonstrates the gamma-ray signal corresponding with the proton range.

3. Epoxy cooling block modules to the readout boards using a thermal epoxy and seal aluminum/pcb boundaries with black silicone.
4. Bolt the bottom readout board to the open enclosure with liquid gasket between the board and aluminum.
5. Attach the enclosure to the xyz table.
6. Put optical couplant on each MPPC using a syringe.
7. Wrap and place each crystal into the enclosure (3 layers of teflon).
8. Attach aluminum window.
9. Put optical couplant on the remaining readout board.
10. Carefully bolt readout board with liquid gasket to the enclosure.
11. Seal each aluminum/pcb and aluminum/aluminum boundary with black silicone.

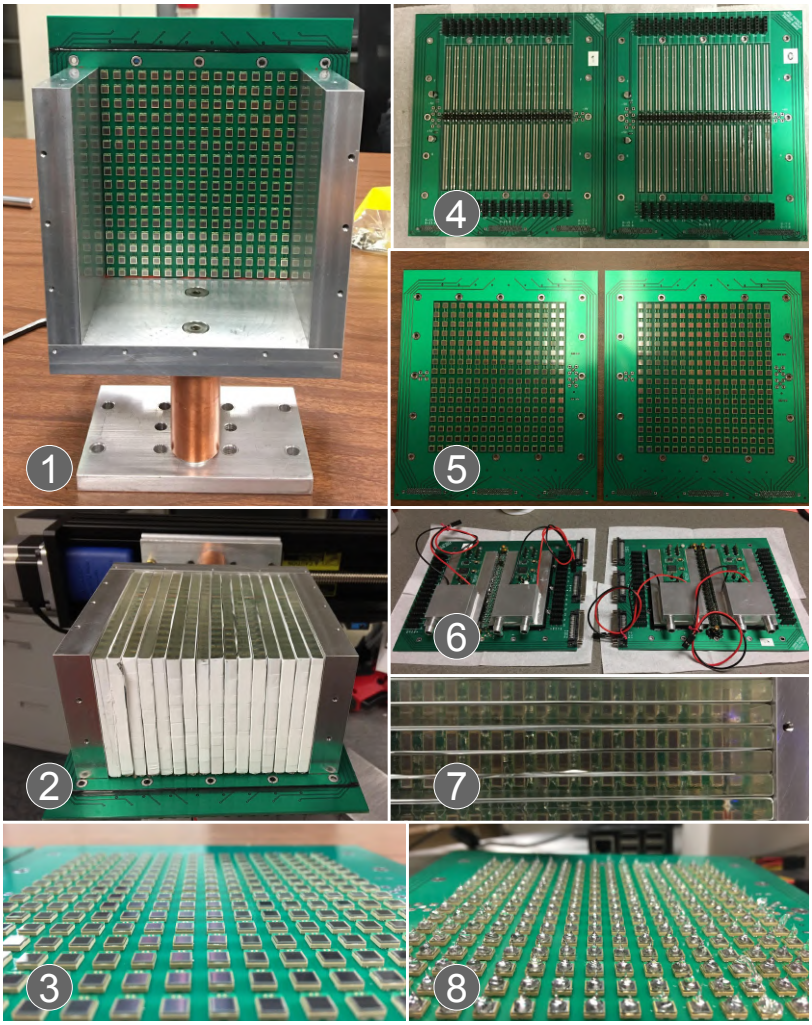

Figure 53: (1) The aluminum enclosure mounted to a readout board (MPPCs are visible). (2) CsI (Tl) scintillation crystals wrapped in Teflon and placed into enclosure. (3) A close-up of the MPPCs soldered to the readout board. (4) A top view of the readout boards before the temperature control cooling boards have been attached. (5) Bottom view of the readout boards. (6) The readout boards fully assembled with the cooling blocks. (7) A view into the scintillation crystals highlighting the transparency of the optical system. (8) The MPPCs with optical couplant, before coupling to the crystals.

5.2 Temperature Control

Temperature control is important for any silicon based detection system since the dark current and diode characteristics are highly temperature dependent. To ensure a stable response from one measurement to another, a temperature control system was designed and incorporated into the detection system. The circuit includes a temperature sensor and a thermo-electric cooler which is pulse width modulated to drive the temperature to the set point. The temperature sensor and the thermo-electric cooler MOSFET are connected to a Raspberry Pi, which controls the temperature using a highly dampened tuning algorithm. The temperature control was characterized and is shown in Figure 54 to be able to hold the temperature stable to $14.99 \pm .08\,^{\circ}\mathrm{C}$ over a period of 800 seconds. The temperature measured is that of the aluminum blocks which are coupled through vias and copper strips on the readout board to the MPPCs. The crystals are highly thermally insulating, but reach a steady state through contact with the MPPCs and the aluminum enclosure, eventually reaching $15\,^{\circ}\mathrm{C}$. The time required for the detector to reach $15\,^{\circ}\mathrm{C}$ is about 10 minutes as shown in Figure 54.

5.3 Calibration Procedure

The energy deposition in each crystal registers at the preamplifier as a voltage versus time for which the height depends on the energy deposited and the thermal properties of the detection system. As referenced in Section 4.3.3, the voltage versus time is not stored, but rather the total sum of the voltage vs time over a 8 microsecond period. The total sum is calibrated to energy deposited by measuring the detector

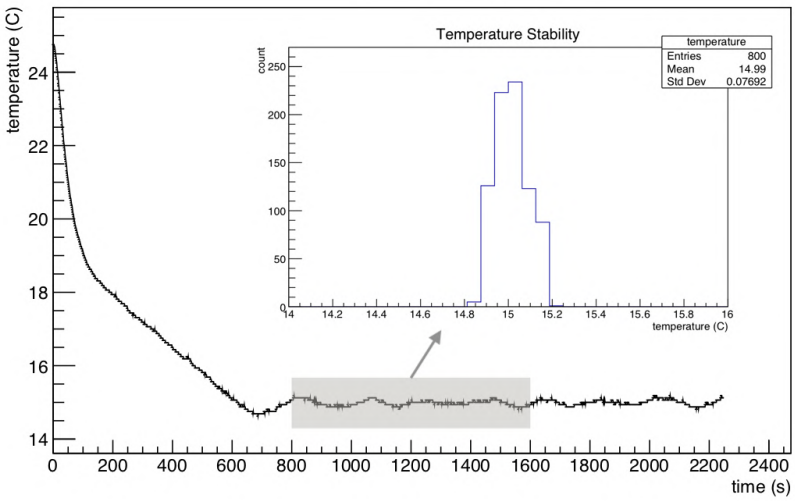

Figure 54: The measured temperature of a cooling module aluminum block cooled with a thermo electric cooler over a period of 40 minutes. The temperature reached the target in 10 minutes and was stable to less than 0.1 degrees Celsius.

response of each crystal to a Na-22 radioactive source. During calibration, the cooling blocks are held to 15 °C. Na-22 decays into Ne-22 (90.6%) emitting a β^+ in the process followed by a 1.27 MeV gamma-ray. The β^+ slows down eventually annihilating with an electron and produces two 0.511 MeV gamma-rays which are shot in opposite directions. The multiple reactions associated with Na-22 makes it a useful source for calibration. Before beginning measurements of the proton beam, the detector is calibrated to a Na-22 source using a 3-point fit (0, 0.511 MeV, 1.27 MeV). The source is taped to the detector directly in the middle and to the side of each crystal as shown in Figure 55. The calibrated pulse integral distribution is plotted for all the crystals in Figures 56 and 57. The photoelectric peak is clearly visible for both 0.511 MeV and 1.27 MeV for all the crystals.

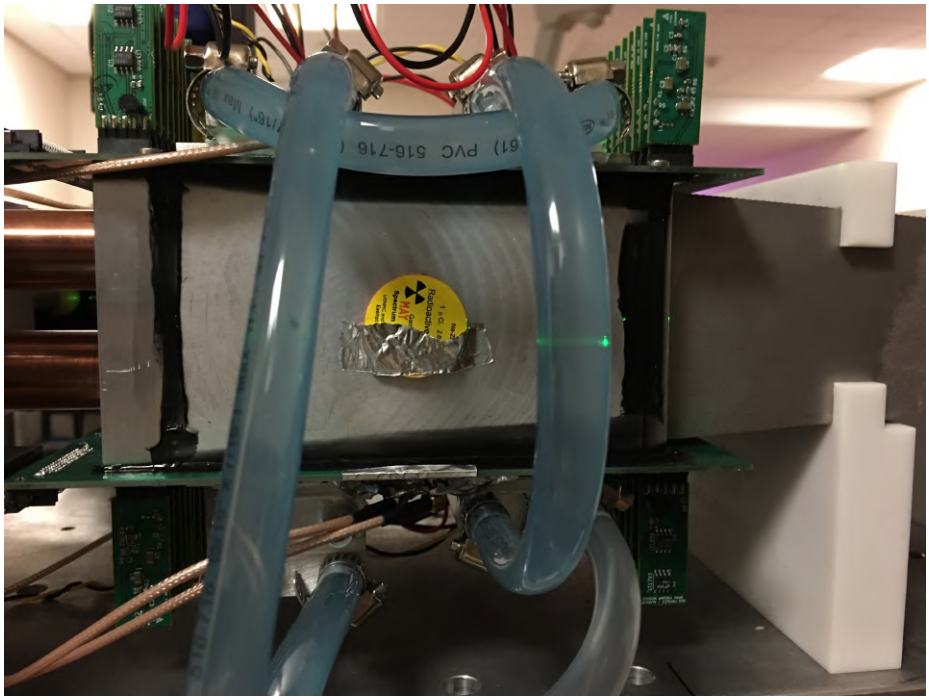

Figure 55: The Na-22 source placed on the detector for calibration purposes. The placement is near the center of each detector so that each channel of the detector can be calibrated for positioning if necessary.

5.4 Range Measurement Setup and Procedure

Measurements for characterizing the detector were made at the Mayo Clinic Proton Therapy Center in Phoenix, AZ. The facility has 5 treatment rooms, 4 of which are intended for treatment of patients. The 5th room has a fixed beam (no gantry) intended for research, which is where the measurements for this work take place. Although the beam can be steered to accommodate a 30 cm x 40 cm field, in this work the beam is always fixed, parallel with the ground going through the isocenter and into the acrylic block. The beam parameters for each measurement are given in Table 3.

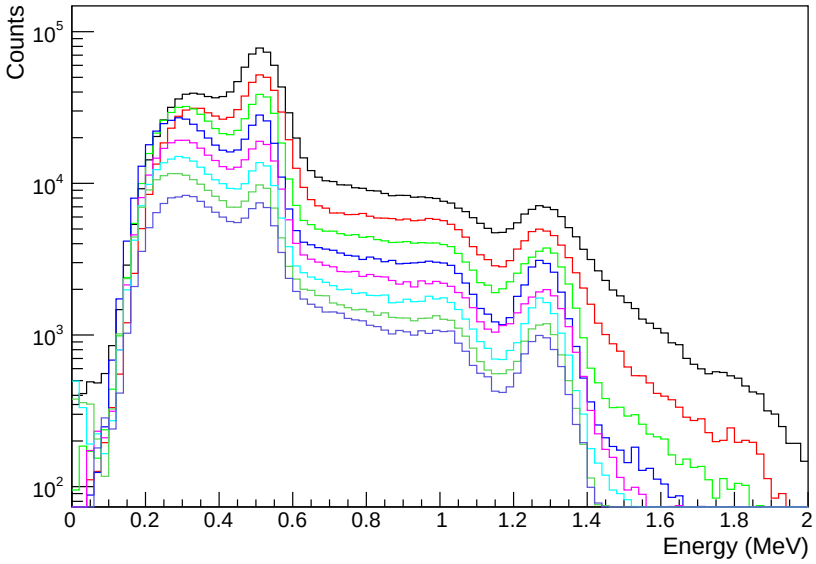

Figure 56: Crystals 0 through 7 response to Na-22. The source was placed on the side of the detector with crystal 0 nearest to the source and crystal 7 furthest.

5.4.1 Setup

The most common target in radiation therapy is water, called a water phantom. Water phantoms require a tank to define the boundaries and the tank material has to be strong enough to not bow due to the water pressure, which may effect the range measurements. To avoid these complications, acrylic is used in place of the water. Acrylic is composed of Hydrogen, Oxygen, and Carbon and is commonly used as a substitute for water in radiation therapy. The density of acrylic is 1.19 g/cm^3, a bit more dense than water.

The acrylic phantom has dimensions 8.75" x 8.00" x 16.00". The phantom is positioned such that prompt gamma-rays emitted along the beam axis have to travel through approximately 8 cm of the acrylic phantom before reaching the detector.

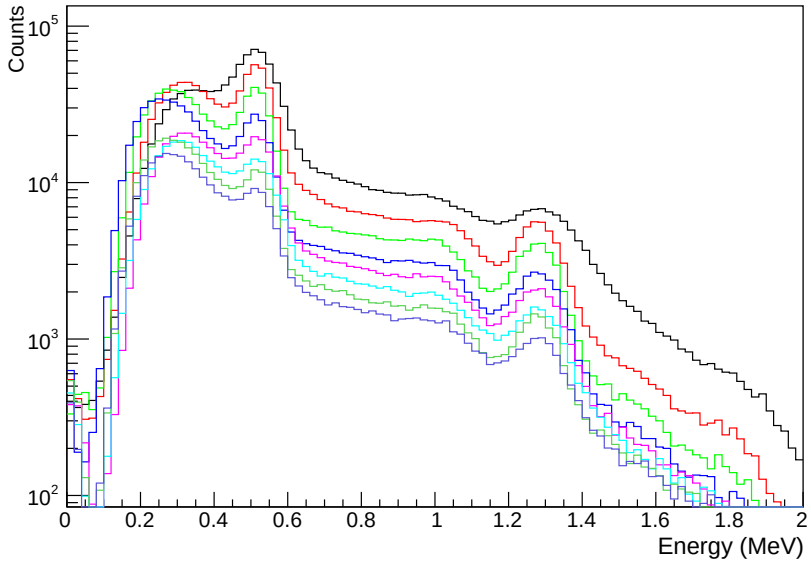

Figure 57: Crystals 8 through 15 response to Na-22. The source was placed on the side of the detector with crystal 15 nearest to the source and crystal 8 furthest.

There is a 2 cm air gap between the phantom and the collimation. The beam axis runs along the center of the detector height. Figure 58 shows the initial measurement configuration of the detector for measuring the range in an acrylic phantom. Figure 59 shows images of the setup at the fixed-beam room at the Mayo Clinic Proton Therapy facility.

5.4.2 Procedure

Due to budget constraints, the detector was designed to be read out only half at a time. The data acquisition system has 32 channels and each scintillation crystal requires 4 channels (8 MPPCs per channel, 32 MPPCs per crystal). To read the

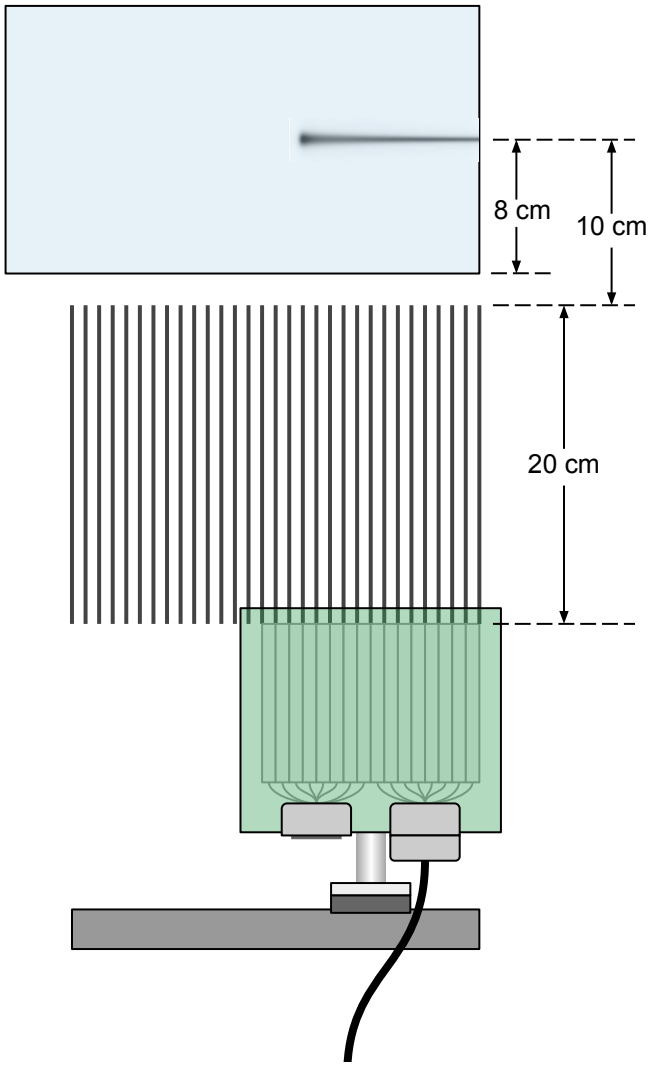

Figure 58: The initial setup and alignment of the detector for the range measurements.

entire detector at once, 64 channels of DAQ are required. In addition, it is desired to mimic a 30-crystal detector. A procedure has been implemented allowing for accurately mimicking 30 crystals while reading 8 crystals at a time. The procedure is demonstrated by Figure 60. The detector is read out in 4 steps, where the beam is repeated in each. Half the detector is read out in each sequence, and the detector is moved using a motorized positioning system between the 2nd and 3rd sequence.

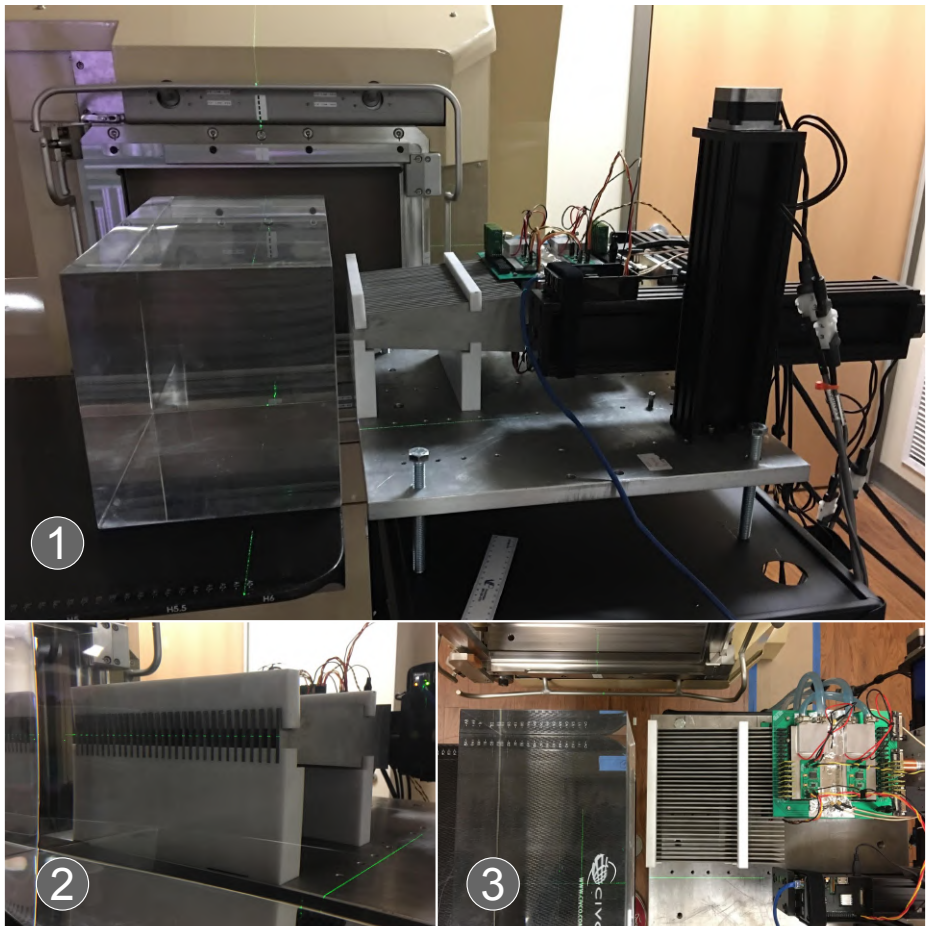

Figure 59: Images showing the detector alignment to the laser system and of the overall testing environment.

A typical measurement following the prescribed procedure is shown in Figure 61. The last step in the procedure is to eliminate the upstream two crystals from analysis in the 3rd position. These two crystals are eliminated since they are the most exposed to the beam. By eliminating the upstream two crystals in the 3rd position, the most prominent edge effects are eliminated thus simulating a continuous detector. Even with this precaution, systematic errors are surely introduced to the system as compared to simply having a 30-crystal detector read out simultaneously.

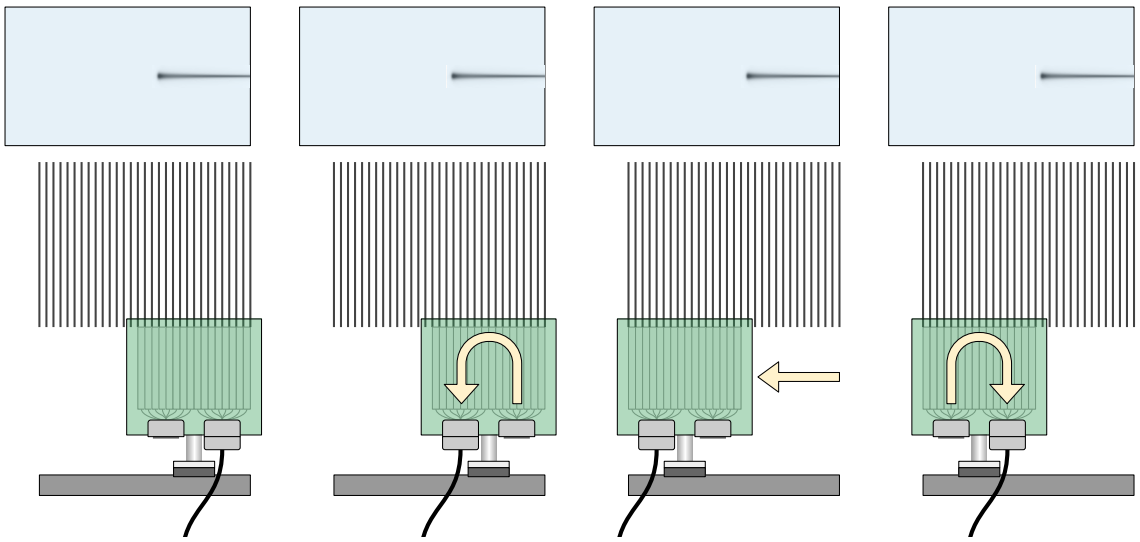

Figure 60: The measurement procedure working from left to right. The detector is readout 8 crystals at a time and the full measurement mimics 30 crystals.

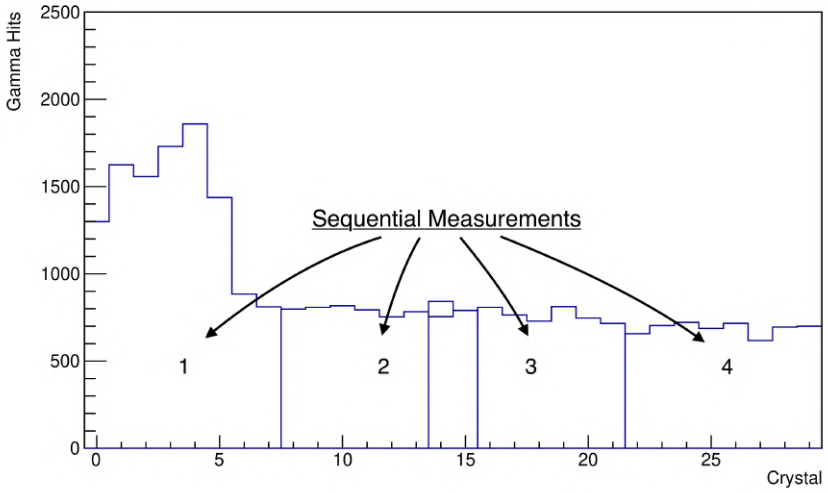

Figure 61: A typical measurement demonstrating the different detector positions.

5.5 Data Selection

The process for selecting data is motivated by the underlying nuclear physics and the measurement limitations introduced by the detector materials and electronics. By making proper cuts on the data, the background noise caused by neutrons and uncollimated gamma-rays can be reduced to levels appropriate for measuring the range. This section will outline the data selection process.

5.5.1 Pulse Shape

Pulse shape discrimination was explained in Section 4.4.2. The pulse shape analysis was initially developed for discriminating between gamma-rays and neutrons, however neutrons often interact with the scintillator, resulting in a gamma-ray emitted by the scintillator material. The only case where neutrons can be discriminated is when the neutron causes a secondary proton or alpha to kick out of the scintillator nuclei, which is a rare event and requires neutron energies beyond the binding energy holding the protons and alphas within the nuclei. However, after using the detector at the beam line it was discovered that the detector is occasionally hit directly by protons from the beam line. Direct charged particle interactions can be removed through pulse shape analysis. Additionally, pileup is easily removed when using pulse shape analysis since the after pulses make the slow part of the signal larger.

The pulse shape analysis used in the range measurements is demonstrated in Figure 62a. The pileup, direct proton hits, and the preamp saturation are all visible through the use of pulse shape analysis. Figure 62b demonstrates how the gamma-rays

(electron line) are selectable. The cuts shown are the same that are used in the range measurement analysis.

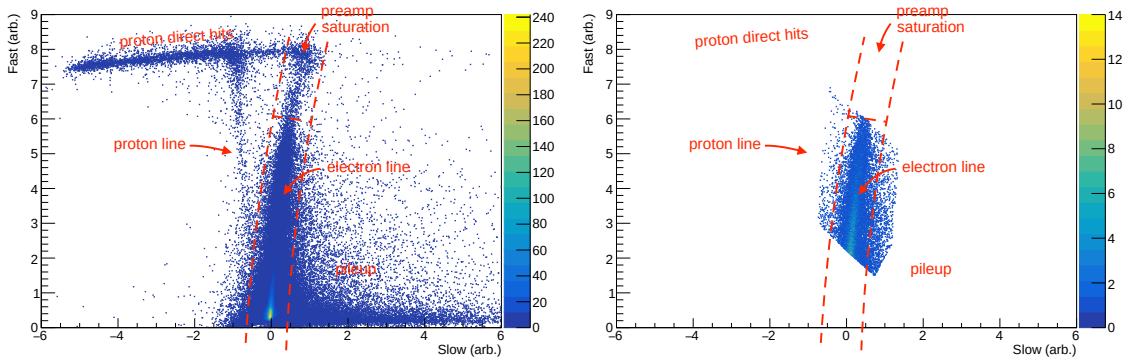

(a) no cuts

(b) PSD and energy cuts

Figure 62: The fast versus slow scatter plot with and without cuts applied. The various features of the plot are labeled to show how the data is selected. Note that this plot also includes cuts on the energy.

5.5.2 Timing

Although the synchrotron does not bunch the protons to a level that allows for using time of flight to reduce the neutron background, timing is still important for analyzing the proton scanning spots. Also, timing can be used to eliminate background pulses when the beam is off or between spots. In the runs measured at Mayo Clinic, a background is present when the beam is off. The timing structure of the beam on small and large time scales as measured by the range detector is shown in Figure 63a and Figure 63b. In Figure 63a, a background is noticed when the beam is off and in Figure 63b, the background is seen between spots. In this work, data that does not exceed 30 kHz for when the data is binned at 0.1 ms is not included in the analysis.

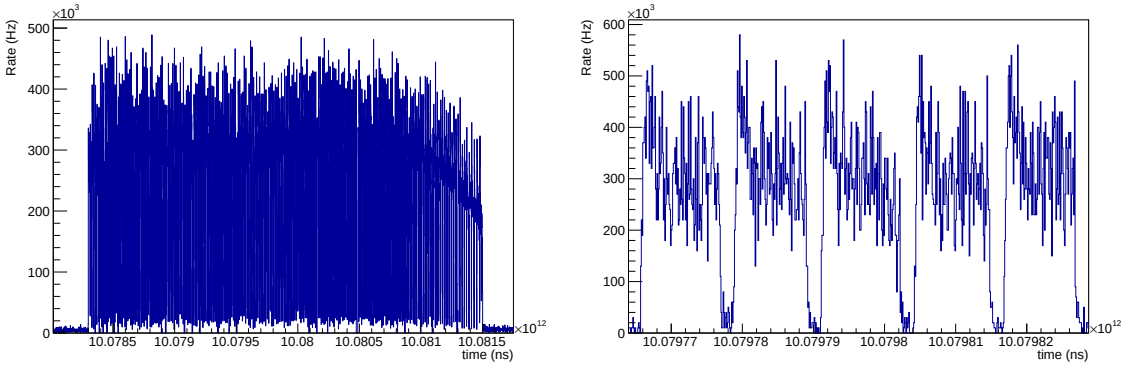

(a) 250 spots

(b) 5 spots

Figure 63: The time structure of the proton beam at Mayo Clinic in Arizona as measured by the range detector. On the left, the width of the group of spots is about 3 seconds. Each spot contains approximately 5 x 10^7 protons in this measurement and is approximately 10 ms in duration.

5.5.3 Energy

Ideally, the range detector should select the 4.4 MeV (1st excited state of Carbon-12) and the 5.2 MeV line (made up of many reactions) and reject the 2.22 MeV line (neutron capture on Hydrogen). The only way of making such strict energy cuts is to have good energy resolution and to detect the entirety of the gamma-ray energy most of the time. At these energies, however, photoelectron interactions are suppressed (see Figure 22) and therefore multiple detector hits are typically required to detect the total energy. In selecting data for this detector, the timing information for each pulse does not allow a clustering of nearby crystals for each event and as such, less strict energy cuts have been made. To eliminate the effect of the 2.22 MeV gamma-rays which are emitted by neutron capture on Hydrogen, energy deposits of less than 2.22 MeV are eliminated from the analysis. Due to saturation of the preamp electronics, all energies deposits above 6.5 MeV are eliminated from the analysis.

Because the detector is measuring mostly Compton scattering and pair production, the energy spectra for the crystals does not contain distinct peaks in energy for the most part, however the response to 4.4 MeV is noticeable. The measured energy spectrum of crystal 4, which is located near the Bragg Peak along the z-direction for a 71.3 MeV proton beam is shown in Figure 64a. A peak in the energy spectrum is seen to be near 3 MeV to 3.4 MeV. For crystal 0 in the same run, the energy spectrum is shown in 64b, which does not show a noticeable peak. The peak is attributed to the Carbon-12 4.4 MeV de-excitation gamma-ray interacting with the crystal by producing an electron-positron pair (pair production) followed by the electron and positron depositing most of their energy into the crystal followed by the positron annihilating with an electron and emitting two 0.511 MeV gamma-rays, where one or both escape the crystal. The phenomenon is well-known and is referred to as single and double escape peaks in the energy spectrum. Single and double escape peaks are common for thin detectors and results in 3 peaks separated by 0.511 MeV, 4.4 MeV, 4.4 MeV $-$ 1(0.511 MeV) = 3.9 MeV, 4.4 MeV $-$ 2(0.511 MeV) = 3.4 MeV. For added confirmation, the detector response was simulated in GEANT4. Figure 65 shows the response of the detector to 4.4 MeV gamma-rays, which shows the single and double escape peaks.

By accepting only energy deposits above 2.22 MeV and below 6.5 MeV, the signal to noise of the detector is greatly improved. The detector hit counts versus crystal before applying cuts and after applying cuts are shown for 88.5 MeV in Figures 66a and 66b respectively and for 117.1 MeV in Figures 67a and 67b respectively.

Since the synchrotron does not allow the possibility of using time of flight to reduce

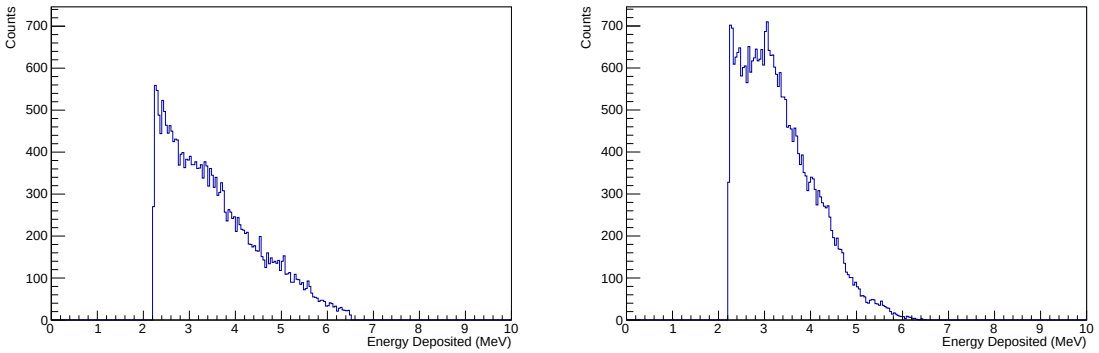

(a) crystal 0 (b) crystal 4

Figure 64: The measured energy spectra for crystals 0 and 4 respectively for a 71.3 MeV proton beam, where crystal 4 is near the Bragg Peak along the beam axis.

the neutron background, making good energy cuts becomes the primary method for reducing the neutron background. Future work will include improved energy resolution and clustering of hits into single gamma-ray events, which will allow for more effective background reduction.

5.6 Range Determination Analysis

The process for determining the range for a single measurement is outlined in this section. After selecting the data, the total number of hits are tallied for each crystal i, giving h_i. Figure 68 shows the resulting h_i for beam energies of 71.3 MeV, 78.5 MeV, 88.5 MeV, and 103.6 MeV.

To extract the range from the measured h_i, the detector response is simulated in GEANT4 for energies ranging between 65.4 MeV and 147 MeV in range increments of 2 mm. In total, 59 beam energies were simulated using 10^9 protons each. The tallied hits in each crystal and for each energy are contained in H_{ij}, where i denotes the

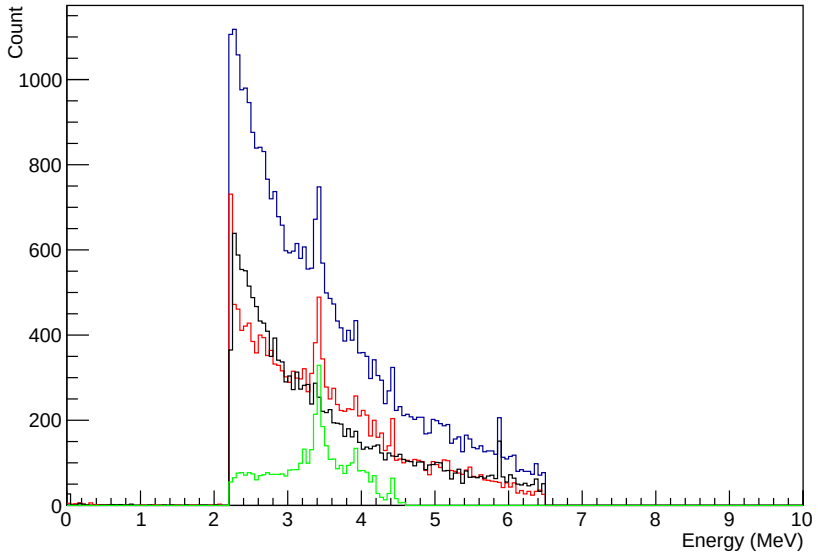

Figure 65: The simulated energy response of the detector to the proton beam interacting with the acrylic phantom. The detector response to all incident gamma-rays (red) and neutrons (black) adds to the total response (blue). The red curve is just the response of the detector to 4.4 MeV gamma-rays, showing the single and double escape peaks from pair production caused by the 4.4 MeV gamma-rays, which is also visible in the total response.

simulated crystal number and j denotes the simulated beam energy. Each measured response h_i is scanned over all the simulated responses H_{ij} calculating the respective correlation coefficient r_j for each,

$$r_j = \mathrm{corr}(h_i,\, H_{ij}) \ . \tag{5.1}$$

Figures 69 and 70 shows the resultant r_j for a 78.5 MeV beam (range in acrylic is 4.32 cm) and a 117.1 MeV beam (range in acrylic is 8.80 cm) respectively. The uncertainty in r_j is $\frac{1-r_j^2}{\sqrt{N}}$, where $N = 30$ (number of crystals) [12]. Since the "true" range may not correspond to one of the simulated energies, a fit to r_j is necessary for

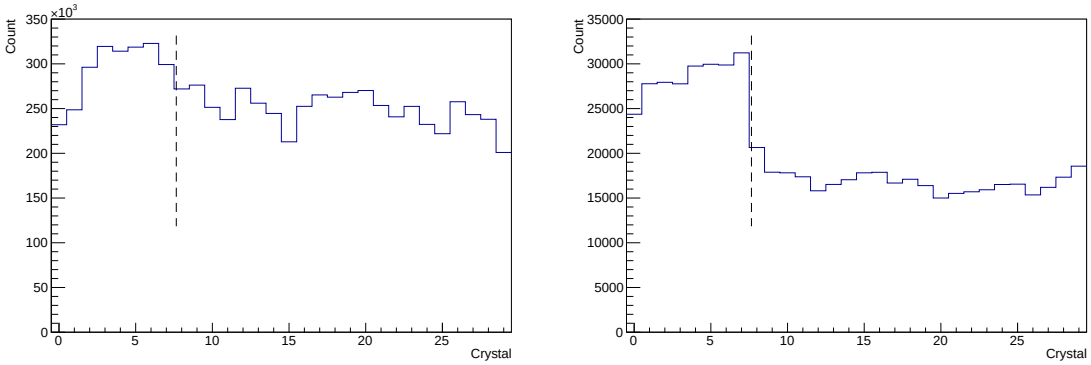

(a) pre-cuts (b) post-cuts

Figure 66: The detector hit counts versus crystal number before applying cuts and after applying cuts for an 88.5 MeV proton beam with 1000 spots and 5 x 10^7 protons per spot.

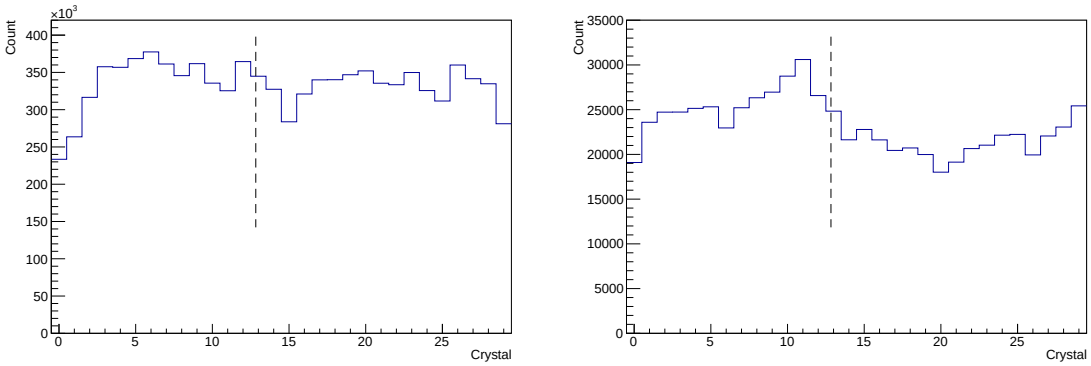

(a) pre-cuts (b) post-cuts

Figure 67: The detector hit counts versus crystal number before applying cuts and after applying cuts for a 117.1 MeV proton beam with 1000 spots and 5 x 10^7 protons per spot.

extrapolating between the points. The maximum of the fitted curve corresponds to the most well matched range.

The curve shape of r_j is not well described by any analytical function. For this reason the data is fit to a spline, in particular the BSpline method of the python scipy

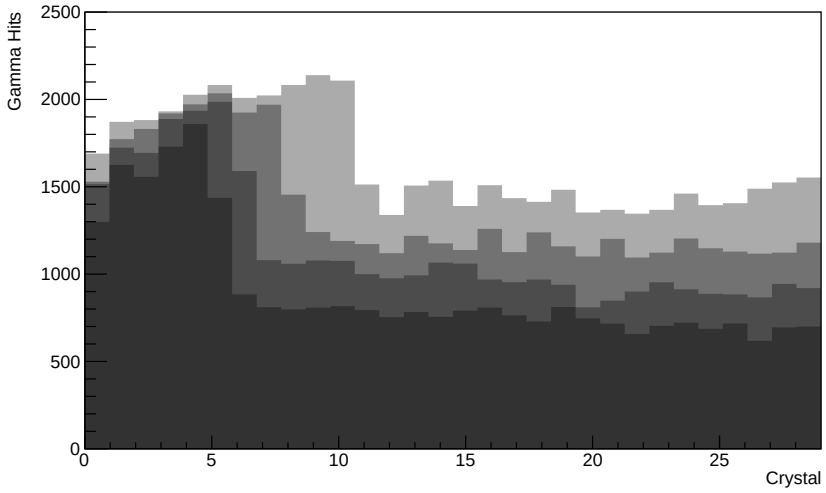

Figure 68: The detector hits versus crystal number for beam energies of 71.3 MeV, 78.5 MeV, 88.5 MeV, and 103.6 MeV, each using 1000 spots with 3 x 10^6 protons per spot.

library. The spline input parameters are determined by minimizing the systematic error between the expected and determined range for the various tested beam energies. For minimizing the systematic error in the range measurements, the 3 x 10^6 protons/spot data was chosen since the prompt gamma-ray rates are lowest and most easily handled by the detector.

5.7 Range Measurement Results

As the beam energy increases, the incident particle rates increase (see Figure 18 in Section 3.1). With higher beam energies, the pileup rates increase and the pulse shape analysis removes an increasing amount of data. Because the detector is able to handle pileup using pulse shape analysis, the range can still be measured, however more protons are required. Improved rate handling capabilities will allow for a quicker

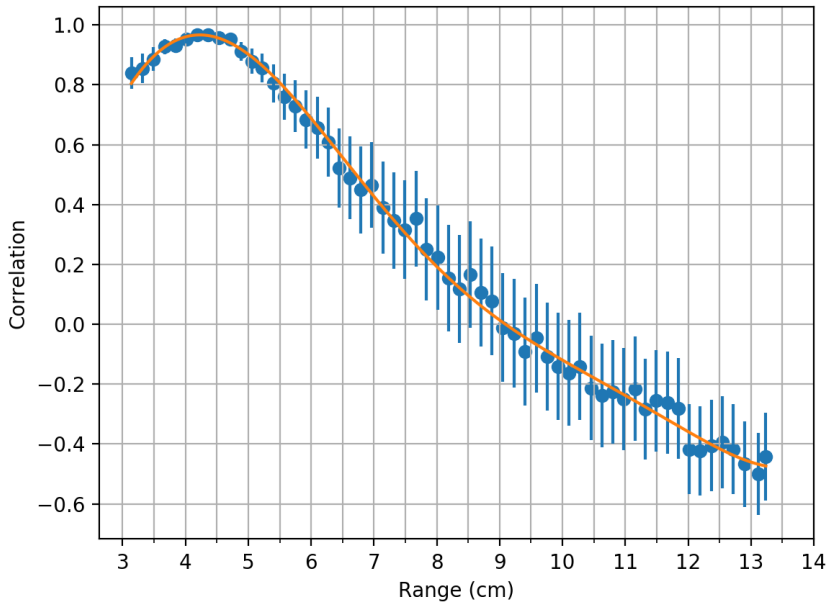

Figure 69: A plot of the correlation between the measured data set h_i and the simulated data sets H_{ij} for a 78.5 MeV beam measurement with an expected range in acrylic of 4.32 cm.

range measurement. Figure 71 shows the reducing acceptance of data as the energy increases. Since beam current does not exceed about 1 nA, the curves in Figure71 shift upward, but the shape is similar once the number of protons per spot reaches 5 x 10^7. Increasing the rate handling of the detector will be a point of improvement for future work.

Each run consists of 1000 spots. The range uncertainty is dependent on the number of spots used in the range measurement analysis. To find the number of protons required for each beam to achieve 1 mm range uncertainty, the analysis was performed on subsets of the total data set. 20 spots of data pulled from the 1000 spots are analyzed repeatedly and histogrammed. Figure 72a shows the range measurements for

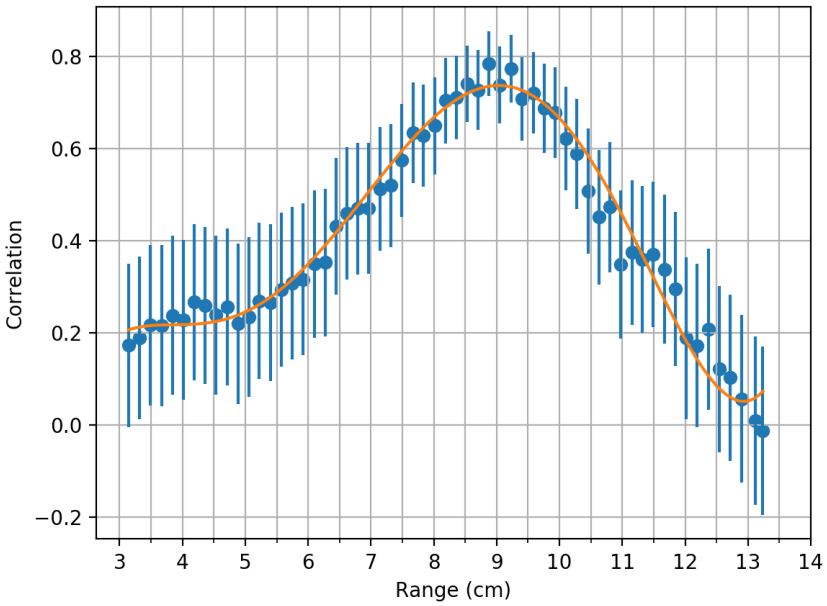

Figure 70: A plot of the correlation between the measured data set h_i and the simulated data sets H_{ij} for a 117.1 MeV beam measurement with an expected range in acrylic of 8.80 cm.

20 spots, 5 x 10^7 protons per spot. The standard deviation in each set of measurements is taken as the range uncertainty for the set. 5 x 10^7 protons per spot was chosen as a main point of analysis due to it being a representative amount of protons per spot for patient treatment. The statistical uncertainty/range uncertainty and systematic errors are seen in Figure 72b, where the expected range and the measured range are plotted. The systematic errors are most likely caused by positional misalignment in the setup and shortcomings of the sequential measurement procedure. A plot showing the range uncertainty versus the number of spots for 5 x 10^7 protons per spot is shown in Figure 73. The range uncertainty is seen to go below 1 mm for each beam energy at a number of protons that is not far from the project goals. The results are extremely promising.

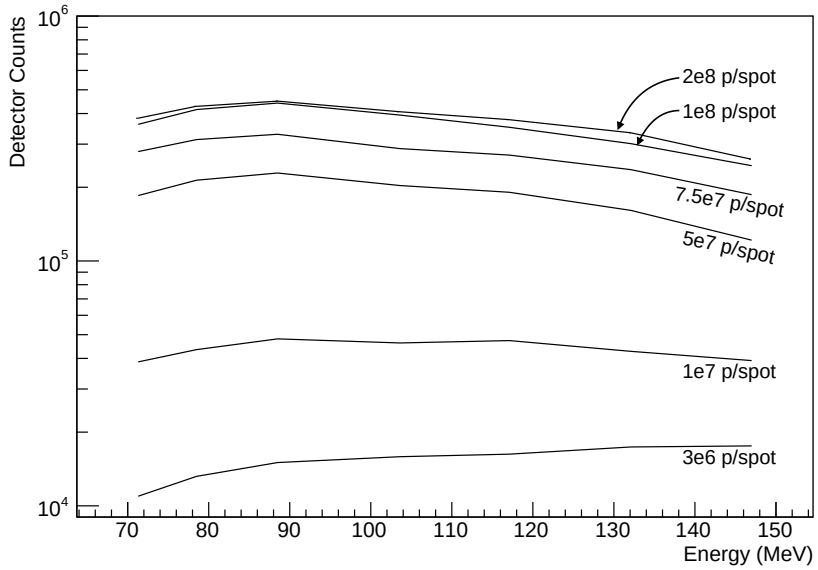

Figure 71: The acceptance rate of the detector after applying cuts on the raw data. The data acceptance decreases with increasing beam energy due to increasing levels of pileup.

5.8 Future Hardware Upgrades

The two most important upgrades for future designs are the ability to handle higher prompt gamma-ray rates and to increase the energy resolution, both of which will allow for deeper measurements hopefully reaching 20 cm. To handle the rates, either the scintillation material could be changed or the scintillation material could be further segmented. The best way to improve energy resolution is to cluster crystal hits into events using timing information, which would allow for a sum of hits from different crystals. To improve the timing, the pulse samples need to be analyzed by the FPGA using extrapolation between the sample times in order to achieve sub-sample timing resolution. To improve on rejecting the background neutrons, the energy resolution needs to be improved and investigations into neutron absorber shielding should be

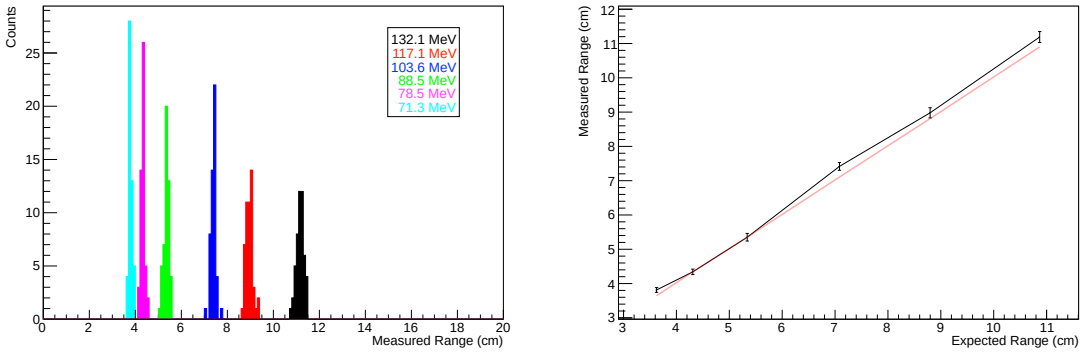

(a) (b)

Figure 72: The range measurement results for 20 spots, 5 x 10^7 protons per spot. The red line on the left is 1:1 for showing the systematic errors in the range measurement.

performed. To test the field of view, new taller collimation with no tapering will need to be acquired. The temperature control of the detector was over designed which caused other aspects of the design to suffer, for example leaving little room on the readout board for amplifiers. Instead of a cooled design, a design which monitors the temperature and perhaps regulates it near room temperature using fans would be much simpler and with little consequence to the overall detector performance. The DAQ should be transitioned to a custom design instead of the National Instruments DAQ in order to more easily scale to more channels. The MPPCs were readout in groups of 8, which is too many to be connected in parallel. Amplifying each MPPC individually is desired, which would require 512 channels of DAQ for the same design. Having more channels would also allow for additional information to be pulled from the detector, such as imaging within the crystals, enabling a more sophisticated analysis technique.

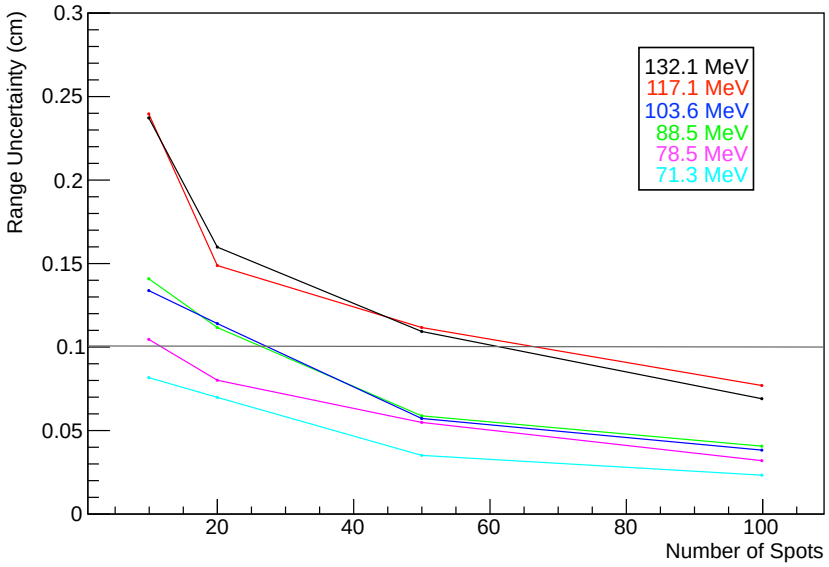

Figure 73: The range uncertainty versus the number of spots used in the range measurement. This plot shows the results for 5 x 10^7 protons per spot.

5.9 Future Measurements

The detector needs to be characterized for a larger field of view more suitable for use with patients. After upgrading the hardware, the detector should be scaled to more crystals to allow for measurements involving patients. Initial patient measurements could involve treatments to the brain as it is uniquely suited to proton therapy and fits within design considerations of an early stage range detector. To prepare for patient measurements, an inhomogeneous target such as a water phantom with objects placed into the tank. It is expected that the analysis described in this work would be well suited to inhomogeneous targets.

5.10 A Pathway Towards Clinical Usage

Much like the patient-specific quality assurance approach outlined in Section 2.6.2 where the measured data is checked for agreement with the treatment plan, the pathway towards clinical usage for the range detector is to simulate the range detector response as part of the treatment plan. During the real treatment, the simulated detector response is checked for agreement with the measured response. The detector can be introduced into the treatment planning software by adding nuclear interactions into the model. A Monte-Carlo based treatment planning approach is best suited for introducing nuclear interactions.

In preparation for the treatment, the range detector could be pre-loaded with the simulated detector response. During treatment, the measured response would be constantly compared with the simulated response in real time. Because the detector has a time response on the order of 100 ms, if the measured data were different from the simulated data, the beam could be shut down before any harmful amount of dose is given.

This type of range detector implementation is better described as an advanced form of dose verification. The range of the detector never needs to be explicitly measured, however, sensitivity to the range is a requirement. As an anecdote, the range detector orientation is not required to be parallel to the beam direction since the range is not the target measurement, but rather the deviation from the simulated response. This will help with simplifying the positioning of the detector, so that it only needs to be positioned once per treatment fraction. The optimal position could be solved as part of the treatment planning software.

As a final note, this implementation can be used as a fail safe, but it is recommended

to combine the fail safe with an actual imaging of the beam facilitated by the detector. Since the range detector measures information about the range of the protons, if combined with a 2D fluence detector, the entire dose image could be reconstructed. More work in this direction is planned. Having a 3D image of the reconstructed dose along with the fail-safe capabilities could help proton therapy to reach its full potential and offer patients improved outcomes over other radiation therapy modalities.

Measurement	Energy (MeV)	protons/spot	MU/spot	spots	MU
1	71.3	3E+06	0.0074	1000	7.40
2	71.3	1E+07	0.0247	1000	24.67
3	71.3	5E+07	0.1234	1000	123.35
4	71.3	7.5E+07	0.1850	1000	185.03
5	71.3	1E+08	0.2467	1000	246.70
6	71.3	2E+08	0.4934	500	246.70
7	78.5	3E+06	0.0068	1000	6.84
8	78.5	1E+07	0.0228	1000	22.82
9	78.5	5E+07	0.1141	1000	114.08
10	78.5	7.5E+07	0.1711	1000	171.12
11	78.5	1E+08	0.2282	1000	228.16
12	78.5	2E+08	0.4563	500	228.16
13	88.5	3E+06	0.0062	1000	6.22
14	88.5	1E+07	0.0207	1000	20.75
15	88.5	5E+07	0.1037	1000	103.73
16	88.5	7.5E+07	0.1556	1000	155.59
17	88.5	1E+08	0.2075	1000	207.45
18	88.5	2E+08	0.4149	500	207.45
19	103.6	3E+06	0.0055	1000	5.51
20	103.6	1E+07	0.0184	1000	18.38
21	103.6	5E+07	0.0919	1000	91.92
22	103.6	7.5E+07	0.1379	1000	137.87
23	103.6	1E+08	0.1838	1000	183.83
24	103.6	2E+08	0.3677	500	183.83
25	117.1	3E+06	0.0050	1000	5.04
26	117.1	1E+07	0.0168	1000	16.79
27	117.1	5E+07	0.0840	1000	83.96
28	117.1	7.5E+07	0.1259	1000	125.94
29	117.1	1E+08	0.1679	1000	167.92
30	117.1	2E+08	0.3358	500	167.92
31	132.1	3E+06	0.0046	1000	4.62
32	132.1	1E+07	0.0154	1000	15.41
33	132.1	5E+07	0.0770	1000	77.04
34	132.1	7.5E+07	0.1156	1000	115.56
35	132.1	1E+08	0.1541	1000	154.08
36	132.1	2E+08	0.3082	500	154.08

Table 3: Range detector testing plan used in the fixed-beam room at Mayo Clinic in Arizona.

Chapter 6

PRINCIPLES OF GAS DETECTORS FOR MEASURING PROTON BEAM FLUENCE

From a quality assurance perspective, pencil beam scanning (PBS) differs from passive scanning in that the beam has a small diameter on the order of one centimeter and that the beam is delivered in spots and energy layers. Even still, patient-specific QA and aspects of machine QA are still performed more from the perspective of passive scanning in that there are no techniques which utilize the timing structure of the beam. Very few QA techniques analyze the treatment on a spot by spot basis, or more generally at higher bandwidth. The only spot analysis performed at Mayo Clinic in Arizona is an analysis of the log files from the accelerator. One of the main reasons for the missing quality assurance done at higher bandwidth among the medical physics community is a lack of available equipment which can operate at high speeds and that meet the high specifications demanded in radiation therapy. As the industry has moved into PBS, quality assurance detectors have not been updated to match the new capabilities of PBS proton therapy. In this work, development and preliminary results of a fast and accurate fluence detector which can perform spot by spot analysis is presented. A fluence detector is a gas detector which measures the beam profile and the beam current. A well designed fluence detector can be used in a variety of quality assurance measurements.

6.1 Ionization of Gas

A gas-based detector measures the amount of ionization caused by incident particles as they pass through the active gas volume. As gas molecules become ionized, an electric field causes the resultant electron-ion pairs to separate, inducing a current on the electrodes as they drift. In general, the average energy required to produce an electron-ion pair in gas will vary depending on the incident particle type and its energy. However, for protons with energies relevant to proton therapy, the average energy required to produce an electron-ion pair is nearly constant, reducing by probably less than 1% as energy increases. For proton with therapeutic energies in air, $w = 34.2$ eV [34]. For protons in Argon with energies relevant to proton therapy, $w = 26$ to 27 eV [9].

6.2 Charge Induction on the Electrodes in Current Mode

The detector signal is a measure of charge induced on the electrodes by the electron-ion pairs created within the detector. The total induced charge on all electrodes is equal and opposite to the charge within the chamber. For a single electron-ion pair created within the detector chamber, Figure 74 demonstrates the charge induced as a function of time and the resulting current on each electrode for when the electron moves straight down into pixel 2. Notice that for pixel 1 and pixel 3, the induced current alternates above and below zero, while pixel 2 only has positive current. The instantaneous current for each pixel is non-zero, however for an integrating readout that integrates for a time period longer than the drift time of the ions the currents in pixel 1 and pixel 3 integrate to zero. This is due to the total induced charge being

zero over long time periods. Pixels 1 and 3 are known as "spectator pixels" due to this phenomenon [20]. For current mode readout where the charge collection efficiency is approximately 100%, the detector signal can be said to be equal to the charge collected at each pixel.

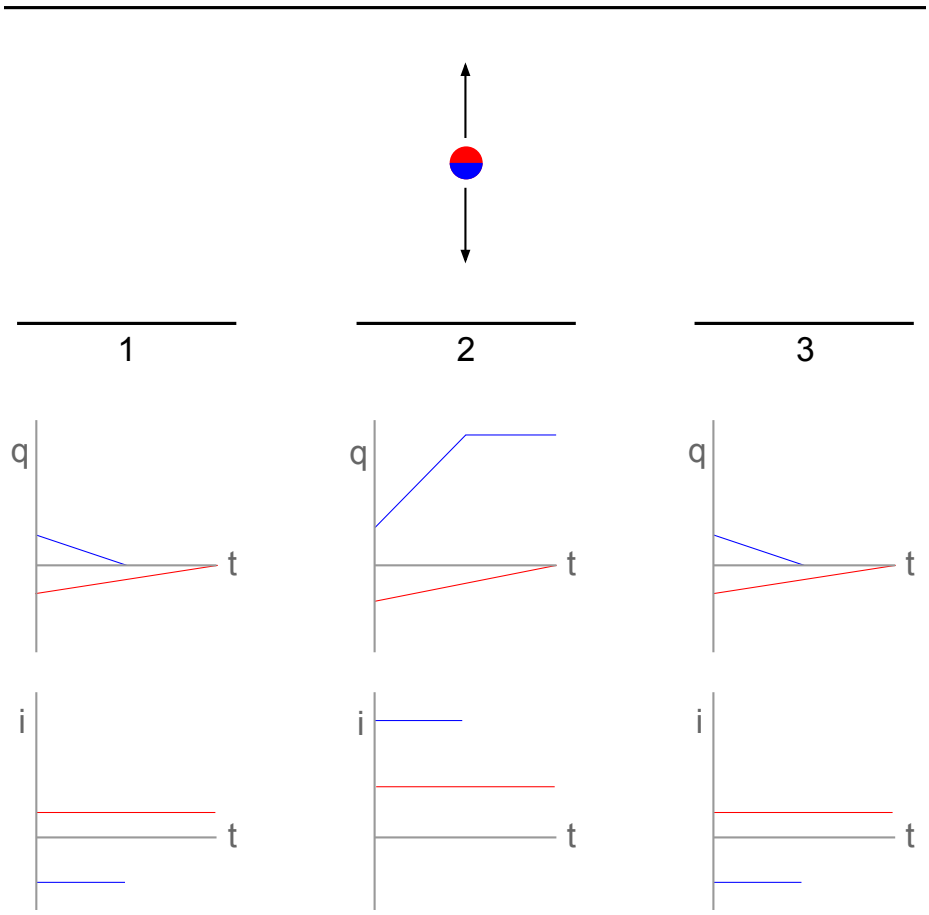

Figure 74: The induced charge (a simplified case) for a single electron-ion pair and the resulting induced current for a pixelated ionization detector. The blue lines represent the electron-induced charge and current. The red lines represent the ion-induced charge and current. The drift time for the ion is in reality much longer than the drift time for the electron (not to scale in drawing for demonstration purposes).

6.3 Ionization Current

The amount of energy deposited into the detector depends on the beam energy. Using GEANT4, a 2 cm thick argon-gas detector was simulated to measure the energy deposited for minimum ionizing particles (MIP). The total energy deposition in the gas volume was recorded for each particle and plotted, shown in Figure 75. The most probable energy deposition for a MIP is 2.7 keV in 2 cm of argon. Using 27 eV as the average energy to produce an electron-ion pair for argon, the number of electron-ion pairs per cm for minimum ionizing particles is found to be approximately 50.

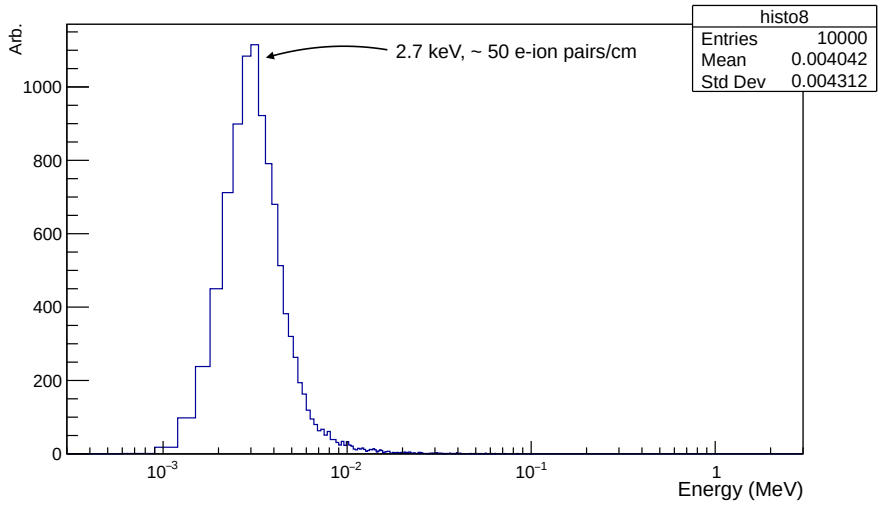

Figure 75: The energy deposition distribution for minimum ionizing protons (about 2 GeV) traversing a 2 cm thick volume of Argon gas.

The total proton beam flux at the Mayo Clinic in Arizona is expected to be 10^{10} protons per second (10 GHz). To calculate the expected ionization current versus beam energy, protons at various energies were shot through a 1 cm thick volume of

Argon in GEANT4. The mean value was taken for each energy deposition distribution and the ionization current per beam rate per detector thickness, $J(E)$, is plotted in 76. $J(E)$ is used as a conversion factor to measure the detector flux, Φ,

$$\Phi = \frac{I_{meas}}{J(E) * T} \ , \tag{6.1}$$

where I_{meas} is the measured ionization current and T is the detector thickness.

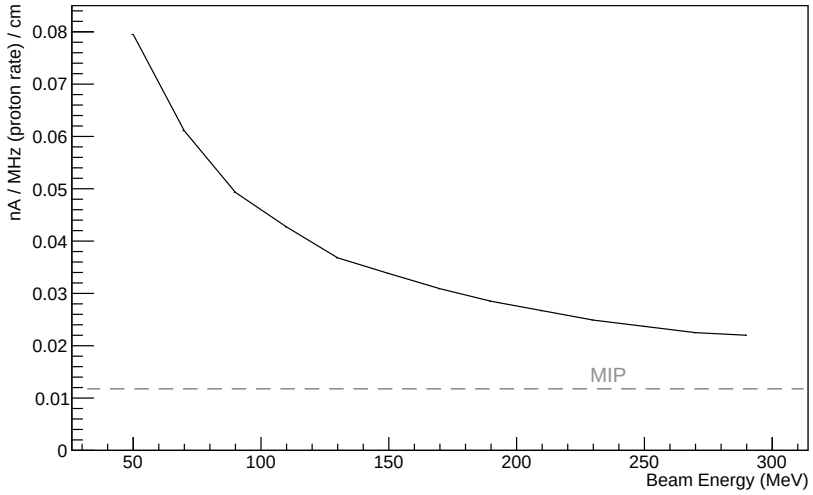

Figure 76: The ionization current found by shooting protons of various energies through a 1 cm thick volume of Argon gas. In each case, the same number of protons were used. Simulated in GEANT4.

6.4 Electron Transport in Gas

As the charge carriers (electrons and ions) drift within the gas detector, they interact with the gas molecules. The interactions are so frequent that the charge

carriers rarely gain energy above a few eV even with electric fields in the 100s or 1000s of V/cm. The drift velocity of electrons in a standard temperature and pressure (STP) gas chamber is typically on the order of 1 cm/μs - 10 cm/μs. Frequent collisions cause the charge carriers to diffuse with a small overall drift velocity along the direction of the electric field. The diffusion of charge carriers in the gas causes the signal for a single proton to spread out across the anode plane. For a 1 kV/cm field, P-10 gas (90% Argon, 10% Methane) at STP, and a 1.8 cm chamber height, the distribution for 100 identical 120 MeV protons was simulated in Garfield++, a toolkit for the detailed simulation of particle detectors [19]. The lateral drift caused by diffusion for a single proton in this configuration is approximately $\pm$0.5 mm, as shown in Figure 77a. Figure 77b shows the energy distribution of electrons just before reaching the anodes.

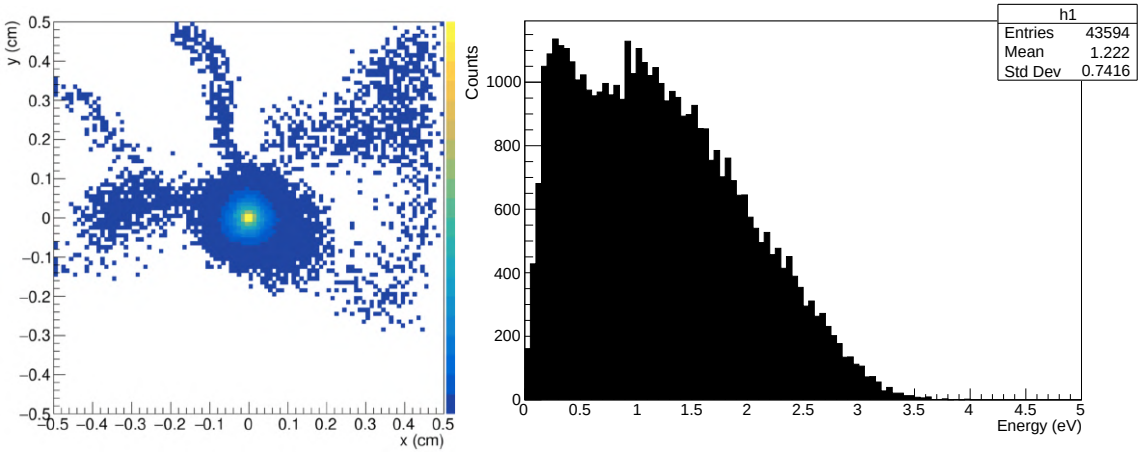

(a) Spatial Distribution

(b) Energy Distribution

Figure 77: Simulated in Garfield++, 120 MeV protons (x100) are shot through a 1.8 cm chamber of P-10 gas at STP. The drift field strength is 1 kV/cm. The plots shows the resulting ionization electrons spatial distribution and energy distribution after reaching the anodes.

6.5 Dead Volume of a Gas Detector

In an ideal parallel plate detector, the field strength is uniform throughout the volume. As electron-ion pairs are produced, if the field strength is high enough, electron-ion pairs will drift apart with a negligible probability of recombining. As the field strength is reduced, the probability of recombination increases. In any real detector design, the mechanical design will introduce spatial volumes where the field strength is reduced, such that the probability for recombination is elevated. At low enough field strength, the probability for recombination in those regions becomes high. In any pixelated electrode design, the electric field will go below the recombination threshold between each pixel creating a volume of dead space as outlined in Figure 78. As the electrode potentials are increased, the field strength scales and therefore the recombination threshold is moved further from the pixels, reducing the overall dead volume. The overall dead volume can also be reduced by reducing the spacing between pixels.

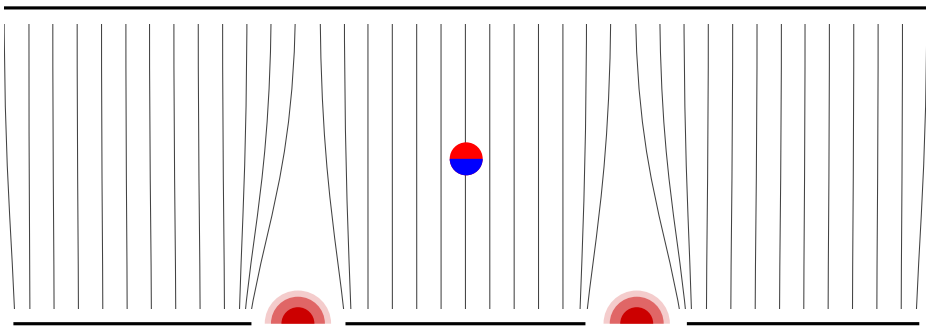

Figure 78: A diagram showing the electric field lines permeating the drift chamber. Due to a low potential between the pixels, the charge collection efficiency will drift below 100% in small volumes between the pixels.

6.6 Electron Multiplication in a Parallel Plate Gas Detector

In an electron avalanche, a primary ionization electron gains enough energy as it drifts towards the anode to ionize a gas molecule creating another electron. Each successive electron also gains enough energy to ionize a gas molecule, creating a chain reaction. Each generation of electrons in the avalanche generates a new generation of electrons after traversing a distance called the 1st Townsend Coefficient. The 1st Townsend Coefficient, α, is the number of electrons generated per unit path length or equivalently the inverse mean free path between ionizations. For a parallel plate detector, the multiplication factor M is then

$$M = e^{\alpha d} \ , \tag{6.2}$$

where d is the distance between plates. Generally, the 1st Townsend coefficient depends on the gas type, the gas pressure, and the electric field strength. At STP for gas-types allowing for electron avalanche, electron avalanche will begin to occur for electric field values starting around 20 kV/cm.

6.7 The Micromegas

One method for adding multiplication to a gas detector is to place a grid or mesh biased to a high voltage at a small height above the anode strips or pads. This has the effect of creating a region with a high electric field strength, which can cause electron avalanche to occur. This type of device is known as a Micromegas (Micro-MEsh Gaseous Structure). The Micromegas as first described by [39] is a gaseous detector consisting of two main parts, a conversion or drift region where the primary particle ionizes the gas creating electron-ion pairs, and a thin (30 μm - 150 μm) multiplication

region, where the electrons experience avalanche multiplication. The two regions are separated by a potential plane resulting in a large electric field strength in the multiplication region and a smaller electric field strength in the conversion region. The potential plane barrier between the drift region and multiplication region has to be physically placed above the anodes at a height of between 30 μm and 150 μm, which is a difficult process. The electrons which are created in the drift region traverse down towards the micromesh, but upon reaching the micromesh the electrons begin to feel the even stronger field beneath the micromesh and are pulled through the micromesh triggering the electron avalanche process. By tuning the bias properly at the cathode, micromesh, and the anodes, the electrons are able to pass through the mesh with high efficiency. A diagram outlining the fundamental principles of a Micromegas detector is given in Figure 79.

6.8 Raether Limit

The Raether limit is a limit on the number of electrons within a multiplication region that if exceeded, will cause a voltage breakdown or spark. Typically in a Micromegas, the Raether limit is 10^7 electrons [17]. The Raether limit becomes a problem for using multiplication in a hadron beam due to the small but non-negligible probability of a nuclear collision to occur within the gas detector. Approximately 1 in 10,000 protons will collide with a nucleus within the gas volume creating an energy deposit which can be 1000 times larger than a typical event. For a 10 GHz proton beam, the nuclear collision rate is approximately 1 MHz. For detector bandwidths below 1 MHz, the nuclear collisions are effectively constant. For a single nuclear collision depositing 1 MeV, there will be about 10^6 electron-ion pairs. So, if the

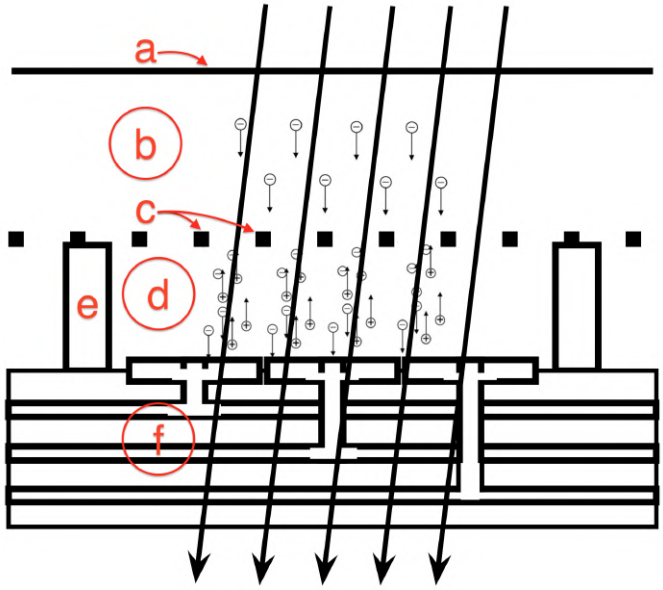

Figure 79: The fundamental principles of a Micromegas detector. (a) the biased cathode, which establishes the physical boundary of the drift region, (b) the drift or conversion region (usually about 0.5 to a few cm thick), where the incident particles are converted into electrons and ions, (c) the micromesh, which establishes the boundary between the multiplication region and the drift region and allows drifting electrons to enter from the drift region into the multiplication region, (d) the multiplication region (usually about 50 to 100 microns thick), where a high electric field causes an electron avalanche for electrons entering the region, (e) the spacer which serves to establish the height of the micromesh, and (f) the readout board and pad array.

detector gain is above 10, a spark will be induced. For hadron beams, the maximum intrinsic electron multiplication is therefore limited to about 10.

6.9 Bandwidth Requirements

The ability to measure the beam timing features allows for new quality assurance techniques previously unavailable to most clinics. Section 2.5.1 explained that the beam timing features include the extraction rate of the proton beam (∼100 Hz), aliasing due to longitudinal beam oscillations (∼1 kHz), and the RF accelerating

cavity (∼MHz). Measuring the RF timing of the beam would add little to benefit the treatment, therefore a bandwidth of 10 kHz is chosen, which is adequate to measure the most important beam timing features, the spot extraction and individual spot features. 10 kHz is also high enough to allow for some generality in the accelerator types where this detector could be used.

6.10 Spatial Resolution vs Centroid Resolution

In PBS, the proton beam is often modeled as having a 2D Gaussian profile. When the profile is measured, the mean and sigma are extracted. The uncertainty in the mean is the centroid resolution, which is typically much lower than the detector resolution, made possible by assuming a Gaussian profile. The centroid resolution is typically on the order of tens of microns, even for detectors with a pixel-pitch approaching 5 or more millimeters. To make use of this high resolution for the centroid position, the beam has to be in a fixed position for longer than the response time of the detector, which is really only possible in specific QA procedures. A detector with a high bandwidth can make use of the high centroid resolution on every spot, which can be measured during any QA procedure. For example in patient-specific QA, a typical detector is limited by its true spatial resolution, which may be very large on the order of a millimeter.

Chapter 7

DEVELOPMENT OF A MULTICOORDINATE IONIZATION CHAMBER AND MICROMEGAS

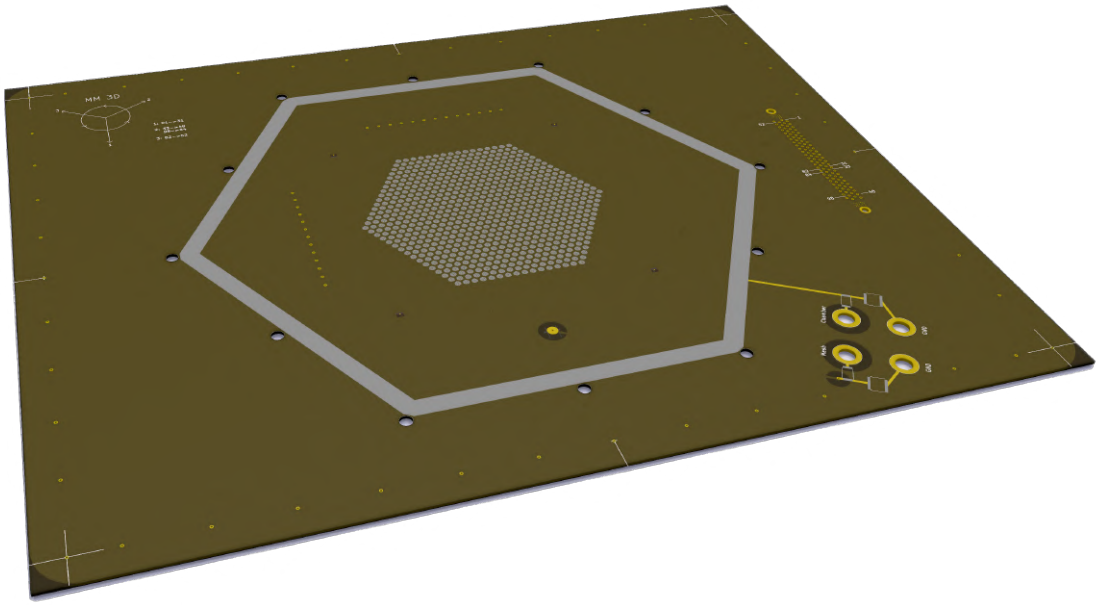

Figure 80: The board layout for the fluence detector. The active area is the pixelated region near the center.

The development of a multicoordinate ionization chamber and specifically a Micromegas detector was initially seeded by the Kemper Marley Foundation through Mayo Clinic. Further work has since been funded by the Department of Energy, Office of Nuclear Physics through the STTR program as a joint collaboration between Arizona State University and Radiation Detection and Imaging, LLC (RDI LLC).

The ultimate goal of the detector is to image the proton beam at a frame rate of 25 kHz while providing a high dynamic range and spatial resolution within 1 mm.

There are many possible configurations for building such a detector, but the primary limitation of any detector is the maximum data throughput. The maximum data throughput is typically set by high bandwidth computer communication protocols, however it is assumed that detectors of different configurations would have the same maximum limitation.

The detector data throughput is proportional to the number of measurements per second. As an example, a camera may use a CMOS or CCD sensor with millions of pixels. For a 60 Hz frame rate, the pixels are readout sequentially such that it takes about $\frac{1}{60}$ seconds to readout all the pixels. The number of measurements per second for a 1 megapixel camera with a 60 Hz frame rate is then 60 million measurements per second. If each measurement requires 16-bits of data storage, then the data throughput for such a camera is

$$(1,000,000 \text{ channels})(60 \text{ Hz})(16 \text{ bits}) = 960 \text{ Mb/s} \ . \tag{7.1}$$

The data throughput can be generalized to

$$T = N * f * d \ , \tag{7.2}$$

where T is the data throughput, N is the number of channels, f is the frame rate, and d is the number of bits of each channel measurement. The limitation due to the maximum data throughput is then $T_{max} > N * f * d$. For the sake of demonstration, this limitation does not take into account lossless data compression.

In choosing a detector configuration for proton therapy fluence measurements, we would like to have time sensitivity for measuring individual spot information. Because most of the information about the spots is within 10 kHz bandwidth, a 25 kHz frame rate is chosen. To ensure a large dynamic range, the bit resolution is

18-bits. Therefore, if we limit the data throughput to 1 Gb/s (Gigabit Ethernet GbE), the maximum number of channels is 2,222.

If the detector were chosen to be a pixelated design, we could in theory use a 47 x 47 array ($\sqrt{(2222)} = 47$). For a 40 cm x 40 cm detector, each pixel would be almost 1 cm x 1 cm, which is too large to adequately image a pencil-beam scanning proton therapy beam on a spot by spot basis. A common approach in contrast to pixelation is to have a strip readout. In a typical proton therapy QA scenario, the most important information being pulled from the detector is the position, sigma (assuming it is a 2D Gaussian), and dose. The strip readout approach loses some ability to measure arbitrary features, but improves the ability to measure the simpler desired features due to the added granularity in each dimension. In a 2D strip readout as shown in Figure 81a, very fine information can be pulled from the x and y dimensions, however the dimensions are orthogonal, which limits the ability to image. Adding more dimensions allows for the ability to image more complex shapes [14], albeit with less granularity for each added dimension. In this project, the detector measures the beam along 3 dimensions as demonstrated in Figure 81b. By using 3 dimensions, we retain the ability to do imaging while also having a fine granularity for measuring the beam shape.

7.1 Pad Geometry

Each dimension of the 3D readout must have physical access to the chamber. The 3D readout concept can be conveniently coupled to the chamber volume while also filling the planar area as demonstrated by Figure 82. While pad geometry is defined by 4 parameters, the channel pitch within a dimension, p, the gap between neighboring

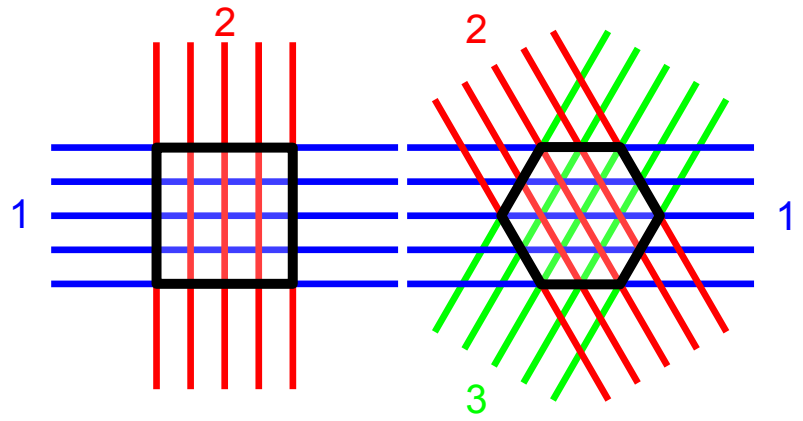

(a) 2D (b) 3D

Figure 81: Strip layout patterns. A common choice is to lay the strips in 2 dimensions (x and y) where the overlap forms a square. The 3D concept is illustrated where the overlap forms a hexagon.

clusters, g_1, the gap between neighboring pads within a cluster, g_2, and the corner radii, φ. For added clarity, the pad geometry parameters are defined visually in Figure 83. The actual pad parameter values chosen for the prototype fluence detector presented in this work are $p = 2.77$ mm, $g_1 = 0.9$ mm, $g_2 = 0.1$ mm, and $\varphi = 0.05$ mm.

The macroscopic shape of the pad array could be chosen as a square, circle, etc., however a hexagon is the shape which gives the closest pad area per channel, which is effectively the capacitance of the detector channel. For this reason, a hexagon defines the outer shape of the 3D readout array. The side-length of the hexagon is about 48 mm. The largest square which can fit within the hexagon boundary has a side-length of about 61 mm. The overall printed circuit board layout is shown in Figure 80.

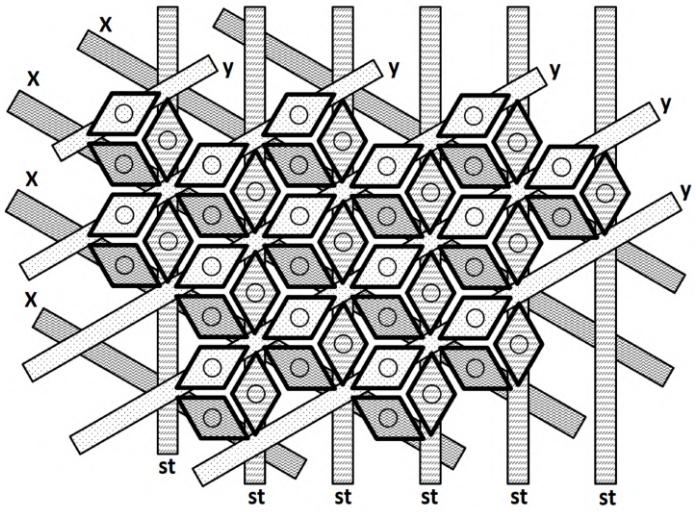

Figure 82: The pad layout concept. The hexagon cells are connected such that there are 3 dimensions being measured in a two-dimensional plane which fills the planar area. Each pad is connected to the printed circuit board traces through a via. Patented by RDI LLC [16].

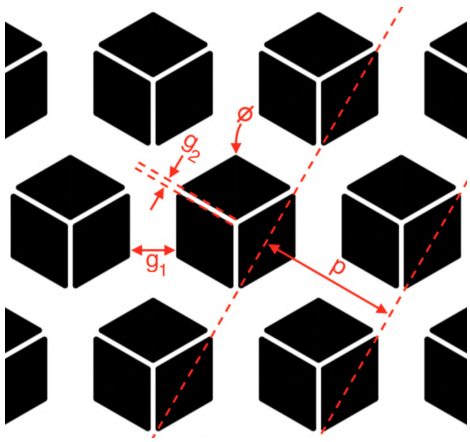

Figure 83: The parameters defining the pad structure for the 3D readout concept.

7.2 Building the Micromegas

As of today, a vast majority of Micromegas detectors are built by a collaboration between CERN (European Organization for Nuclear Research) and CEA Saclay (Saclay

Nuclear Research Centre) using the so called bulk Micromegas [17] and microbulk Micromegas [4] techniques. CERN and CEA Saclay have had the philosophy of developing new processes in order to build the Micromegas detectors. The philosophy for this project has been to make use of existing, albeit continually improving/evolving, industrial processes.

The most difficult and fundamental aspect of building a Micromegas is placing the mesh at a well defined height above the readout pads. To enforce the mesh height, we place a "spacer" between the anode cells, which is demonstrated by Figure 84. Our material approach is to use readily available manufacturing processes, especially relying on the printed circuit board industry. For example, the pad array is made from a custom printed circuit board made from a polyimide or FR-4 substrate and the mesh spacer is adapted from existing printed circuit board stencil technology, made from polyimide. Using our build procedure, we can regularly produce mesh assemblies held flat to within 2 microns as measured by a Keyence 3D microscope. The mesh assembly is built freestanding from the detector and is then glued onto the spacer as pictured in Figure 85.

7.3 Micromegas Mesh Electron Transparency

The ideal multiplication region boundary has been described by [24] to be perfectly transparent to electrons, totally opaque for ions, allowing for gas to dilute equally in all regions, and to be infinitely thin and flat. The mesh electron transparency is defined as the ratio of electrons which pass through the mesh over the electrons which approach the mesh. The electron transparency is largely dependent on the optical

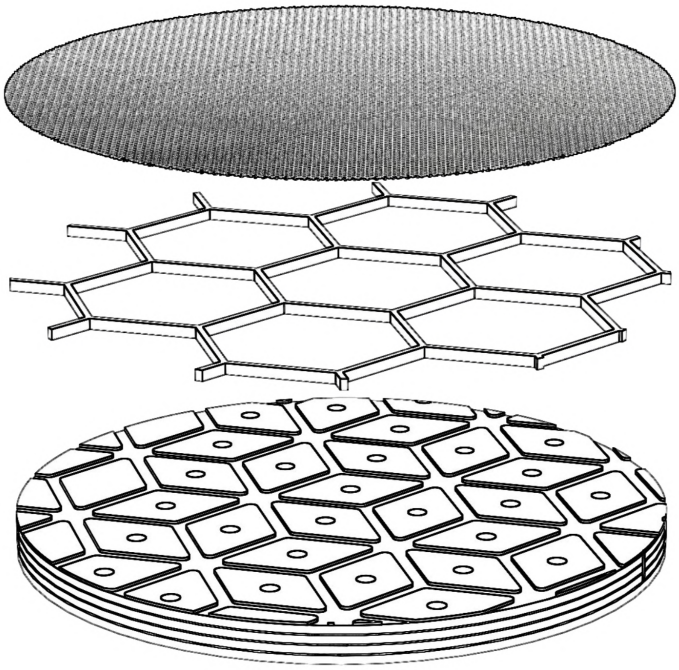

Figure 84: The placement of a mesh over the anodes uses a spacer which conforms to the pad structure. The spacer enforces a height of the mesh above the anodes.

transparency and the ratio of the drift field to the multiplication field. The optical transparency, τ, is defined as

$$\tau = \frac{(p-d)^2}{p^2} \ , \tag{7.3}$$

where p is the mesh opening pitch and d is the diameter of the wire. The geometric mesh parameters are shown in Figure 86.

In a study performed by Kuger et al. [24], they found that the electron transparency was only slightly dependent on the particular geometric parameters, but very dependent on the optical transparency. Two different mesh configurations with different pitch and wire diameter generally perform similarly as long as the optical transparency was the same. Based on their study, they chose to use a woven mesh with a geometry of 71 μm aperture and 30 μm wire diameter. We were able to reproduce similar results. The

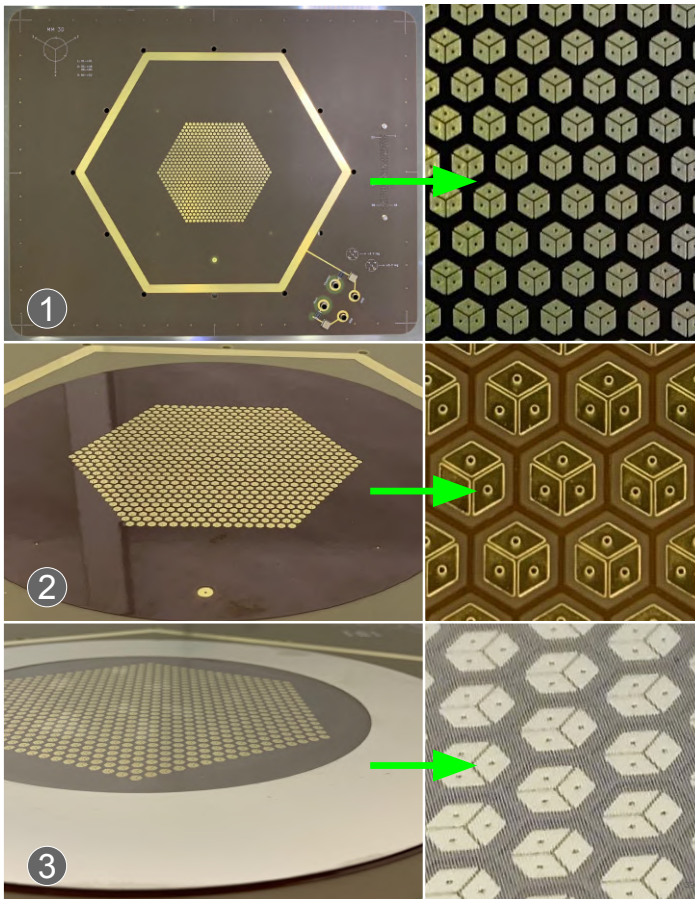

Figure 85: The process for adding a micromesh to the detector. (1) design the pcb to have gaps between the pixels, (2) place the kapton spacer onto the pcb. (3) place the mesh assembly onto the kapton spacer thus forming the multiplication region.

electron transparency of the woven mesh was simulated in Garfield++. A 120 MeV proton is shot through the detector and the ionization electrons are tracked throughout the chamber. Figure 87 shows how the electron transparency varies depending on the optical transparency of the mesh as the drift field is increased (multiplication field is constant). The electric fields were simulated using a finite element analysis software, OPERA [2], and then input into the Garfield++ simulation. The mesh geometry in the simulation is demonstrated by Figure 88. The mesh configuration chosen for this

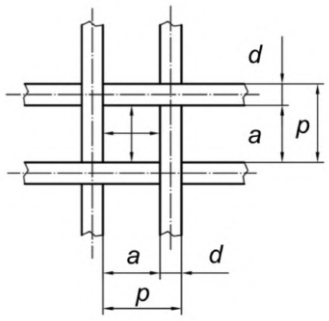

Figure 86: The geometric parameters defining a woven mesh. p is the mesh pitch, d is the wire diameter, and a is the aperture opening side-length. Image taken from Kuger et al. [24].

project based also on availability was 76 μm aperture side-length and 22 μm wire diameter, which gives an optical transparency of 60%.

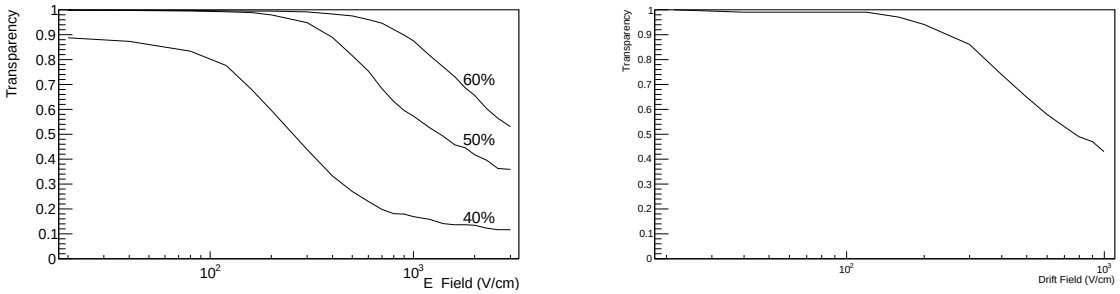

(a) Simulated in Garfield++

(b) Measurement

Figure 87: In the simulated results, electric fields modeled in OPERA were input into Garfield++ and the electron transparency was calculated for mesh having optical transparencies of 40%, 50%, and 60%. The higher the optical transparency, the higher the electron transparency extends for higher drift fields. The detector electron transparency was also measured for a mesh with 60% transparency and 100% charge collection is seen for moderate electric fields.

As a means of benchmarking the Garfield++ simulation, the electron transparency

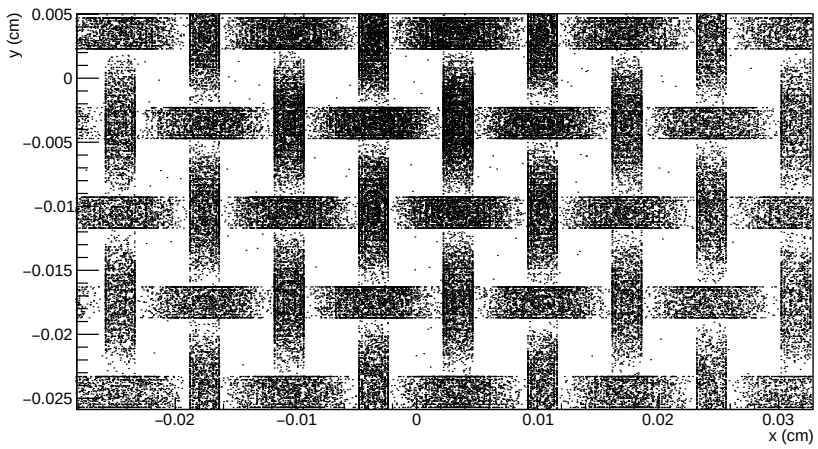

Figure 88: In a configuration with poor electron efficiency, the electron endpoints for electrons which do not reach the anodes are plotted, which gives a good sense of the woven mesh geometry used in the simulation.

was measured. Within the Micromegas chamber, a freestanding cathode is inserted and placed at a height of 5 mm. The freestanding cathode has a 1/8" hole drilled through for collimating a Po-210 alpha source. The setup is shown in Figure 89. The freestanding cathode is electrically connected to the chamber and the chamber is filled with P–10 gas. A pulse height distribution was obtained for each drift field strength using an Ortec 142A preamp and an Amptek 8000D multi-channel analyzer. The most probable pulse height was extracted for each drift field and is plotted in Figure 87. As compared with the Garfield++ simulation, the results show a similar shape in the electron transparency as the drift field increases, however the electron transparency begins to drops earlier. Further work will continue to resolve and explain the differences.

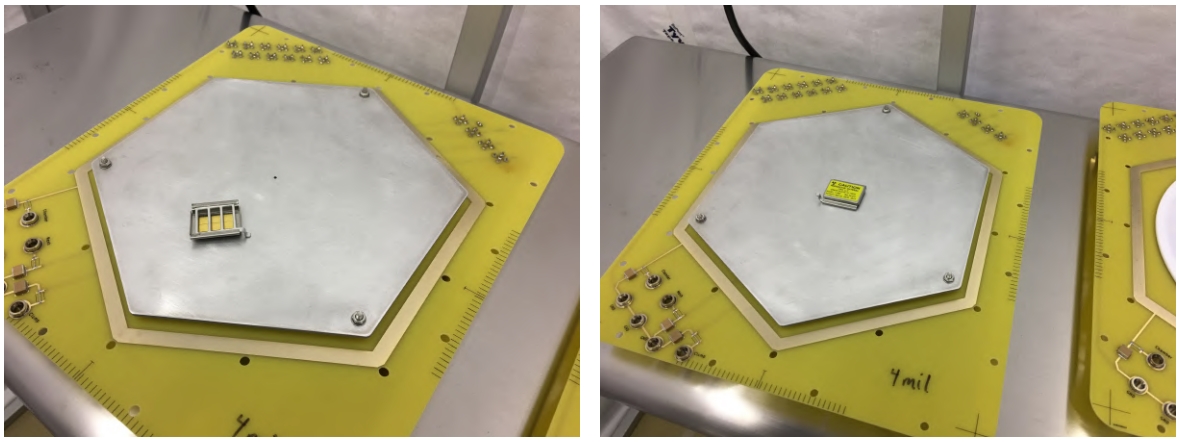

(a) opening for the Po-210 alpha-source (b) Po-210 alpha-source in position

Figure 89: The setup for measuring the electron transparency of the Micromegas detector.

7.4 Sparking

Through visual inspection of the Micromegas while applying a high voltage to the mesh, it was apparent that sparking occurred at the junction where the spacer touches the mesh. Also, sparking did not seem to occur between the mesh and the pads. In order to gain a better understanding of sparking, the electric fields were simulated using OPERA. The simulation verified that the highest electric field strength is near to the corner at the gas/spacer/mesh junction, which can be seen in Figure 90. This type of junction is called a triple-junction [36] and is known to have an enhanced electric field strength. Imagining a cross section of the cell area, Figure 91 shows the field strength along a line passing just below the mesh for two different mesh heights. The peak location is at the spacer edge. The plateau is above the pad.

When operating the Micromegas, the bias is set at a point below where sparking begins to occur. The spike in the electric field strength due to the triple-junction

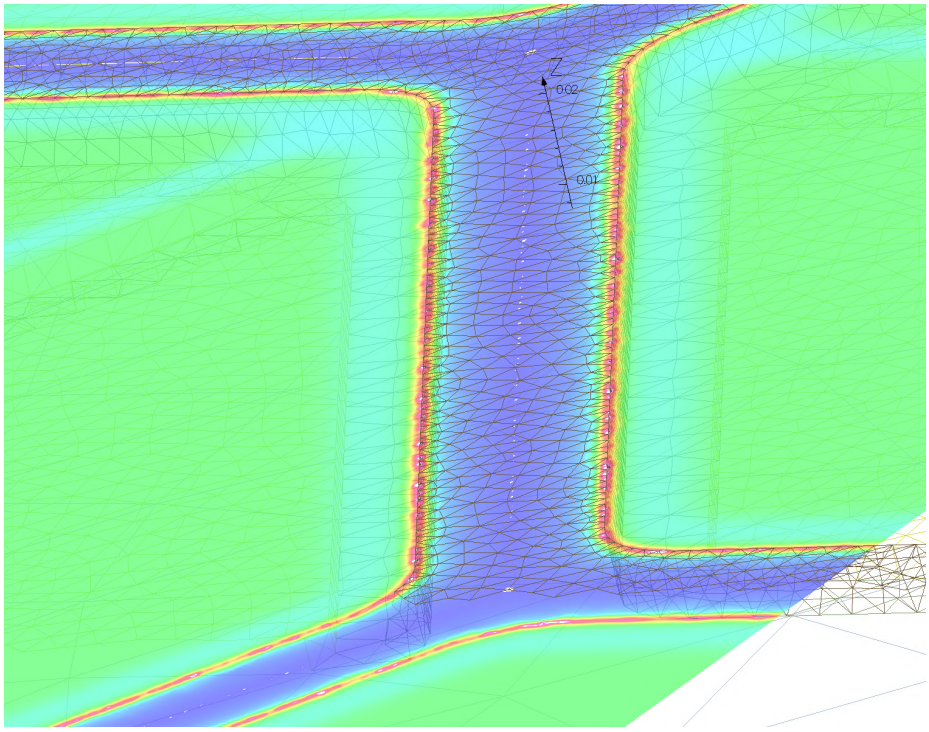

Figure 90: The electric field magnitude in the plane just below the mesh. The green color above the pads is the expected field strength found by taking the mesh potential divided by the mesh height. Near the spacer edge, the triple-junction where the gas/spacer/mesh all meet, the field strength is enhanced well above the field strength above the pads. This enhanced region is where breakdown is most likely to occur.

must be below the breakdown field, effectively limiting the multiplication range of the Micromegas. Using OPERA and varying the gap size between the spacer edge and the pad edge and also varying the mesh height, the ratio of the peak electric field strength to the plateau field strength was calculated. Figure 92 illustrates the results. The ratio can be minimized by reducing the mesh height. As the ratio approaches 1, the full range of multiplication can be utilized, no longer limited by the triple-junction effect. The geometric properties studied here give promising results for suppressing the sparking in a Micromegas.

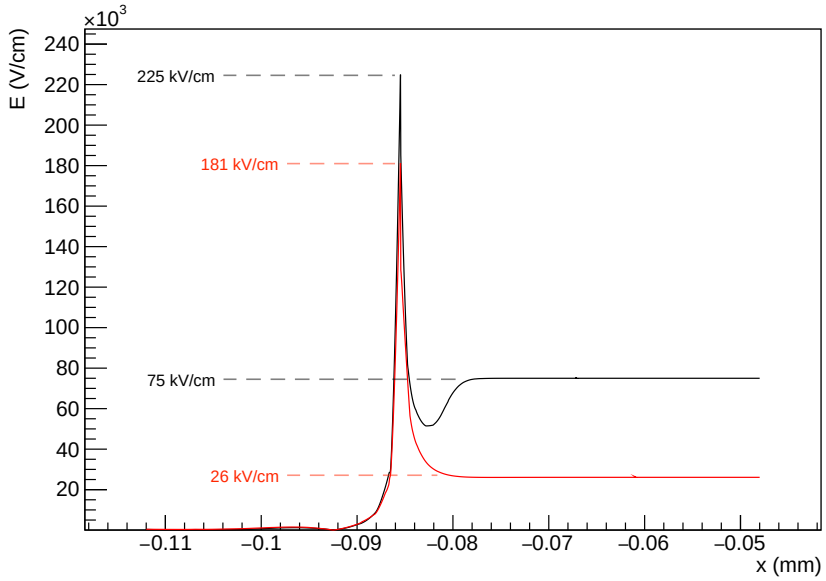

Figure 91: The electric field strength along a line passing just below the mesh and across the pad into the polyimide (dielectric) spacer. The black curve is for a mesh height of 150 μm. The red curve is for a mesh height of 75 μm. The sharp peaks correspond with the triple-junction between the dielectric, the gas, and the mesh.

7.5 Data Acquisition Electronics

A 96 channel data acquisition (DAQ) system was designed and constructed for use with the proton beam fluence detector. The DAQ concept is outlined in Figure 93. The data acquisition system measures the ionization current collected by the detector pads, digitizes the information, and writes the data to computer memory. The current is captured at a 25 kHz frame rate using 18 bit digitization. The 96 channels are digitized by 12 ADCs integrated circuits followed by a parallel readout of the digitized data by the Terasic DE0-Nano-SoC (Altera Cyclone V FPGA System on a Chip). The motivation for the transimpedance (gain) and the noise characteristics are given in this section.

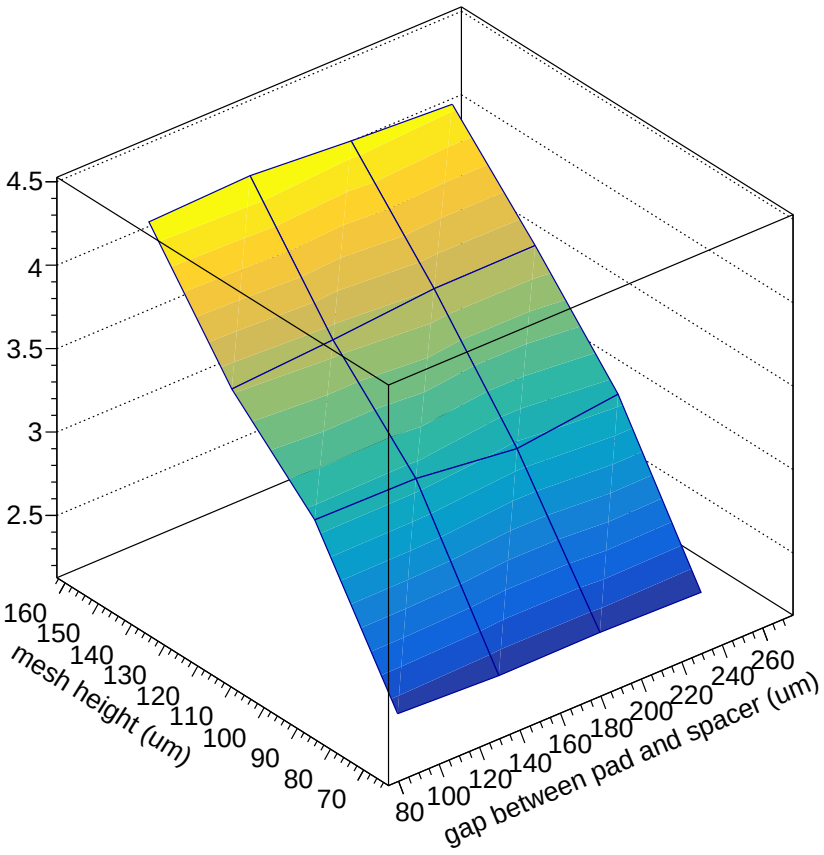

Figure 92: The Ratio of the peak electric field strength divided by the plateau electric field strength. The ratio has a strong dependence on the mesh height and very little dependence on the gap between the spacer and the pad.

7.5.1 Choosing an Adequate Transimpedance

The ionization current is converted to a voltage using a transimpedance amplifier. Figure 94 shows the circuit diagram for a transimpedance amplifier. The output voltage can be calculated given an input current,

$$V_{OUT} = I_{IN} R \ , \tag{7.4}$$

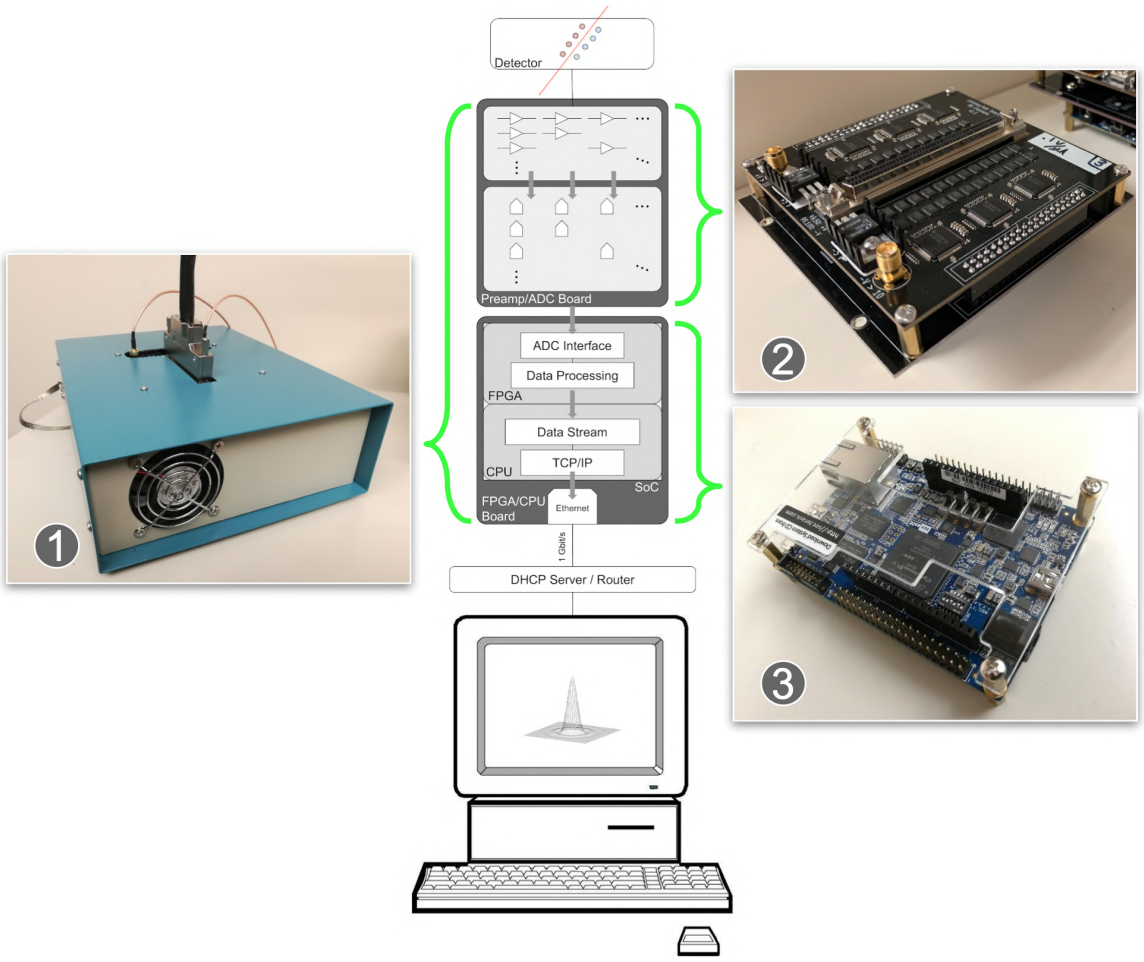

Figure 93: The data acquisition concept. In image 1, a simple enclosure was made for containing and cooling the data acquisition components and allowing for a cable connection from the detector to the data acquisition system. Image 2 shows the analog front end and digitization device, which is mainly composed of 96 transimpedance amplifiers followed by 12 ADC integrated circuits. Image 3 shows the Terasic DE0-Nano-SoC (Altera Cyclone V FPGA System on chip).

where R is the feedback resistor of the opamp. The transimpedance (sometimes just called gain) is equal to R and the bandwidth is 0 to $\frac{1}{2\pi RC}$. To determine a suitable transimpedance value for the DAQ, first the maximum signal strength for a single channel must be estimated. If the detector consists of a strip readout, Figure 95 gives the fraction of the total ionization for a strip centered on a Gaussian beam. For

sigmas ranging between 0.5 cm and 2.0 cm, the fraction is seen to be between about 5% and 20% of the total beam. For a detector active area segmented by strips in 3 dimensions as is the case, the fraction for a single strip should be divided by 3, so the range in signal depending on the beam shape is between 1.5% to 7%. Assuming a 1 cm drift region, the total current is about 0.8 μA for a 71.3 MeV proton beam. For a 2 mm to 3 mm strip centered on a 0.5 sigma Gaussian beam with a flux of 10 GHz, the maximum signal for a single channel is approximated to be about 7% of 0.8 μA or about 60 nA.

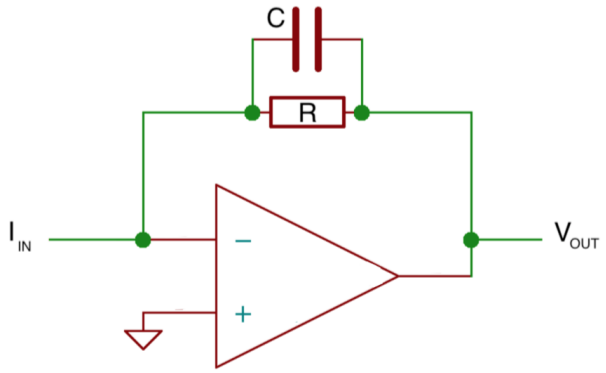

Figure 94: The circuit diagram of a generic transimpedance amplifier.

The real beam has features that spike above the mean when using a fast gas such as P-10, so we should allow for features that are 4 times larger than the mean. Also, to allow for higher intensity without adjusting the gain, another factor of 10 is included. So, the transimpedance which fits these requirements is calculated to be about 2 MΩ or 2 V/μA. If using air instead of P-10, the gain may safely be doubled since the spikes will be smaller by at least a factor of 2.

In the case of a Micromegas, assuming an electron multiplication of 100, the gain will be 20 kΩ or .02V/μA.

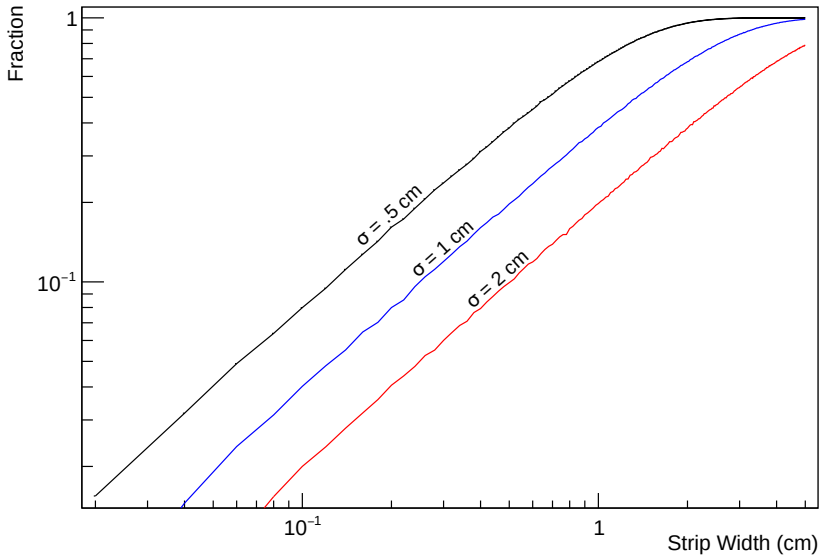

Figure 95: The fraction of a Gaussian profile beam intersecting a strip centered on the beam for various beam widths.

For the first DAQ module which was constructed and for which the beam testing was performed, the transimpedance value chosen was .1V/μA. The value was chosen initially assuming a different detector geometry and an electron multiplication of about 100.

7.5.2 Noise and Offsets

The noise and offsets for the DAQ was measured. Figure 96 shows the distribution of offsets for the 96 channel DAQ system. The offsets are very reasonably displaced around zero. The offsets are recalculated and subtracted for each measured current to ensure a correct measurement. The RMS noise over a 100 ms period at 10 kHz bandwidth for a typical channel was measured to be 1.1 nA, which is about 3 least

significant bits for the ADC. In this configuration, the maximum signal to noise ratio is $20 \log(\frac{50\ \mu\text{A}}{1.1\ \text{nA}}) = 93$ dB.

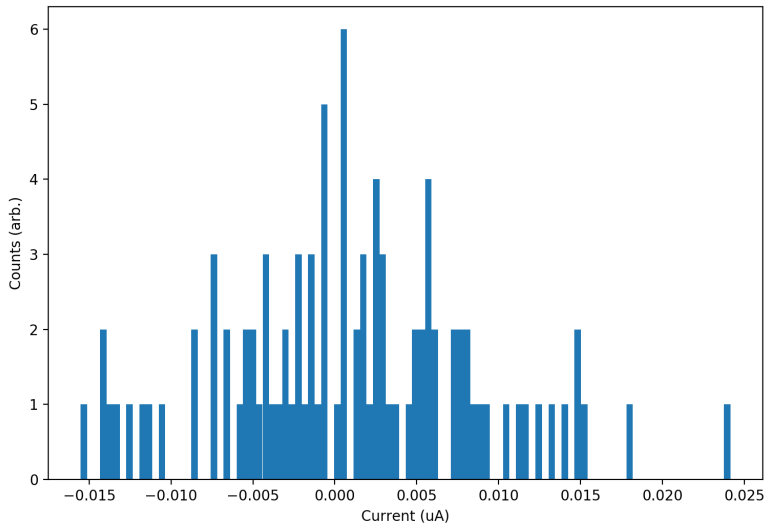

Figure 96: Offsets histogram of the 96 channels of data acquisition.

Chapter 8

FLUENCE DETECTOR PROTON BEAM RESULTS

The fluence detector was tested at the Proton Therapy Center at Mayo Clinic in Phoenix, Arizona and also at Mayo Clinic in Scottsdale, Arizona. The detector was tested in 3 configurations: (1) A gridded ionization detector (Micromegas) with P-10 gas and a 0.8 cm deep chamber, (2) An ionization chamber with P-10 gas and a 1.8 cm deep chamber, and (3) an ionization chamber with air and a 1.8 cm deep chamber. The pad layout and DAQ were identical in all configurations. The chamber window is aluminum and 0.8 mm thick.

The detector anode plane and the center of the detector were placed at beam isocenter as can be seen in Figure 97. The results for three different proton beam plans are presented in this chapter. The beam plans are listed in Table 4.

8.1 Ionization Current

The total ionization current for the detector can be found by summing all 96 channels of the detector. The ionization current for a single 151.9 MeV, 0.1 MU spot is shown in Figures 98a and 98b. The beam timing features are less pronounced in air due to the differences in the diffusion of secondary ionization. Because air requires a higher average energy to create an electron-ion pair than P-10, the ionization current in air is smaller than P-10. For 100 spots (Plan "Single" in Table 4), the ratio of the total charge deposited into the chamber for air to P-10 was measured to be 0.61,

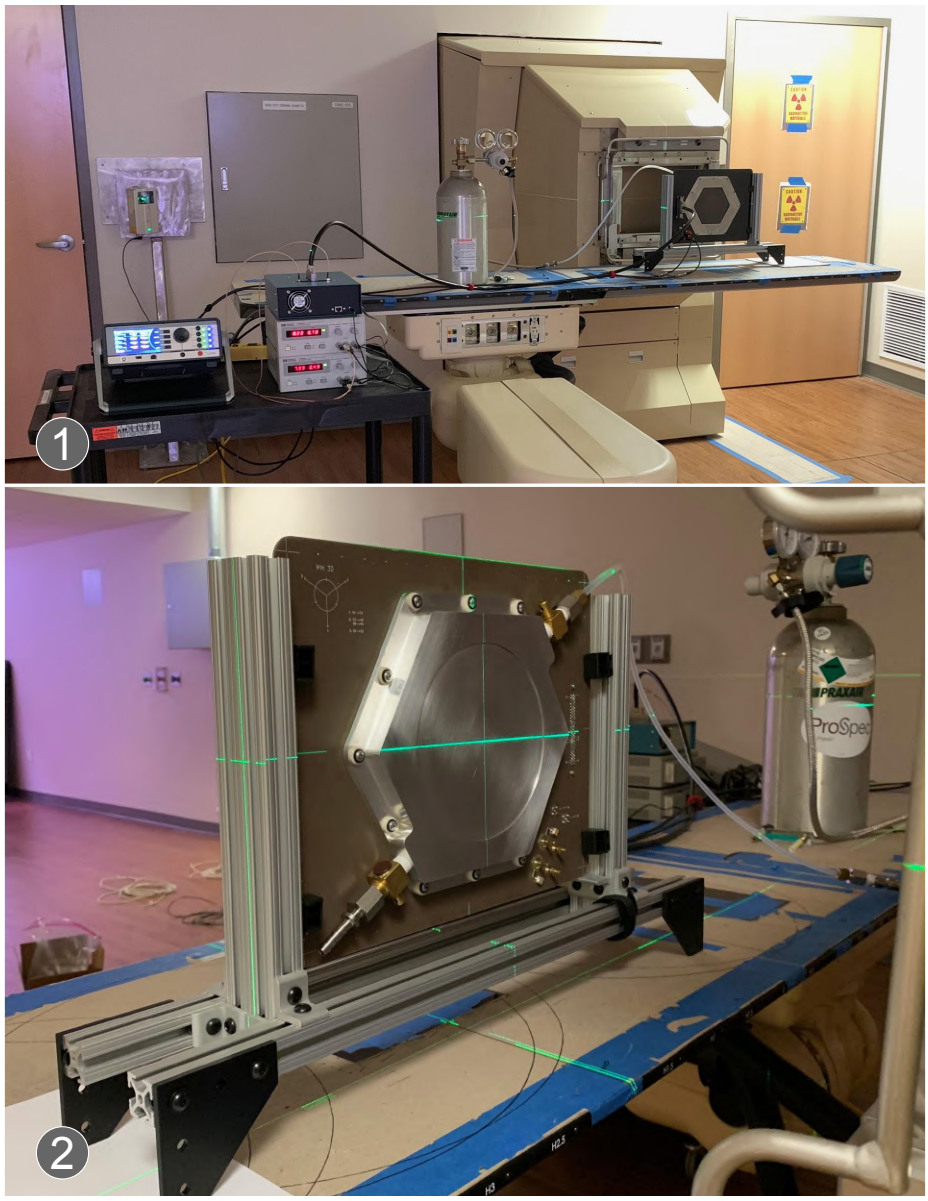

Figure 97: The fluence detector setup at the fixed-beam room at Mayo Clinic in Phoenix, AZ

which is smaller than the ratio of the average energy required to create an electron-ion pair, which is $\frac{26 \text{ eV}}{34.2 \text{ eV}} = 0.76$. This discrepancy may be due to P-10 gas not being pure Argon or that there was air contamination in the P-10 gas, or a geometric factor that has not been considered.

Plan	Energy (MeV)	protons/spot	MU/spot	spots	x (cm)	y (cm)	Meas.
Single	151.9	71434640	0.1	100	0.0	0.0	1
Linearity	71.3	1216040	0.003	100	0.0	0.0	1
	71.3	4053466	0.01	100	0.0	0.0	2
	71.3	12160400	0.03	100	0.0	0.0	3
	71.3	20267333	0.05	100	0.0	0.0	4
	71.3	30401000	0.075	100	0.0	0.0	5
	71.3	40534667	0.1	100	0.0	0.0	6
	71.3	60802001	0.15	100	0.0	0.0	7
	71.3	81069335	0.2	100	0.0	0.0	8
	71.3	101336669	0.25	100	0.0	0.0	9
	71.3	121604003	0.3	100	0.0	0.0	10
Energy	71.3	40534667	0.1	100	0.0	0.0	1
	88.5	48203396	0.1	100	0.0	0.0	2
	103.6	54397548	0.1	100	0.0	0.0	3
	117.1	59552496	0.1	100	0.0	0.0	4
	129.7	64070807	0.1	100	0.0	0.0	5
	141.4	68039379	0.1	100	0.0	0.0	6
	151.9	71434640	0.1	100	0.0	0.0	7
	163.5	75023917	0.1	100	0.0	0.0	8
	173.6	78028097	0.1	100	0.0	0.0	9
	183.3	80822046	0.1	100	0.0	0.0	10
	193.6	83706102	0.1	100	0.0	0.0	11
	203.1	86304197	0.1	100	0.0	0.0	12
	209.7	88081050	0.1	100	0.0	0.0	13
	218.7	90475469	0.1	100	0.0	0.0	14
	228.8	93135419	0.1	100	0.0	0.0	15

Table 4: Fluence detector beam test plans used in the fixed-beam room at Mayo Clinic in Arizona. The number of protons per spot is an estimate. The amount of MU per spot was used directly in controlling the beam.

The Fourier transform of the current versus time for about 100 spots (151.9 MeV proton beam, 0.1 MU per spot) yields the frequency structure of the beam. The ∼100 Hz beam timing and the faster ∼1 kHz structure are both visible as shown in Figure 99.

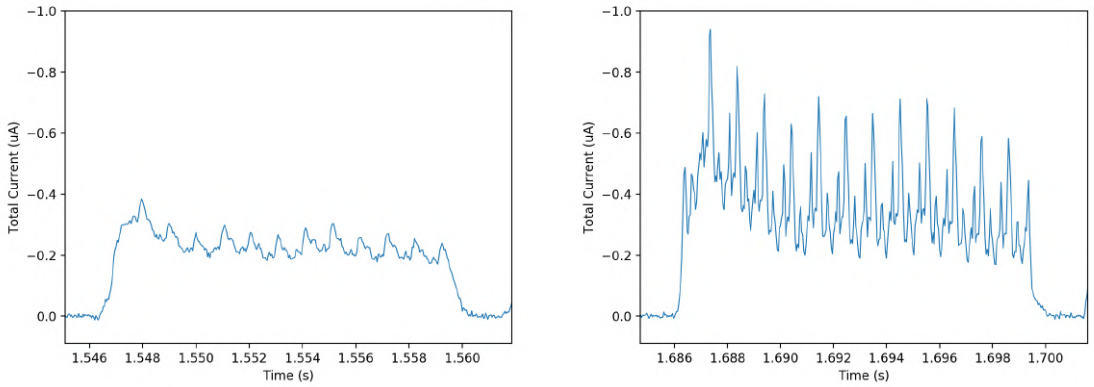

(a) Air (b) P-10

Figure 98: A single proton therapy beam spot in air and P-10 gas for a beam energy of 151.9 MeV and 0.1 MU per spot.

8.2 Linearity in Time

The linearity response of the device was measured as the amount of MU per spot was varied for a fixed beam energy (Plan "Linearity" in Table 4). The energy deposit in the detector for a fixed beam energy is proportional to the amount of MU. As the amount of MU increases, the time duration of spots increases. A linear response of the detector indicates that the detector is stable over time. Figure 100a shows the linearity in air, which is expected to be linear. Figure 100b shows that the Micromegas is linear, but perhaps not quite as linear as the air-based detector. Both detectors show a slight non-linearity at 0.75 MU/spot, which may indicate the beam delivering slightly more MU than requested.

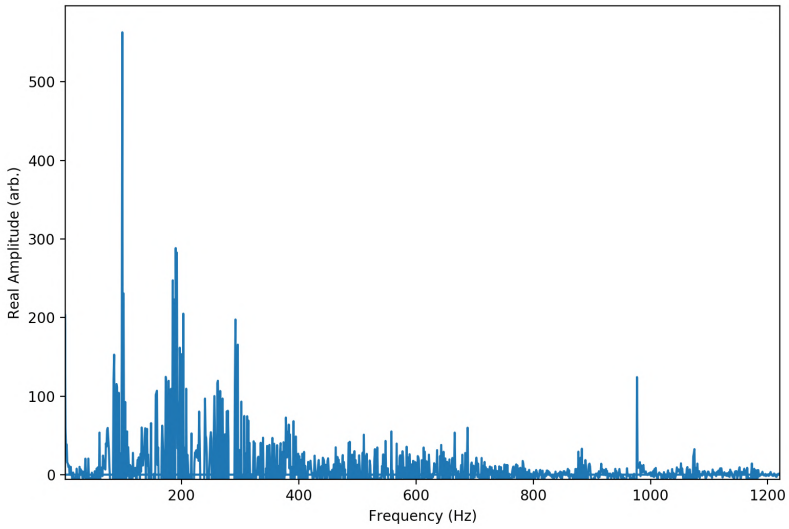

Figure 99: The signal amplitude versus frequency found by taking the fourier transform over about 2 seconds of ionization current data. The peak near 100 Hz is due to the spot period followed by harmonics at 200 Hz and 300 Hz. The peak near 1 kHz is due to the intraspot periodic timing, hypothesized to be aliasing of the longitudinal beam oscillations.

8.3 Beam Profile

The beam profiles were measured for various proton beam energies, using the "Energy" plan shown in Table 4. Because the chamber is 1.8 cm thick, a large amount of diffusion is expected for the electrons and ions in the chamber. For each energy, the 3 detector projections were fit to a Gaussian respectively. Figure 101a shows the 71.3 MeV beam profile taken for a single spot, where the precision in sigma and the position is about 90 microns. Figure 101a shows the 228.8 MeV beam profile taken for a single spot, where the precision in sigma and the position is about 40 microns. Beam profile measurements for a single spot have extremely good signal to noise

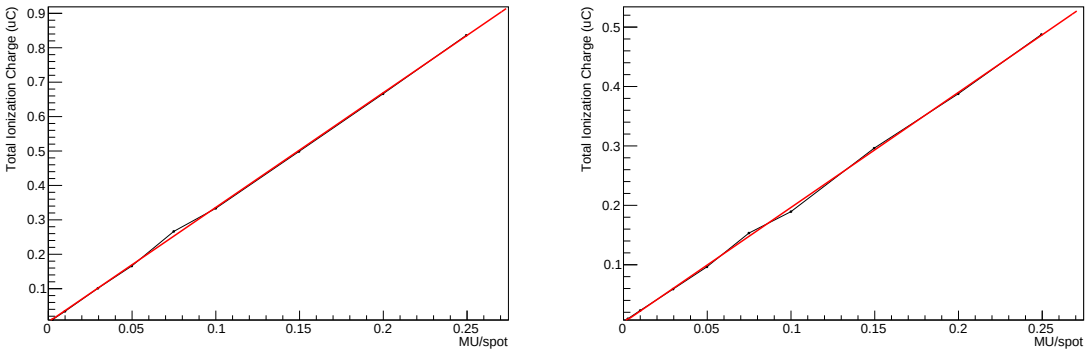

(a) Air (b) Micromegas (P-10)

Figure 100: The linearity of each detector response to increasing amounts of MU per spot.

characteristics. Even using just a few samples is possible, however the noise floor starts to become apparent.

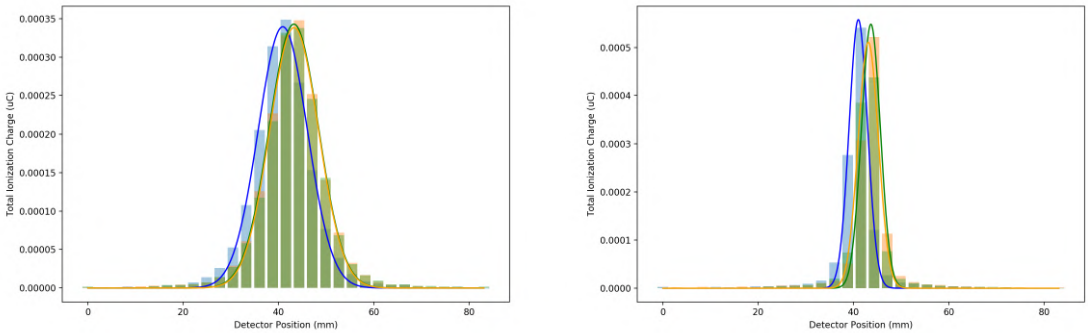

(a) 71.3 MeV (b) 228.8 MeV

Figure 101: The smallest beam energy and largest beam energy as measured in P-10, measured for a single spot of about 10 ms.

The sigma for each dimension was averaged and plotted in Figure 102. The results are as expected. The air detector shows a larger sigma over the entire energy range due to the higher diffusion of the electron and ions in air. For a detector which can

be used for clinical purposes, the chamber would need to be much thinner and the diffusion would need to be characterized and perhaps deconvolved from the beam profile.

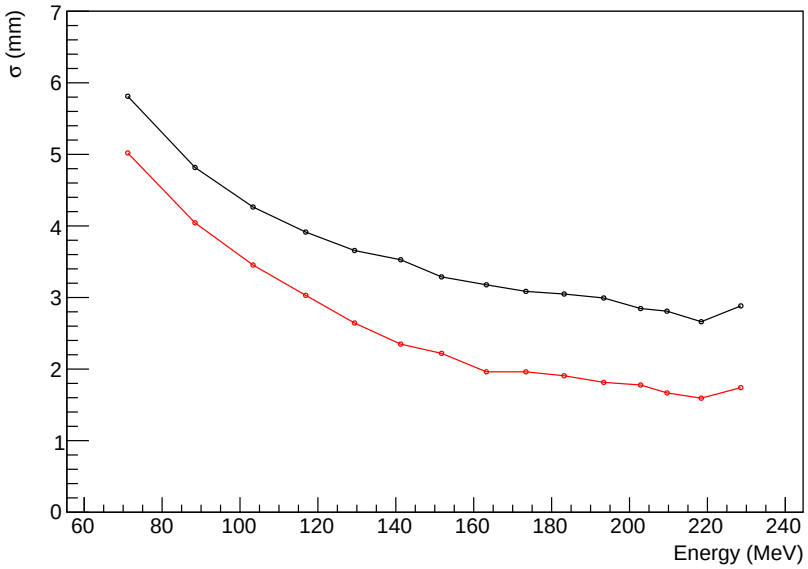

Figure 102: The measured sigma for each projection is averaged and plotted versus proton beam energy for both P-10 (red) and Air (black).

8.4 Electron Multiplication Measurement

Measuring the range of multiplication at the proton beam is not possible due to the Raether limit, however low values of gain are usable and have been demonstrated for a 151.9 MeV proton beam and shown in Figure 103a (multiplication of 2) and Figure 103b (multiplication of 20). The signal to noise ratio is clearly very high in Figure 103b, where the baseline noise is barely visible.

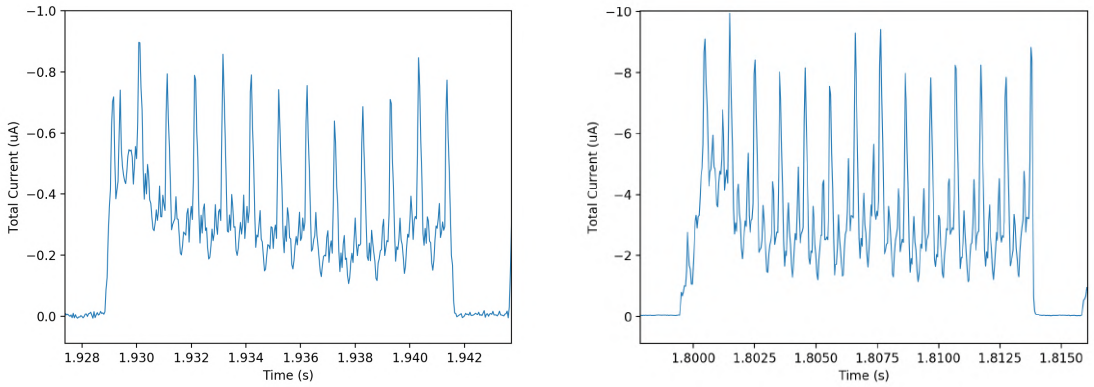

(a) Gain: 2

(b) Gain: 20

Figure 103: Single spots for the Micromegas detector, where intrinsic electron avalanche multiplication was implemented.

To measure the multiplication range of the Micromegas, the device was used in an IMRT system, the Varian EX2100 at the Mayo Clinic in Scottsdale, Arizona. This beam-line shoots gamma-rays which are collimated by a 120 leaf multi-leaf collimator (MLC). Nuclear processes are heavily suppressed as compared to protons, which effectively eliminates the possibility of the Raether limit being exceeded. The multiplication was measured and is shown in Figure 104a and Figure 104b. The maximum multiplication achieved before sparking began to occur was about 300. More extensive testing with different heights and mesh types will follow in future work. Because the Raether limit does not limit the Micromegas for x-rays or electrons, the Micromegas is now being considered for those modalities of treatment.

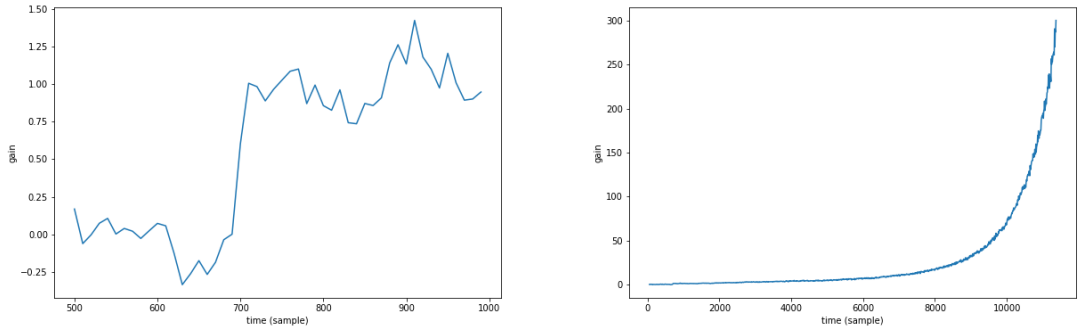

(a) Beam Turn-on (b) Gain vs. Time

Figure 104: The multiplication for a 65 micron mesh height above the pads. The mesh voltage was slowly increased while maintaining a constant drift field.

8.5 Exceeding the Raether Limit

When trying to operate the Micromegas in a proton beam, the gain must be set as to not allow the occasional nuclear collisions to cause the number of electrons within the multiplication region to exceed the Raether limit. This limits the multiplication factor that is possible in a beam (see Section 6.8. A typical example of sparking caused by exceeding the Raether limit is shown in Figure 105. The spark occurs very near to the time when the beam turns on.

8.6 Clinical Usage

The fast response of this detector does not preclude its use in any case where fluence detectors are used in typical quality assurance procedures, however the fast response does offer new possibilities. For each spot delivered by the proton beam, the beam can be completely described by 6 parameters: (1) shape, (2) position, (3)

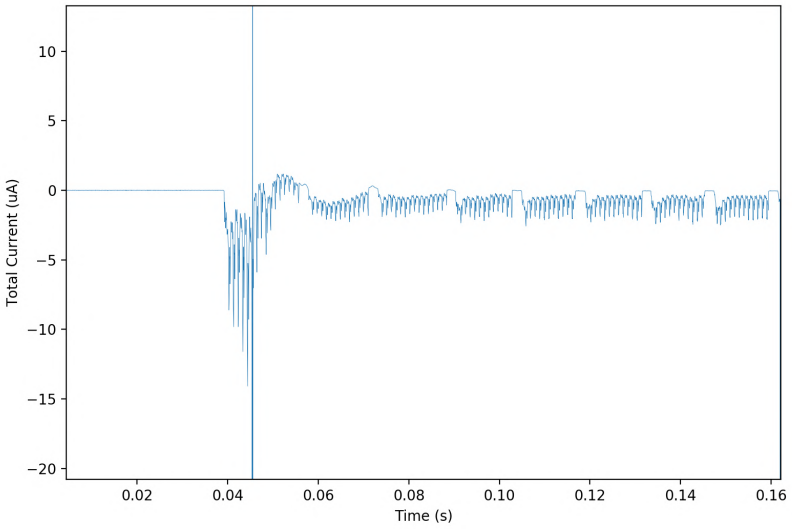

Figure 105: A typical example of sparking induced by the proton beam in a Micromegas.

energy, (4) angle, (5) current, and (6) duration. The detector as described can measure the shape, position, current, and duration on a spot by spot basis. Most available devices on the market only sample the overall dose delivered while offering no direct measurement of the beam spot parameters. As a result, proton therapy facilities are naturally becoming more reliant on beam monitor log files. By introducing a device which can directly measure the same parameters as the beam monitor on a spot by spot basis, a truly independent test of the beam monitor is possible.

Chapter 9

SUMMARY AND CONCLUSIONS

Proton therapy has the potential to be superior in most cases over other radiation therapy modalities, however due to protons stopping in the patient, there are natural complications. For one, the uncertainty in the range causes doctors to be cautious in treatment planning. Secondly, the ability to perform quality assurance is made more complicated. To accommodate for range uncertainty in patient-specific QA, the treatment plan has to be transformed into a water phantom plan and a fluence detector is scanned through a water tank. Although pencil-beam scanning has been transformational for proton therapy in the way the beam is delivered, a similar advancement in detection technology has not occurred. The fluence detectors available on the market do not measure the beam spot by spot and are mostly too coarse to precisely image the beam due to having a pixelated readout.

The detectors presented in this work are a first step in helping the advancement of detectors used in proton therapy to catch up with the advancement in delivery. The range detector is able to measure the range up to 11 cm deep and to within 1.1 mm precision in less than 500 ms. The fluence detector can measure the beam shape and position on a spot by spot basis and well within reasonable resolution requirements of proton therapy. With simple upgrades, the fluence detector can have almost no dead volume, offering a continuous measurement area. Although only a brief description of new quality assurance techniques offered by these devices has been given, devices with these capabilities will surely offer a new perspective on quality assurance as they become available.

It is my hope that continued work on these projects will evolve into a better form of proton therapy ultimately leading to improved outcomes for patients.

BIBLIOGRAPHY

[1] Eclipse™ for Proton.

[2] Opera FEA Simulation Software, September 2013.

[3] S. Agostinelli, J. Allison, K. Amako, J. Apostolakis, H. Araujo, P. Arce, M. Asai, D. Axen, S. Banerjee, G. Barrand, F. Behner, L. Bellagamba, J. Boudreau, L. Broglia, A. Brunengo, H. Burkhardt, S. Chauvie, J. Chuma, R. Chytracek, G. Cooperman, G. Cosmo, P. Degtyarenko, A. Dell'Acqua, G. Depaola, D. Dietrich, R. Enami, A. Feliciello, C. Ferguson, H. Fesefeldt, G. Folger, F. Foppiano, A. Forti, S. Garelli, S. Giani, R. Giannitrapani, D. Gibin, J. J. Gómez Cadenas, I. González, G. Gracia Abril, G. Greeniaus, W. Greiner, V. Grichine, A. Grossheim, S. Guatelli, P. Gumplinger, R. Hamatsu, K. Hashimoto, H. Hasui, A. Heikkinen, A. Howard, V. Ivanchenko, A. Johnson, F. W. Jones, J. Kallenbach, N. Kanaya, M. Kawabata, Y. Kawabata, M. Kawaguti, S. Kelner, P. Kent, A. Kimura, T. Kodama, R. Kokoulin, M. Kossov, H. Kurashige, E. Lamanna, T. Lampén, V. Lara, V. Lefebure, F. Lei, M. Liendl, W. Lockman, F. Longo, S. Magni, M. Maire, E. Medernach, K. Minamimoto, P. Mora de Freitas, Y. Morita, K. Murakami, M. Nagamatu, R. Nartallo, P. Nieminen, T. Nishimura, K. Ohtsubo, M. Okamura, S. O'Neale, Y. Oohata, K. Paech, J. Perl, A. Pfeiffer, M. G. Pia, F. Ranjard, A. Rybin, S. Sadilov, E. Di Salvo, G. Santin, T. Sasaki, N. Savvas, Y. Sawada, S. Scherer, S. Sei, V. Sirotenko, D. Smith, N. Starkov, H. Stoecker, J. Sulkimo, M. Takahata, S. Tanaka, E. Tcherniaev, E. Safai Tehrani, M. Tropeano, P. Truscott, H. Uno, L. Urban, P. Urban, M. Verderi, A. Walkden, W. Wander, H. Weber, J. P. Wellisch, T. Wenaus, D. C. Williams, D. Wright, T. Yamada, H. Yoshida, and D. Zschiesche. Geant a simulation toolkit. *Nuclear Instruments and Methods in Physics Research Section A: Accelerators, Spectrometers, Detectors and Associated Equipment*, 506(3):250–303, July 2003.

[4] S. Andriamonje, P. Colas, A. Gris, T. Dafni, J. Galan, I. Savvidis, A. Teixera, C. Guerrero Sanchez, F. J. Iguaz, J. Ruz, F. Gunsing, D. Attie, E. Berthoumieux, R. De Oliveira, I. Giomataris, A. Giganon, G. Fanourakis, T. Papaevangelou, E. Ferrer-Ribas, A. Tomas, I. Irastorza, M. Calviani, and T. Geralis. Development and performance of Microbulk Micromegas detectors, 2010.

[5] Søren M. Bentzen, Louis S. Constine, Joseph O. Deasy, Avi Eisbruch, Andrew Jackson, Lawrence B. Marks, Randall K. Ten Haken, and Ellen D. Yorke. Quantitative Analyses of Normal Tissue Effects in the Clinic (QUANTEC): an introduction to the scientific issues. *Int. J. Radiat. Oncol. Biol. Phys.*, 76(3 Suppl):S3–9, March 2010.

[6] M.J. Berger, J.S. Coursey, M.A. Zucker, and J. Chang. ESTAR, PSTAR, and ASTAR: Computer Programs for Calculating Stopping-Power and Range Tables for Electrons, Protons, and Helium Ions (version 1.2.3), 2005.

[7] H. A. Bethe. Theory of the Passage of Fast Corpuscular Rays Through Matter. *Annalen der Physik*, 5:325–400, 1930.

[8] Aleksandra K. Biegun, Enrica Seravalli, Patrícia Cambraia Lopes, Ilaria Rinaldi, Marco Pinto, David C. Oxley, Peter Dendooven, Frank Verhaegen, Katia Parodi, Paulo Crespo, and Dennis R. Schaart. Time-of-flight neutron rejection to improve prompt gamma imaging for proton range verification: a simulation study. *Phys. Med. Biol.*, 57(20):6429, 2012.

[9] W. Binks. Energy per Ion Pair. *Acta Radiologica*, os-42(117_suppl):85–104, November 1954.

[10] D. Blyth, M. Gibson, D. Mcfarland, and J. R. Comfort. Flash ADC data processing with correlation coefficients. *Nuclear Instruments and Methods in Physics Research Section A: Accelerators, Spectrometers, Detectors and Associated Equipment*, 738:106–110, February 2014.

[11] Niels Bohr. I. On the constitution of atoms and molecules. *Philosophical Magazine Series 6*, 26(151):1–25, July 1913.

[12] A. L. Bowley. The Standard Deviation of the Correlation Coefficient. *Journal of the American Statistical Association*, 23(161):31–34, 1928.

[13] John Byrd. Storage Ring Dynamics: Longitudinal Motion, June 2014.

[14] J. S. Fraser. Beam Analysis Tomography. *IEEE Transactions on Nuclear Science*, 26(1):1641–1645, February 1979.

[15] J. Smeets G. Janssens. PD-0402: Proton range monitoring using prompt gamma camera in clinical configuration. *Radiotherapy and Oncology*, 111:S158–S159, 2014.

[16] Evgeny Galyaev. Ionizing particle beam fluence and position detector array using micromegas technology with multi-coordinate readout, November 2017.

[17] I. Giomataris, R. De Oliveira, S. Andriamonje, S. Aune, G. Charpak, P. Colas, G. Fanourakis, E. Ferrer, A. Giganon, Ph. Rebourgeard, and P. Salin. Micromegas in a bulk. *Nuclear Instruments and Methods in Physics Research Section A: Accelerators, Spectrometers, Detectors and Associated Equipment*, 560(2):405–408, May 2006.

[18] Susumu Ikeda and John M. Carpenter. Wide-energy-range, high-resolution measurements of neutron pulse shapes of polyethylene moderators. *Nuclear Instruments and Methods in Physics Research Section A: Accelerators, Spectrometers, Detectors and Associated Equipment*, 239(3):536–544, September 1985.

[19] Kim Baraka, Asmund Folkestad, Kevin Heijhoff, Dorothea Pfeiffer, Joshua Renner, Heinrich Schindler, Ali Sheharyar, Nicholi Shiell, Rob Veenhof, and Klaus Zenker. Garfield++ – simulation of ionisation based tracking detectors.

[20] Glenn F. Knoll. *Radiation Detection and Measurement*. John Wiley & Sons, August 2010. Google-Books-ID: 4vTJ7UDel5IC.

[21] Antje-Christin Knopf and Antony Lomax. In vivo proton range verification: a review. *Phys. Med. Biol.*, 58(15):R131, August 2013.

[22] Benzion Kozlovsky, Ronald J. Murphy, and Reuven Ramaty. Nuclear Deexcitation Gamma-Ray Lines from Accelerated Particle Interactions. *ApJS*, 141(2):523, 2002.

[23] J. Krimmer, M. Chevallier, J. Constanzo, D. Dauvergne, M. De Rydt, G. Dedes, N. Freud, P. Henriquet, C. La Tessa, J.M. Létang, R. Pleskač, M. Pinto, C. Ray, V. Reithinger, M.H. Richard, I. Rinaldi, F. Roellinghoff, C. Schuy, E. Testa, and M. Testa. Collimated prompt gamma TOF measurements with multi-slit multi-detector configurations. *Journal of Instrumentation*, 10(01):P01011–P01011, January 2015.

[24] F. Kuger. Micromesh-selection for the ATLAS New Small Wheel Micromegas detectors. *J. Inst.*, 11(11):C11043, 2016.

[25] Dr William R. Leo. Scintillation Detector Mounting and Operation. In *Techniques for Nuclear and Particle Physics Experiments*, pages 199–213. Springer Berlin Heidelberg, 1994.

[26] D. A. Low, W. B. Harms, S. Mutic, and J. A. Purdy. A technique for the quantitative evaluation of dose distributions. *Med Phys*, 25(5):656–661, May 1998.

[27] Chul Hee Min, Han Rim Lee, Chan Hyeong Kim, and Se Byeong Lee. Development of array-type prompt gamma measurement system for in vivo range verification in proton therapy. *Med Phys*, 39(4):2100–2107, April 2012.

[28] Danairis Hernandez Morales, Jie Shan, Wei Liu, Kurt E. Augustine, Martin Bues, Michael J. Davis, Mirek Fatyga, Jedediah E. Johnson, Daniel W. Mundy, Jiajian Shen, James E. Younkin, and Joshua B. Stoker. Automation of routine elements for spot-scanning proton patient-specific quality assurance. *Medical Physics*, 46(1):5–14, 2019.

[29] R. C. Murty. Effective Atomic Numbers of Heterogeneous Materials. *Nature*, 207(4995):398–399, July 1965.

[30] N. Otuka, E. Dupont, V. Semkova, B. Pritychenko, A. I. Blokhin, M. Aikawa, S. Babykina, M. Bossant, G. Chen, S. Dunaeva, R. A. Forrest, T. Fukahori, N. Furutachi, S. Ganesan, Z. Ge, O. O. Gritzay, M. Herman, S. Hlavač, K. Katō, B. Lalremruata, Y. O. Lee, A. Makinaga, K. Matsumoto, M. Mikhaylyukova, G. Pikulina, V. G. Pronyaev, A. Saxena, O. Schwerer, S. P. Simakov, N. Soppera, R. Suzuki, S. Takács, X. Tao, S. Taova, F. Tárkányi, V. V. Varlamov, J. Wang, S. C. Yang, V. Zerkin, and Y. Zhuang. Towards a More Complete and Accurate Experimental Nuclear Reaction Data Library (EXFOR): International Collaboration Between Nuclear Reaction Data Centres (NRDC). *Nuclear Data Sheets*, 120:272–276, June 2014.

[31] Harald Paganetti. Range uncertainties in proton therapy and the role of Monte Carlo simulations. *Phys Med Biol*, 57(11):R99–R117, June 2012.

[32] Harald Paganetti. *Proton Therapy Physics*. CRC Press, April 2016.

[33] R. Kamermans Paul Schotanus. Scintillation characteristics of pure and Tl-doped CsI crystals. *Nuclear Science, IEEE Transactions on*, 37(2):177 – 182, 1990.

[34] Jv Siebers, Sm Vatnitsky, Dw Miller, and Mf Moyers. Deduction of the Air W-Value in a Therapeutic Proton-Beam. *Phys. Med. Biol.*, 40(8):1339–1356, August 1995. WOS:A1995RN27600004.

[35] Alfred Smith, Michael Gillin, Martin Bues, X. Ronald Zhu, Kazumichi Suzuki, Radhe Mohan, Shiao Woo, Andrew Lee, Ritsko Komaki, James Cox, Kazuo Hiramoto, Hiroshi Akiyama, Takayuki Ishida, Toshie Sasaki, and Koji Matsuda. The M. D. Anderson proton therapy system. *Med Phys*, 36(9):4068–4083, September 2009.

[36] C. Tran Duy, N. Bonifaci, A. Denat, O. Lesaint, L. Caliap, A. Girodet, B. Gelloz, and P. Ponchon. Partial discharges at a triple junction metal/solid insulator/gas and simulation of inception voltage. *Journal of Electrostatics*, 66(5):319–327, May 2008.

[37] Joost M. Verburg, Kent Riley, Thomas Bortfeld, and Joao Seco. Energy- and time-resolved detection of prompt gamma-rays for proton range verification. *Phys. Med. Biol.*, 58(20):L37, October 2013.

[38] Joost Mathias Verburg. Reducing range uncertainty in proton therapy. 2015.

[39] Y. Giomataris, Ph. Rebourgeard, J.P. Robert, and G. Charpak. MICROMEGAS: a high-granularity position-sensitive gaseous detector for high particle-flux environments. *Nuclear Instruments and Methods in Physics Research Section A:*

Accelerators, Spectrometers, Detectors and Associated Equipment, 376(1):29–35, June 1996.

[40] James F. Ziegler and Jochen P. Biersack. The Stopping and Range of Ions in Matter. In D. Allan Bromley, editor, *Treatise on Heavy-Ion Science*, pages 93–129. Springer US, 1985.